First Steps of the ECHo Experiment: Penning-Trap Mass Measurements of the ^{163}Ho Electron Capture Process and Implantation of ultrapure Ho into Microcalorimeter Arrays

Dissertation

zur Erlangung des Grades

„Doktor der Naturwissenschaften“

am Fachbereich Physik, Mathematik und Informatik

der Johannes Gutenberg-Universität in Mainz

Fabian Schneider
geb. in Darmstadt

Mainz, den 24.05.2016

Abstract

The mass of the electron neutrino $m(\nu_e)$ is known to be non-zero but has not been directly measured yet. The ECHo experiment (Electron Capture of ^{163}Ho) has been initiated as an approach to do so by analysis of the electron capture decay spectrum of ^{163}Ho using metallic magnetic calorimeters. The radioisotope ^{163}Ho has been produced from enriched ^{162}Er in a high flux nuclear reactor and was isolated from the target by high performance liquid chromatography. Dominant remaining contaminants are stable ^{165}Ho and the long lived isomer ^{166m}Ho. Within this work, two important preparatory tasks for the ECHo experiment have been carried out: Mass measurements of ^{163}Ho and ^{163}Dy were performed as prerequisite for a high precision determination of the decay energy Q_{EC}. And the embedding of ultra-pure ^{163}Ho into microcalorimeters by ion implantation in a mass separator has been developed and characterized, including the performance of the applied highly efficient and selective process of resonant laser ionization.

The atomic mass measurements were carried out at the Penning-trap mass spectrometer setup TRIGA-TRAP. By employing the time-of-flight ion cyclotron resonance technique the uncertainties of the masses of ^{163}Ho and ^{163}Dy could be decreased in comparison to former literature data. In the run-up to these measurements, the ion production from the newly procured ^{163}Ho, as well as from stable holmium and dysprosium samples, using a laser ablation ion source in combination with radiofrequency trapping was studied to confirm the required purity of the ^{163}Ho sample for high-precision Penning-trap mass spectrometry.

For the implantation of ^{163}Ho into calorimeters, the complete process from sample preparation to ion implantation using the mass separator RISIKO was investigated and a reliable and quantifiable preparation of ^{165}Ho could be demonstrated. For the resonant laser ionization of holmium a fully resonant three-step optical excitation scheme was applied. Mechanical modifications of the ion source components on the basis of heat flow simulations, contributed strongly to the ionization efficiency and reliability of the process by improving the temperature distribution of the ion source. To estimate the expected suppression of ^{166m}Ho during implantation of ^{163}Ho, the transmission peak shape behind the separation slit was analyzed. Finally, new post focusing ion optics were installed near the detector region to maximize the fraction of the ion beam implanted into the calorimeter absorbers.

Contents

1 Introduction **1**

2 ECHo: Electron capture of ^{163}Ho experiment **5**

I Precision Mass Measurements of the ^{163}Ho Electron Capture **11**

3 TRIGA-TRAP Experimental Apparatus **15**
3.1 Mini-RFQ ion source 17
3.2 Low energy transport beamline 20
3.3 TRIGA-TRAP Penning traps 21
3.4 Samples 21

4 Mass and Q_{EC} Measurements of ^{163}Ho and ^{163}Dy **23**
4.1 Optimization of the Mini-RFQ ion source 23
4.2 Measurement procedure 24
4.3 Data evaluation 28
4.4 Results 31
4.4.1 Calibration with carbon cluster ions 31
4.4.2 Atomic masses of ^{163}Ho and ^{163}Dy 32
4.4.3 Electron capture Q-value of ^{163}Ho 33
4.5 Conclusion 34

II Implantation of ultrapure Ho in Microcalorimeter Arrays **37**

5 RISIKO Experimental Apparatus **41**
5.1 Resonant laser ionization ion source 42
5.2 Ion optics and separator magnet 42
5.3 Ion detection 43
5.4 High-repetition Ti:sapphire laser system 44

6 Initial evaluation of the ^{163}Ho ionization and separation process **45**
6.1 Sample preparation 45
6.2 Ionization efficiency 48
6.3 Mass separation 54

6.4 Ion implantation 57
6.5 Summary 61

7 Improvements to the implantation process 63
7.1 Ion source temperature optimization 63
7.2 Reduction of beam contamination 68
7.3 Beam refocusing 74
7.4 Summary 79

III Conclusion 81

IV Appendix 87

A Simulation studies of the Mini-RFQ ion source 89
A.1 SIMION Representation of the Mini-RFQ ion source 90
A.1.1 Ion initial conditions 90
A.1.2 Simulation procedure 91
A.2 Simulation results 93

B Mass Measurement Fit Parameters 99

List of Figures 101

List of Tables 102

Bibliography 105

Chapter 1

Introduction

Neutrinos contain one of the last mysteries in the standard model of particle physics. Although we are continuously bathed in a stream of neutrinos, already their detection is difficult and measuring their properties poses an enormous challenge - so far impeding a measurement of their mass. W. Pauli first postulated the existence of neutrinos - originally as "*neutrons*" - in 1930 as an explanation for the observed continuous spectra in β decays. This proposal was in stark contrast to atomic theories of the time, so other physicists hesitated to follow its ideas. Nevertheless, E. Fermi agreed with Pauli and polished the idea in 1934 to the point where he could reproduce the shape of observed β spectra [1]. He saw strong evidence for a particle that was electrically neutral and had a very tiny mass or even none at all. On this more solid foundation, experimentalists started to search for direct evidence of neutrinos. But it took nearly two decades until these elusive particles could be observed by C. Cowan and F. Reines in 1956 [2]. Their observation of the "*inverse β decay*" initiated by reactor produced neutrinos was not only ground breaking, but also awarded with the Nobel prize in 1995[1]. Several more important postulations and discoveries in the following years lead to the establishment of three neutrino flavors in the nuclear standard model: the electron neutrino ν_e, the muon neutrino ν_μ and the tau neutrino ν_τ. All three particles share the properties of being charge zero leptons with spin $1/2$ and having zero mass. This apparently complete picture of the neutrinos was disturbed already in the late 1960s when the Homestake experiment lead by R. Davis detected significantly smaller amounts of electron neutrinos as was expected by the standard solar model [3]. A piece to solve the puzzle was given in 1958 by B. Pontecorvo [4, 5]: If neutrinos were massive, an oscillation between different neutrino types would be possible, leading to a smaller number of neutrinos at the experiment site to which it was sensitive. At the time only the electron neutrino was known, so he assumed the transition $\nu_e \rightleftarrows \bar{\nu}_e$. After the discovery of the muon neutrino ν_μ by L. Lederman, M. Schwartz and J. Steinberger in 1962 [6], this theory was expanded to also include the flavor oscillation $\nu_e \rightleftarrows \nu_\mu$ [7]. Based on this, only half of the neutrinos emitted in the sun's core would be detected as ν_e when they reach earth, whereas the other

[1] The nobel prize was only awarded to Reines, as Cowan had died in 1974.

half would have changed to another flavor - to which Davis' Homestake experiment was insensitive. Two decades later, in the 1990s, a new generation of neutrino detectors was commissioned to detect neutrinos by the Cherenkov light emitted when scattered in large heavy water volumes: the Sudbury Neutrino Observatory [8] and the Super-Kamioka Neutrino Detection Experiment [9]. These could detect both ν_e and ν_μ and by careful analysis even distinguish them. Thus, they not only observed the lack of electron neutrinos, but also confirmed the appearance of muon neutrinos emitted from the sun's direction. This unambiguous proof of neutrino oscillation made clear that neutrinos are massive and was awarded with last year's 2015 Nobel prize.

The non-vanishing neutrino mass poses the question on how to measure it. Although neutrino oscillations are the definitive proof of a non-zero mass, they can not be used for its determination. In the corresponding theory, the three flavor states are a rotated projection of three mass eigenstates. Their mass only enters into the oscillation length which is proportional to $E/\Delta m^2_{ij}$, *i.e.*, the neutrino energy divided by the difference of squared masses $\Delta m^2_{ij} = m^2_i - m^2_j$ of two neutrino mass eigenstates. From the current best values of $\Delta m^2_{21} = 7.53(18) \cdot 10^{-5}\,\mathrm{eV}^2$ and $\Delta m^2_{32} = 2.44(6) \cdot 10^{-3}\,\mathrm{eV}^2$ [10] the total mass of the three eigenstates can be deduced to be at least $\sum m(\nu_i) > 0.058\,\mathrm{eV}$, while neither absolute values nor upper limits can be extracted from neutrino oscillations for individual neutrino flavors as stated above.

Nevertheless, there are several approaches to determine the neutrino mass, from which so far, none has conclusively been able to determine a value. However, in most cases the lack of a direct signature still allows to set upper limits to either the sum of neutrino masses or the neutrino flavor relevant to the specific process. For example, by fitting a model for the early universe to the data from the Wilkinson Microwave Anisotropy Probe, the authors of [11] were able to determine an upper limit $\sum m(\nu_i) < 1.1\,\mathrm{eV}$. By including data from other cosmological surveys and opening more degrees of freedom in the model, they were even able to report a limit as low as $\sum m(\nu_i) < 0.33\,\mathrm{eV}$. However, the robustness of these values is connected to the specific model, which known to be incomplete beyond linear contributions of $m(\nu_i)$. A more direct access to the neutrino mass is the search for neutrinoless double beta decay ($0\nu\beta\beta$). In contrast to classical double beta decay ($2\nu\beta\beta$) where two neutrinos are emitted, in $0\nu\beta\beta$ a virtual neutrino is emitted and absorbed at the same time. This is only possible if neutrinos are Majorana particles, *i.e.*, fermions that are their own antiparticles [12]. Besides important implications for particle physics in general, *e.g.*, lepton number non-conservation, the observation of this specific decay channel allows a neutrino mass determination. The decay rate would be proportional to the squared mass of the electron neutrino, and being based on only two parameters from nuclear physics, much less model dependent.

An essentially model independent approach is the high precision study of low en-

ergy β decay kinematics. From the difference of the β energy spectrum endpoint E_{max} and the decay energy Q_{β}, the mass of the electron antineutrino can be deduced as $m(\bar{\nu}_{\mathrm{e}}) = Q_{\beta} - E_{\mathrm{max}}$. The most successful experiments so far were performed at Troitsk and Mainz, both studying the emitted electron spectrum of the tritium β decay in so called MAC-E energy filters [13, 14]. They derived upper limits of $m(\bar{\nu}_{\mathrm{e}}) < 2.05\,\mathrm{eV}$ and $m(\bar{\nu}_{\mathrm{e}}) < 2.2\,\mathrm{eV}$, respectively. Currently the next generation MAC-E filter experiment KATRIN is being set up at Karlsruhe [15]. With a 40 m main spectrometer vessel it aims to reach a sensitivity for $m(\bar{\nu}_{\mathrm{e}})$ of 0.2 eV.

In recent years, the advances in low temperature calorimetry made another detection scheme possible. By embedding the radioactive source in a calorimeter, a complete decay spectrum can be recorded at once. For example the MARE collaboration plans to investigate the decay spectrum of ^{187}Re, which decays to ^{187}Os with a half-life of $5 \cdot 10^{10}$ a and a decay energy of $Q_{\beta} = 2.47\,\mathrm{keV}$ [16]. The seven times lower decay energy compared to tritium ($Q_{\beta} = 18.6\,\mathrm{keV}$) significantly increases the important relative event rate close to the spectrum endpoint. Furthermore, this technique can be applied to electron capture (EC) decays as well. Here, the decay energy is split up between the emitted neutrino and the daughter atom as excitation energy. In the following de-excitation process the latter is released through X-ray photons and Auger electrons and is recorded by the calorimeter. The ideal isotope, ^{163}Ho, has already been identified in 1982 by A. de Rújula [17]. It features a similarly low decay energy as ^{187}Re but with a much more reasonable half-life of 4570 a. For the same activity, 10^7 times less sample material is needed, making smaller calorimeters with higher energy resolution possible. The only drawback is the requirement of producing ^{163}Ho at an accelerator or reactor facility as it is not naturally occurring. Three collaborations have started to follow this approach towards a direct measurement of the neutrino mass: HOLMES [18] based in Italy, NuMECS [19] based in the US, and ECHo [20] based in Germany. What is common for all of these direct measurement experiments is the strive to reduce detector background as much as possible. This includes purification of the radioactive sources to highest extent. Furthermore, to increase the quality of the result independently measured high-precision Q values are highly desirable. Although Q_{β} and Q_{EC} can be determined by fitting theoretical curves to the recorded spectra, externally measured values can serve as consistency check and possibly reveal overlooked sources of systematic errors as well as increase the precision of the fit.

The scope of this thesis includes two crucial preparatory tasks for the ECHo experiment. With the newly produced ^{163}Ho sample, the atomic masses of ^{163}Ho and ^{163}Dy were measured by Penning-trap mass spectrometry at TRIGA-TRAP as presented in part I. These studies served to analyze the suitability of the sample and the ionization method for future Penning-trap based measurements, namely the high-precision measurement of Q_{EC} at SHIPTRAP. Part II concerns the development, evaluation and

improvement of ^{163}Ho source purification and embedding. Starting from the same sample as for the Penning-trap mass measurements, ^{163}Ho had to be ionized, mass separated to remove any contaminants and implanted into the calorimeter absorbers with high efficiency and ultimate purity in respect to radioactive contaminations. A general overview of the ECHo experiment, including the detection technique and the ^{163}Ho production, is presented in the following chapter.

Chapter 2

ECHo: Electron capture of ^{163}Ho experiment

^{163}Ho has been studied in view of the neutrino mass by several groups [22–25]. So far, all efforts were hampered by low energy resolution of the respective detection techniques and limited statistics due to small amounts of ^{163}Ho. Therefore only strong resonances in the de-excitation spectrum were analyzed rather than the complete spectrum or specifically the shape near the endpoint. Dominant resonances appear at distinct energies associated with the binding energy of M and N shell electrons as shown in fig. 2.1. Captures from the inner shells, K and L, are not possible because their binding energy is larger than the available decay energy Q_{EC}. Limits to the electron neutrino mass obtained by these groups are comparably imprecise, with the most

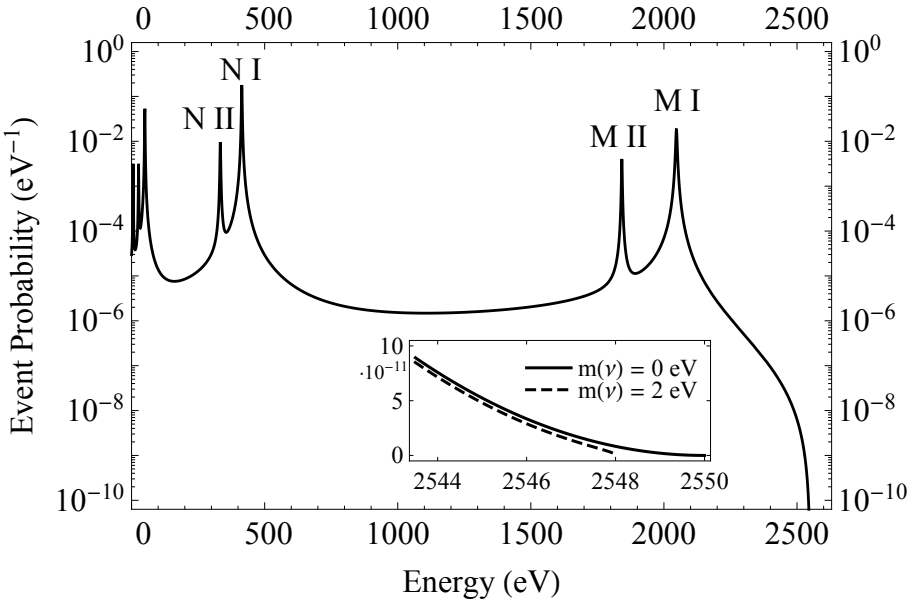

Figure 2.1: Calculated de-excitation spectrum of the ^{163}Ho $\rightarrow$ ^{163}Dy + ν_{e} electron capture decay. The endpoint is assumed to be 2.55 keV. In the inset the effect of a neutrino mass of 2 eV is shown by the dashed line. The resonances correspond to capture of electrons from the atomic shells as labeled. Figure adopted from [21].

stringent one being $m(\nu_e) < 225\,\text{eV}$ from Springer *et al.* [24]. To reach a sub-eV sensitivity to $m(\nu_e)$, a detection method with an energy resolution of a few eV combined with statistics of 10^{14} to 10^{16} detected events would be necessary [26].

The ECHo collaboration envisages to employ an array of metallic magnetic calorimeters (MMC) loaded with a total ^{163}Ho activity of 1 MBq to reach this goal [20, 27]. Using MMCs as bolometer for soft X-rays, energy resolutions down to 2 eV were already demonstrated [29]. This value was achieved by reducing the calorimeter size to dimensions of few 100 µm edge lengths and a miniumum thickness necessary for complete absorption of the particles to be measured, *i.e.*, about 5 µm for < 10 keV photons. The resulting low heat capacity combined with an operation at 30 mK leads to a strong relative change in temperature for each detected particle. A paramagnetic sensor further translates the corresponding temperature increase into a non-linear change of magnetization which is read out by a SQUID. Figure 2.2 shows the layered structure of the MMCs to be used in the development phase of ECHo for which ^{163}Ho will be embedded between two 5 µm gold absorber layers. A performance evaluation of these calorimeters resulted in an energy resolution of 12 eV and a signal risetime of 90 ns [27]. To be able to readout a large number of MMCs in parallel, a multiplexing scheme is used [30]. This in turn increases the effective signal risetime due to limited bandwidth to about 500 ns. Still, the detector performance is already quite close to expectations and the maximum ^{163}Ho activity per MMC can be estimated based on these values. The limitation arises from possible pile-up events, *i.e.*, from two decays occurring in a time frame of the signal rise time. In this case, the measured energy is the sum of the two events. For measuring the neutrino mass, this is critical because false-positive events with energies above Q_{EC} are generated. The ideal amount of ^{163}Ho per MMC is therefore as large as possible, but small enough to prevent excessive pile-up events. Monte-Carlo simulations indicate that above a pile-up fraction of 10^{-5} these

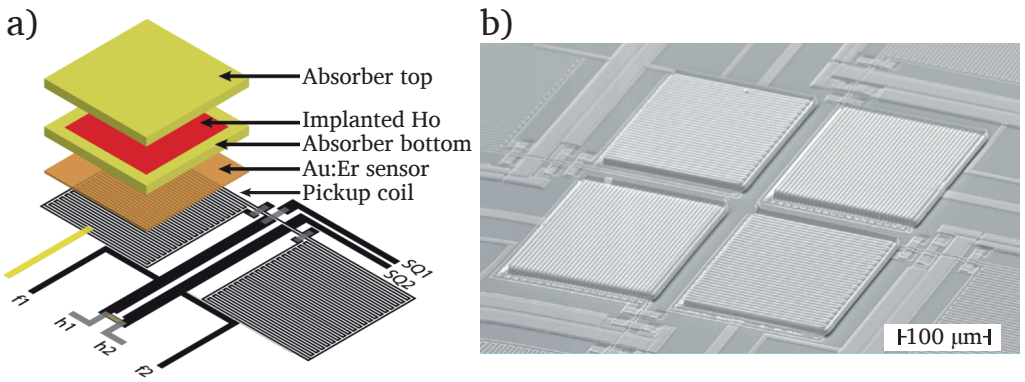

Figure 2.2: (a) Schematic view of a metallic magnetic calorimeter as employed in the ECHo experiment. (b) Raster electron microscope image of a 2×2 MMC array. Figures adopted from [27, 28].

cause the dominant background. This fraction is expected at an activity of 1 Bq per MMC. Therefore, the estimated target of 10^{14} detected events in three years of data taking will require about 10^6 calorimeters in parallel. Because this number may be reduced by orders of magnitude if the MMC performance is improved, an intermediate phase of the ECHo experiment is in preparation with a smaller number of MMCs applying the current state of the art read out and data handling. Instead of 10^6 MMCs loaded with 1 MBq of ^{163}Ho, only 1000 calorimeters with a total activity of 1 kBq are to be deployed for this stage.

One of the key tasks in the ECHo experiment is the loading of the calorimeters with ^{163}Ho - ideally *only* with ^{163}Ho. Any other radioactive co-implant will increase the background count rate. Because the relevant part of the electron capture spectrum close to the endpoint is already suppressed by more than eight orders of magnitude compared to the count rate of the resonances, any increase in the background signal can quickly overshadow the relevant data in this region. Therefore the ^{163}Ho source introduction has to include several purification steps to eliminate any radioactivity that is inevitably co-produced. Also contaminations with stable atoms in significant amounts can hamper the detector performance through the corresponding increase in heat capacity.

A first test of the ^{163}Ho production using the high energy proton beam at ISOLDE/CERN proved quite successful. From the produced amount, 0.01 Bq ($\approx 10^9$ atoms ^{163}Ho) were directly implanted as ion beam into the MMC detector pixels. This facilitated recording the electron capture spectrum and a redetermination of the ^{163}Ho Q_{EC}-value [27]. However, co-produced ^{144}Pm was ionized in molecular form of $^{144}Pm^{19}F^{+}$ and, due to the same mass to charge ratio, could not be separated from ^{163}Ho and was implanted as well. The additional peaks in the spectrum prohibited any evaluation beyond the strengths of the M and N capture resonances. This emphasizes the necessity of splitting the production and the sample introduction processes. With additional purification steps envisaged, the production of ^{163}Ho could be carried out in a nuclear reactor, where much larger production yields are available at the cost of more co-produced radioactivity in comparison to accelerator based production [31]. After chemical isolation of holmium, the process is kept the same: ^{163}Ho will be ionized, mass separated and implanted as ion beam into the calorimeters. Because a direct production of radionuclides is not needed anymore, this has not be performed at ISOLDE, but can be carried out at other high efficiency mass separators as well.

The first large scale ^{163}Ho production for ECHo was carried out at the high flux nuclear reactor at the Institut-Laue-Langevin in Grenoble, France [32]. 30 mg of erbium, enriched to 20 % in ^{162}Er was irradiated for 55 days with a neutron flux of $1.3 \cdot 10^{15}\,\mathrm{cm^{-2}\,s^{-1}}$ [32]. In this way, about 10 % of the ^{162}Er was activated to ^{163}Er which then decayed to ^{163}Ho providing a yield of 10 MBq ($\approx 10^{18}$ atoms) of ^{163}Ho.

A chromatographic ion exchange resin for the extraction of lanthanide elements was developed at the Paul-Scherrer-Institute in Villigen, Switzerland, for the use in radiopharmaceutical applications. This resin was further optimized to isolate holmium from mixed lanthanide samples. In this way, holmium can be extracted from the erbium target after neutron irradiation. To prevent production of lighter contaminations, the erbium target material was also purified in a similar process prior to the irradiation. The quantitative removal of lighter elements than erbium significantly suppresses the production of radioactive isotopes of dysprosium and below. Combined with the chromatographic separation afterwards, a fraction can be obtained containing $> 95\,\%$ of the produced holmium, including ^{163}Ho, ^{a}Hond ^{166m}Ho, with no further radioactive isotopes. A detailed description of the chemical purification steps will be given in [33].

The sample constitution (relative to the atom content of ^{163}Ho), as determined by a combination of γ-spectroscopic and ICP-MS measurements, is given in table 2.1. Here, the content of ^{166m}Ho is of primary concern. From simulations of the expected electron capture spectra and statistical estimations, an upper limit for the concentration was deduced. At a relative concentration above 10^{-9}, the additional background negatively influences the obtainable precision for the neutrino mass. The mass spectrometric separation has therefore to suppress ^{166m}Ho by a factor of 10^5 in comparison to ^{163}Ho. In contrast, for the Penning trap mass measurements the concentration of ^{163}Dy is critical. It was estimated that at a relative level above $0.2\,\%$ the observed cyclotron frequencies could be shifted more than the measurement resolution of SHIPTRAP [34]. Its concentration could not be determined so far. Excluding external contaminations, the only source for ^{163}Dy is the decay of ^{163}Ho which is negligible in the period of one year between irradiation and measurement. By comparison, the concentration of ^{164}Dy, which is produced during the irradiation by neutron capture of ^{163}Ho and subsequent electron capture of ^{164}Ho ($T_{1/2} = 29\,\text{min}$), was determined to be $0.4\,\%$ by neutron activation analysis.

Table 2.1: Content of the ^{163}Ho sample after chromatographic purification. Concentrations are given relative to the ^{163}Ho content. The erbium isotopes are residuals of the production target.

Isotope	Rel. Concentration
^{163}Ho	1
^{165}Ho	0.500
^{166m}Ho	$2 \cdot 10^{-4}$
^{162}Er	0.017
^{164}Er	0.004
^{166}Er	0.031
^{168}Er	0.039
^{170}Er	0.008
^{164}Dy	0.004
^{23}Na	0.560

Part I

Precision Mass Measurements of the ^{163}Ho Electron Capture

The goal of measuring the atomic masses of ^{163}Ho and ^{163}Dy was threefold: First, the laser ablation ion source (the Mini-RFQ ion source, see sec. 3.1) had to be tested if it reliably delivered holmium and dysprosium ions from adequately small samples. Second, the newly procured and chemically purified ^{163}Ho sample was assumed to contain traces of stable ^{163}Dy. Because the amount could not be quantified, the feasibility of using it for Penning-trap mass spectrometry had to be confirmed. Third, measuring the physical quantities themselves. The Atomic Mass Evaluation 2012 lists the atomic masses of the two isotopes with uncertainties of 1.8 keV [35]. The recently attained relative uncertainties of $5 \cdot 10^{-9}$ in the masses of transuranium isotopes [36] applying the time-of-flight ion-cyclotron-resonance (ToF-ICR) technique proved that at TRIGA-TRAP a mass measurement of ^{163}Ho with 1 keV uncertainty should well be possible. In addition, all three of these aspects serve as preparatory work for the precise determination of the ^{163}Ho electron capture Q-value. Here, the recommended value of 2.555(16) keV [35], is reported with a very small uncertainty, although there are discrepancies beyond 0.1 keV between the results of different groups as shown in fig. 2.3. To verify this value, a renewed measurement of Q_{EC} with a different technique would be necessary with a similar uncertainty. This is beyond the limits of the ToF-ICR technique as applied at TRIGA-TRAP. But, the newly developed phase-imaging ion-cyclotron-resonance technique (PI-ICR [37]) was found appropriate to perform a direct Q_{EC} determination using SHIPTRAP which complements the calorimetrically measured values. These Q_{EC} measurements require additional input from atomic physics which increases the chances of systematic deviations. Here, a measurement based on Penning-trap mass spectrometry has the advantage of being independent from theory, as only the mass difference between the two nuclides is directly measured. Because the ion preparation and ionization technique as well as the mass separation in the preparation Penning trap are performed at SHIPTRAP in an identical fashion to TRIGA-TRAP, the first two of the scientific goals are directly applicable to such a measurement.

The sample preparation, measurement method and results of these mass measurements have been published in [21] out of which parts are reproduced in this work with kind permission of The European Physical Journal (EPJ). The results of the Q_{EC} determination at SHIPTRAP are published by Eliseev *et al.* in [38].

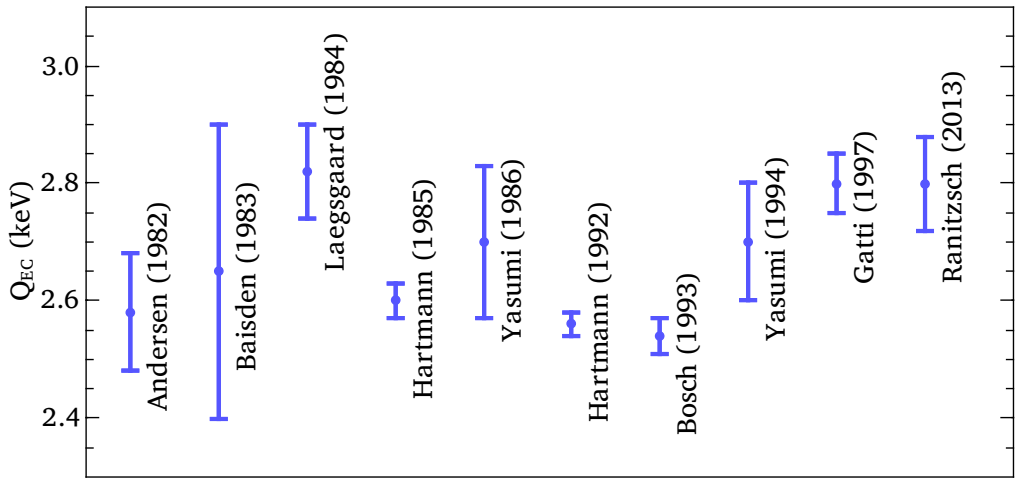

Figure 2.3: Overview of the results from measurements of the ^{163}Ho electron capture Q-value [22, 23, 25, 27, 39–44] as listed in the Atomic Mass Evaluation 2012 [35]. The recommended value of 2.555(16) keV is calculated exclusively from the two values of Hartmann *et al.* [25, 41] and Bosch *et al.* [42], disregarding the values around 2.8 keV.

Chapter 3

TRIGA-TRAP Experimental Apparatus

The TRIGA-TRAP experiment is a setup for Penning-trap mass spectrometry. It is designed for direct mass measurements of singly charged ions in the mass range of 20 to 300 u. It is situated in the experimental area next to the research reactor TRIGA Mainz as a part of the TRIGA-SPEC collaboration, whose goal is to study ground state properties of exotic nuclei [45]. A photograph of the complete TRIGA-SPEC setup is shown in fig. 3.1. By exploiting the neutron flux through fissionable targets of ^{235}U or ^{249}Cf a large number of fission fragment isotopes are produced for the experiments. These fragments are thermalized in the stopping chamber by buffer gas and subsequently transported by aerosol particles embedded in the gas flow to a surface ionization ion source [46]. It employs a tantalum tube heated by electron bombardment to temperatures of 2000 °C. The created ions are accelerated to an energy of 28 keV and, after mass separation, cooling and optionally bunching in a gas filled RFQ [47], are sent to either of the experiments. The TRIGA-LASER setup overlaps the ion beam with a continuous-wave laser beam for high-precision collinear laser spectroscopy [48]. Several configurations are possible, by sending the laser beam either collinearly or anti-collinearly. In addition, the ion beam can be neutralized in a charge exchange cell for spectroscopy of atomic species. In the TRIGA-TRAP setup, ion bunches are decelerated by means of a pulsed drift tube before they are sent into the low-energy beamline depicted in fig. 3.5 and finally enter the Penning traps situated in the 7 T magnetic field of a superconducting solenoid. A second, dedicated ion source for TRIGA-TRAP is located in a 90° branch of the low-energy beamline. There, a laser ablation ion source has been installed to deliver short ion bunches on demand and independent of the common TRIGA-SPEC beamline [49]. Following an external trigger a single pulse of a frequency doubled Nd:YAG laser is focused on a rotatable target. By adjusting the pulse energy, the size of the ion bunches can be controlled. Recently this ion source was upgraded by positioning the ablation target inside a gas filled RFQ to thermalize the ions and reduce the bunch length. In view of the miniature size of this RFQ compared to typical RFQ cooler and buncher units used for ion bunching in 30 keV beamlines, the name Mini-RFQ ion source was coined.

The following chapter describes the Mini-RFQ ion source, low energy beamline,

Penning traps and the detection section in closer detail.

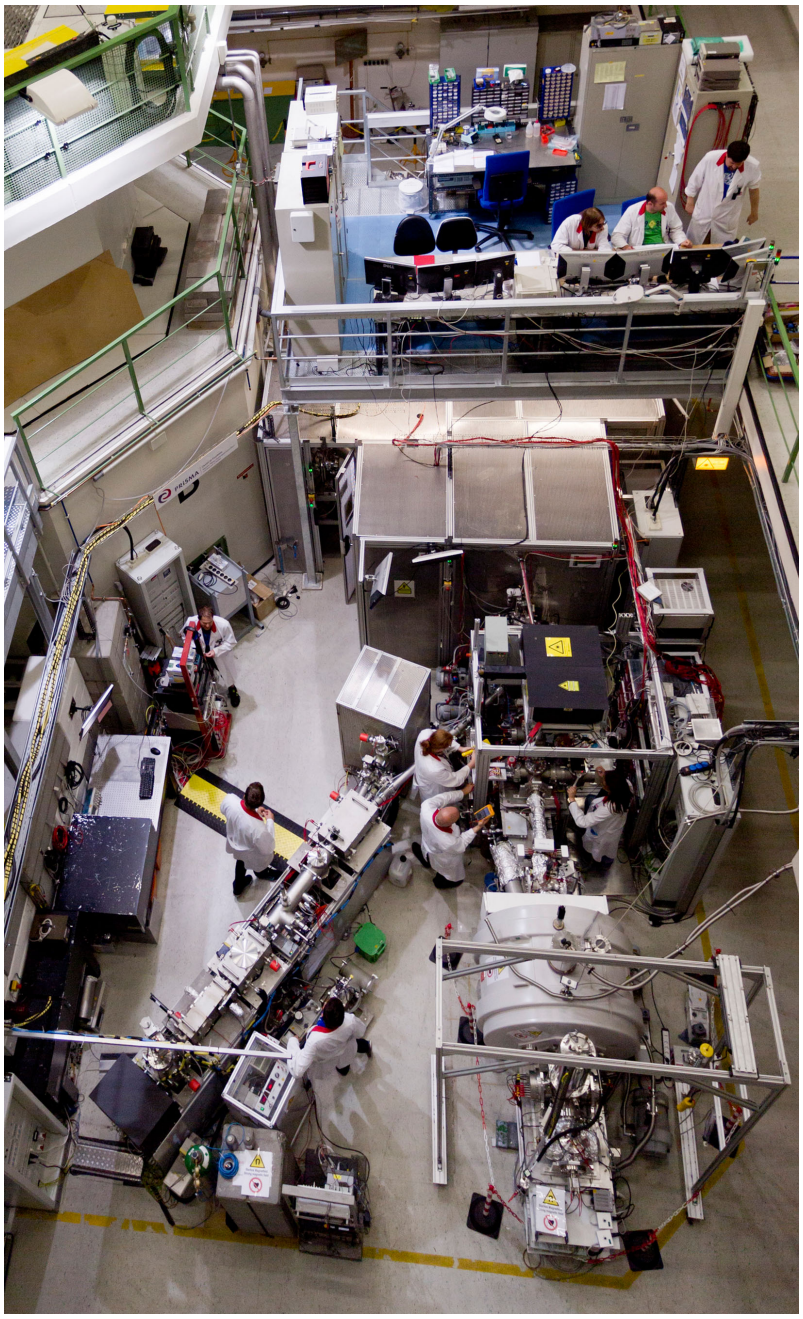

Figure 3.1: Photograph of the TRIGA-SPEC experimental setup. In the top left corner, the research reactor TRIGA Mainz and port B through the concrete shielding of the reactor core is visible. Next to it the operator platform and below it, in the shielded HV cage, the gas-jet transport system and the common beamline are located. The latter connects to the two experiment beamlines TRIGA-LASER (left) and TRIGA-TRAP (right) in the lower part of the picture.

3.1 Mini-RFQ ion source

A previously used laser ablation ion source suffered from a large emittance of the produced ion bunches, mainly caused by the broad kinetic energy distribution associated with the laser ablation process. The resulting low transport efficiency and the long bunches lead to required sample sizes of typically 10^{16} to 10^{17} atoms to perform a mass measurement. Similar to the TRIGA-SPEC common beamline [47] and ISOL-type beamlines in general, where gas-filled RFQs are commonly used for reducing beam emittance and bunching continuous beams into short pulses [50], such an RFQ was to be used with the ablation source as well. Here a further advantage was used: Instead of creating the ions and subsequently injecting them into an RFQ, the ablation process can be driven directly inside the quadrupole volume. With the given ion energies below 10 eV and the pulsed operation, the RFQ can correspondingly be designed in a compact size.

The implementation of that concept is shown in fig. 3.2. The quadrupole field for radial trapping is generated by four cylindrical rods in between two flat electrodes for axial trapping. The back electrode features a circular cutout with its center slightly offset from the center axis. Here the ablation target is inserted from the rear on a rotatable mount, whereby a ring shaped area on the substrate can be targeted by the laser. The back and front electrodes are screwed onto a cylindrical PTFE body to enclose a limited volume which has to be gas filled. Gas is let in through a nozzle and can only escape through the front aperture and the thin gap surrounding the target in the back electrode, thus only a very small gas flow is needed to sustain the desired pressure. Furthermore, to reduce the gas flow into the following beamline, a differential pumping stage is implemented by encapsulating the Mini-RFQ ion source

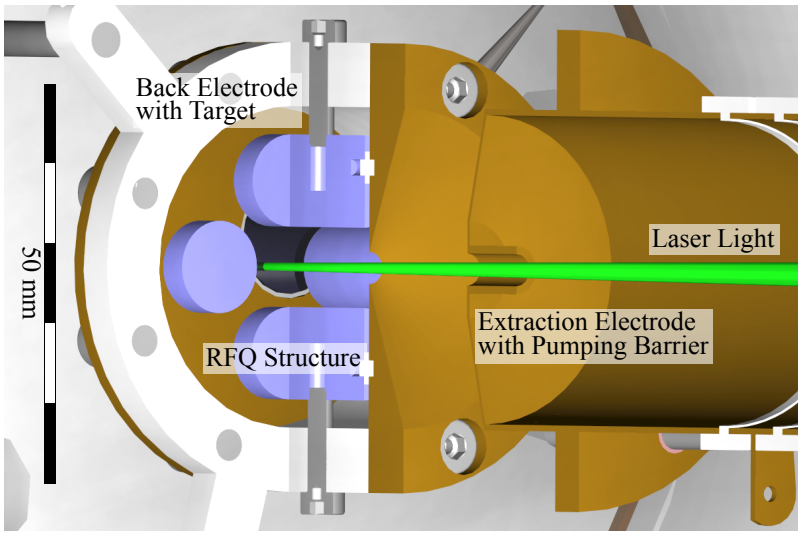

Figure 3.2: 3D model of the Mini-RFQ ion source. Figure adopted from [21].

Table 3.1: Key design parameters of the Mini-RFQ ion source currently in operation.

Parameter	Value
Rod diameter r	10.0 mm
Rod spacing r_0	11.5 mm
Rod length	40.0 mm
Target diameter	14.0 mm
Target thickness	2.0 mm
Offset from center axis	5.0 mm
Front aperture	2.0 mm
Extraction aperture	3.0 mm

into a separate vacuum chamber whose only connection to the beamline is the aperture in the extraction electrode, to which a short tubular extension (see fig. 3.2) is fitted to increase its flow resistance. An overview of the design parameters of the Mini-RFQ ion source is given in tab. 3.1.

The Mini-RFQ ion source is usually fed with liquid samples dissolved in either distilled water or nitric acid, out of which 1 to 10 µl are dried on the substrate. To prevent the drop from wetting a large area, the polished SIGRADUR surface is broken by sandblasting beforehand. For this, a mask with circular cutouts is used to define the sample positions. The 5 mm off-axis mounting defines through rotation under the ablation laser a circle on which four sample spots are prepared in this manner. A photograph of a sample after use, showing traces of the laser pulses, is shown in fig. 3.3. Furthermore, the SIGRADUR substrate itself serves as sample material for

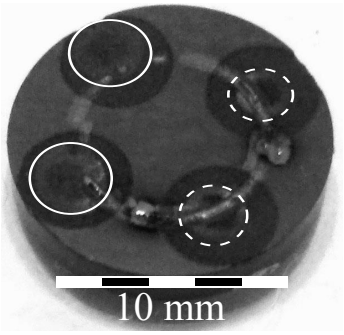

Figure 3.3: Photograph of the ablation target used for the mass measurements of ^{163}Ho and ^{163}Dy. The four darker areas are sandblasted spots where droplets of solutions of ^{163}Ho (solid circles) and ^{nat}Dy (dashed circles) were applied and dried. The bright ring is caused by the laser pulses which remove material from the surface. The two craters at three and six o'clock are the positions used for the production of carbon cluster ions. Figure adopted from [21].

ions of carbon clusters C_n. With the mass of carbon being defined as $m_C = 12\,u$ in the International System of Units (SI), they serve as ideal reference ions in the entire range mass of atomic masses [51]. Their easy availability as singly charged clusters for $1 \leq n \leq 25$ by laser ablation [52] ensures a mass difference of $\Delta m \leq 6\,u$ to the reference ion for all possible mass measurements of singly charged ions. Only in measurements at precision levels of 10^{-9} and below, their binding energy has to be considered. Theoretical calculations for the binding energy report values between 5 and 8 eV per carbon atom, depending on the cluster size and shape, e.g., linear, cyclic or fullerene-like [53, 54].

The ablation is driven using a Continuum Minilite II[1], a pulsed, frequency doubled Nd:YAG laser. It emits pulses with up to 25 mJ energy at a wavelength of 532 nm and a pulse length of 3 to 7 ns. The Nd:YAG laser rod is pumped by a flash lamp and the resonator is Q-switched. At TRIGA-TRAP, it is operated with a fixed delay of 160 µs between lamp flash and Q-switch. Figure 3.4 shows an overview of the laser system at the Mini-RFQ ion source. In front of the Nd:YAG laser a rotatable Glan-Taylor calcite polarizer is installed. It is used to externally control the ablation pulse energy by rotating around the beam axis. A stepper motor is used to set the angle of rotation in steps of 0.05°, thus allowing very fine changes in the pulse energy, especially at very low levels due to the $\cos(\theta)^2$ dependence of the transmitted power. The polarizer is embedded in a metal casing to absorb the escape ray. A 11 %-reflectivity mirror

[1] Continuum, part of the Amplitude Laser Group. http://www.continuumlasers.com/

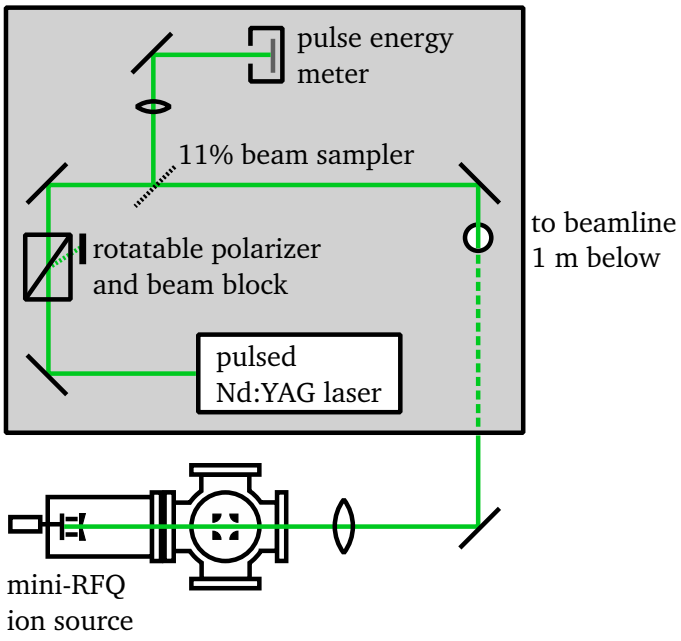

Figure 3.4: Overview of the laser system used for the Mini-RFQ ion source. For more details, see text.

is used to send a reference pulse to a pulse energy meter. The main pulse is sent downwards from the laser table to the vacuum system by two mirrors. A movable lens with a focal length of $f = 450\,\text{mm}$ focuses the beam through a viewport and apertures in the electrodes onto the ablation target. For reasons of laser safety, the complete system, including the beam transport to the vacuum chamber, is enclosed. After manual alignment at very low energy levels, the two most critical parameters, the rotation angle of the polarizer and the position of the focusing lens, can be remote controlled.

3.2 Low energy transport beamline

The beamline for ion bunches from either the Mini-RFQ ion source or decelerated ions from the on-line ion source serves to merge these two beamlines, transport the bunches to the Penning traps and furthermore to separate the ions by mass. For the first task, an electrostatic quadrupole deflector is used. Consisting of four rods, its potential can be set to guide ions in either a 90° bend or straight-through. The subsequent transport section is a nearly continuous set of drift tubes with adjustable potentials to guide and focus the ion bunches into the center of the first Penning trap. With an average ion energy of 1 keV, the differences in flight time through the transport section for different ion species are much larger than the bunch duration of typically 1 to 2 µs. Therefore, pulsable electrodes permit the selective transmission of a small m/q range. A wire mesh electrode 400 mm downstream of the quadrupole deflector provides a pre-selection, whereas the entry-side Penning-trap end cap provides the final mass resolving power of $m/\Delta m \approx 50$. If even after separation, the ion number per bunch is still potentially overloading the first Penning trap and cannot be adequately reduced by adjusting the ablation laser energy, the transmission window can be reduced to less than 1 µs, thus lowering the number of ions entering the trap region.

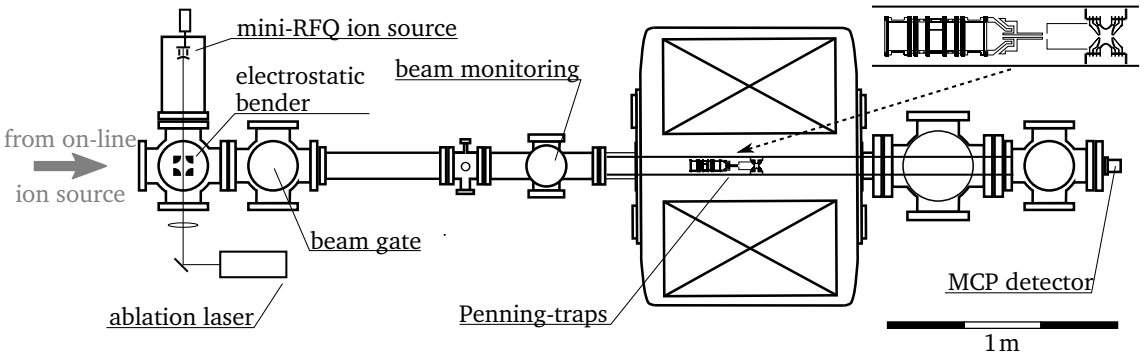

Figure 3.5: Schematic representation of the TRIGA-TRAP setup. The upper right inset shows a detailed view of the two Penning traps. Figure adapted from [21].

3.3 TRIGA-TRAP Penning traps

At TRIGA-TRAP, a setup of two Penning traps located in the same magnet is used for high precision mass measurements with the ToF-ICR technique. The first trap serves as preparation trap, *i.e.*, is used to cool the trapped ions and select one m/q species by resonant buffer gas cooling [55]. Subsequently, in the second trap the actual measurements are performed - or more precisely: the RF excitation pattern is applied. Because of the different applications, the requirements for the two traps differ significantly, which is reflected in their different construction. The preparation trap needs to accept a large ion bunch with high initial energy, therefore a large trapping volume as well as a deep potential is needed. Furthermore, a buffer gas needs to be introduced. In contrast, the measurement trap needs well defined potentials for achieving the highest precision and very low gas pressures to exclude ion-gas collisions. In contrast it only needs to accommodate a small number of ions, as ideally only one ion should be trapped at a time. The inset in fig. 3.5 shows a sectional view of the trap system as it is implemented. The preparation trap consists of seven cylindrical electrodes, with the lengths of the inner ones optimized for a harmonic trap potential. The center ring electrode is split fourfold to enable dipolar as well as quadrupolar RF excitations. A diaphragm extending to a thin tube connects the two traps and sustains the pressure gradient from 10^{-6} mbar in the preparation traps to below 10^{-8} mbar in the measurement trap. The latter has hyperbolical shaped ring and endcap electrodes, with additional correction electrodes in between and on the outsides to compensate for minor field imperfections like the ones caused by the entry and exit orifices. Similar to the preparation trap, the ring electrode of the measurement trap is segmented as well. In preparation for an implementation of ion detection by their image current, the segmentation is asymmetric, with two larger electrodes (140° segments) for image current pickup and two smaller electrodes only used for RF excitation. Attached to the traps is the final drift beamline which extends to the microchannel plate detector about 1.2 m outside of the magnet housing. The magnetic field accordingly drops along this drift line from 7 T at the magnet center to 7 mT at the detector location.

3.4 Samples

For the measurement of the atomic masses of ^{163}Ho and ^{163}Dy, the cyclotron frequencies of the corresponding ions (or molecular ions, e.g. $^{163}Ho^{16}O^{+}$) need to be measured and referenced to ν_c of an ion with known mass. For this, the carbon cluster ion $^{12}C_{15}^{+}$ was chosen. All of these substances have to be present as dedicated samples on a common ablation target in the Mini-RFQ ion source. To select a specific ion, the target is then rotated to the position of the sample of interest. The individual samples were

prepared in the follow manner:

$^{12}C_n$ The carbon cluster ions could be readily produced by laser ablation in the Mini-RFQ ion source of the SIGRADUR bulk material.

^{165}Ho In the preparation and commissioning phase, stable ^{165}Ho was used instead of ^{163}Ho. The sample was prepared from Holmium(III)nitrate-pentahydrate ($Ho(NO_3)_3 \cdot 5\ H_2O$) bought from Alfa Aesar[2] with a certified purity of 99.9 %. This was weighed and transfered to an aqueous solution with a ^{165}Ho concentration of 10^{19} atoms/ml. Out of this, a 10 µl drop was pipetted onto the dedicated locations on the substrate and evaporated to dryness.

^{163}Dy In a similar fashion to Ho, the ^{163}Dy sample was prepared from Alfa Aesar Dysprosium(III)nitrate-pentahydrate with 99.99 % purity transferred to an aqueous solution. In two different sandblasted positions on a new substrate solution drops were pipetted, with each containing 10^{17} atoms of dysprosium. With the naturally abundance ratios, this corresponds to $2.5 \cdot 10^{16}$ atoms ^{163}Dy.

^{163}Ho The radioactive ^{163}Ho was taken from the chemically purified sample described in tab. 2.1. On both of the two remaining positions of the substrate with Dy samples, a 10 µl drop of the solution was pipetted. From the nominal concentration, these contained $3 \cdot 10^{16}$ atoms ^{163}Ho each. The most significant further contents are $1.5 \cdot 10^{16}$ atoms ^{165}Ho and $3 \cdot 10^{14}$ to $1 \cdot 10^{15}$ atoms of the erbium isotopes ^{162}Er, ^{164}Er, ^{166}Er and ^{168}Er. Although dysprosium was removed quantitatively before neutron irradiation, it could have been produced during irradiation by (n,α) reactions or by the electron capture decays of ^{163}Ho and ^{164}Ho. With ICP-MS and RIMS (see sec. 6.3), no measurable dysprosium content could be detected above the detection threshold of a relative concentration of 10^{-4} to ^{163}Ho.

[2] Alfa Aesar, brand of Thermo Fisher Scientific. http://www.alfa.com

Chapter 4

Mass and Q_{EC} Measurements of ^{163}Ho and ^{163}Dy

4.1 Optimization of the Mini-RFQ ion source

The first step in the experimental optimization procedure was the sample ionization in the Mini-RFQ ion source. For this, potentials and time delays were chosen according to the results of corresponding SIMION simulations (see chap. A). Goal of the optimization procedure was a reproducible production of ion bunches containing less than ten ions. In addition, the bunch length measured at the MCP detector in front of the Penning traps should be as short as possible to increase the mass resolving power of the low energy beamline. The resulting parameters are listed in tab. 4.1. Besides smaller deviations, for example an RF frequency of 1.077 MHz because of a slightly detuned tank circuit, the most obvious change was the necessity of stronger trapping and an initial negative offset voltage of the ablation target. A possible explanation is that ions were created with energies above 15 eV, as observed by the authors of [56]. The ions were trapped for 6 ms, with no change in the transmission or bunch length was observed for longer trapping duration, indicating that the ions have reached the dynamic equilibrium. From this, the pressure inside the Mini-RFQ ion source can be estimated to be between 10^{-2} mbar and 10^{-3} mbar, depending on the actual initial energy. The much lower potential on the first electrode is in parts caused by an increased distance compared to the simulation and the fact that the bunch length could be shortened by a stronger acceleration field. With a 10 V DC quadrupole voltage, only a minor mass resolution was realized, mostly to discard lighter ions with $m < 150$ u.

With the settings given and laser pulse energies above 0.1 mJ, holmium ions were detected. Furthermore, in the time of flight distribution shown in fig. 4.1 the oxide species HoO^+ and HoO_2^+ are also visible. The ratios of their production rates are 1:2:1.6 for Ho^+:HoO^+:HoO_2^+. As a consequence, all further measurements were performed with the monoxide ions. In addition to the increased yield, this offers the advantage of a smaller mass difference between reference ion and measured ion. For $^{163}Ho^+$, the best reference ion would be $^{12}C_{14}$ with $\Delta m = 5$ u, whereas for $^{163}HoO^+$,

Table 4.1: Operational parameters for the Mini-RFQ ion source after optimization in comparison to the values from the SIMION simulations. For details regarding the deviations, see the text.

Parameter	Simulated value	Optimized value
Target offset	1 V	-15 V
Axial trap depth	10 V	30 V
RF Frequency	1 MHz	1.077 MHz
RF Amplitude	476 V	400 V
DC Rod Voltage	< 50 V	10 V
Buffer-gas flow	- -	10^{-5} mbar/(l s)
Buffer-gas pressure	10^{-3} mbar	$\approx 10^{-3}$ mbar
Extraction pulse	100 V	105 V
Target pulse delay	10 µs	10 µs
Trapping duration	2 ms	6 ms
First electrode	-200 V	-2400 V

the mass difference to $^{12}C_{15}$ is only $\Delta m = 1$ u. Systematic shifts in the cyclotron frequency ν_c which are dependent on the mass difference between the two ion species can thus be significantly reduced. From the determined mass of HoO^+, the mass of Ho^+ can then simply be extracted by subtracting the mass of ^{16}O. At the expected level of precision of about 1 keV, the uncertainty in the mass of ^{16}O (0.16 eV) and the binding energy (few eV) can be neglected. For dysprosium a very similar behavior in the relative production rates was observed and therefore the measurements were performed on the monoxide species, too. The production of carbon cluster ions in the necessary mass range set in at higher laser pulse energy levels around 0.2 mJ. The mass spectrum shown in fig. 4.1 was recorded at this power level, showing strong holmium (and related) peaks with smaller peaks belonging to carbon cluster ions. The bunch lengths measured as the full width at half maximum are slightly larger than 1 µs. In the shown mass range, this corresponds to a resolving power of $m/\Delta m \approx 40$. This is sufficient to completely separate neighboring carbon cluster ions, while ions with a mass difference smaller than 5 u are distinguishable but not completely separated.

4.2 Measurement procedure

In the measurement cycle to determine the free cyclotron frequency ν_c, the ions were first captured in the preparation Penning trap, mass separated by resonant buffer-gas cooling [55], and then transfered to the measurement Penning trap. There, the frequency measurement was carried out using the Time-of-Flight Ion Cyclotron Res-

onance technique (ToF-ICR). The technique is described in detail in several publications, for example in [57] and [58]. It is based on the conversion of motion from the slow magnetron motion (with frequency ν_-) into the fast modified cyclotron motion (with frequency ν_+). This conversion is excited by a quadrupolar RF excitation on the sideband of the sum of the two frequencies $\nu_- + \nu_+$. As described in [59], in an ideal Penning trap this sideband frequency equals the free cyclotron frequency ν_c. Thus, in ideal cases only one frequency measurement is needed instead of the measurement of all three frequencies ν_-, ν_z, ν_+ to determine ν_c by the Brown-Gabrielse invariance theorem $\nu_c^2 = \nu_-^2 + \nu_z^2 + \nu_+^2$ [60]. Obviously, the application at real Penning traps introduces limitations, but these are mostly understood and can be corrected to achieve relative uncertainties below 10^{-8} [61]. The conversion is then probed by the interaction of the ions magnetic moment μ due to radial motion with the gradient of the magnetic field. When ejecting an ion through the magnetic field gradient to the detector, it experiences an axial force

$$\vec{F} = -\mu \nabla \vec{B}. \tag{4.1}$$

This results in a gain of for forward kinetic energy proportionally to their magnetic moment

$$\mu = \frac{1}{2} q \sum_i 2\pi \nu_i r_i^2 \tag{4.2}$$

given by the orbital frequencies ν_i and radii r_i of the respective motions. After a full conversion from magnetron to modified cyclotron motion, the final radius of motion r_+ matches the initial radius r_-, but the much larger orbital frequency translates to

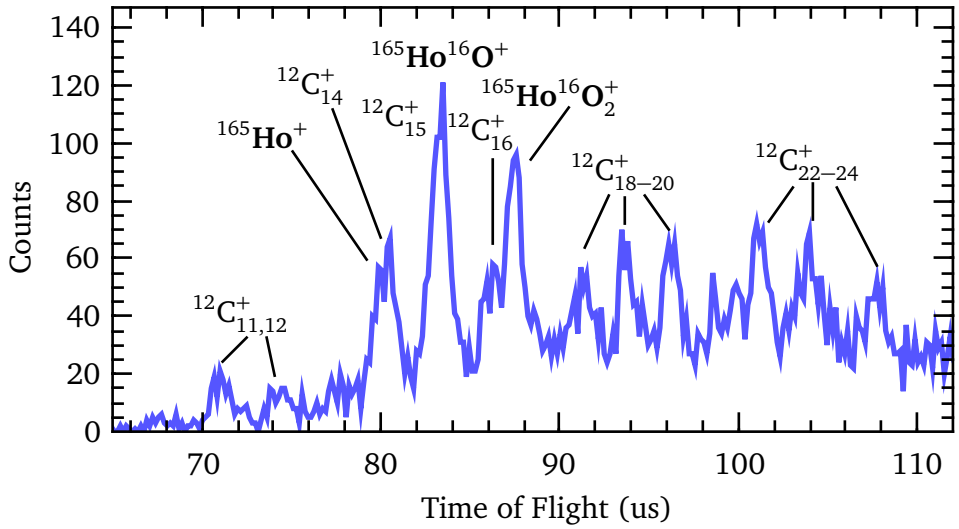

Figure 4.1: Time of flight distribution of ions created in the Mini-RFQ ion source recorded with the MCP detector in front of the Penning traps. The sample was stable holmium nitride on SIGRADUR. Adapted from [21].

Table 4.2: Durations and amplitudes for the resonant buffer-gas cooling in the preparation trap and the ToF-ICR measurement of ν_c in the precision trap.

Parameter		Value
Preparation trap	Cooling delay	300 ms
	Magnetron excitation	10 ms
		1.7 V
	ν_c excitation	1000 ms
		1.0 V
	Ejection delay	100 ms
Precision trap	Initial delay	0.01 ms
	Magnetron excitation	10 ms
		200 mV
	ν_c excitation	$2 \cdot 200$ ms
		47 mV
	Ramsey interval	1600 ms
	Ejection delay	≈ 0.3 ms

a much larger μ. Thus, the determination of ν_c with the ToF-ICR method is based on identifying the excitation frequency for which the time of flight to the detector is minimum.

After capturing the ions in the purification trap, they are stored for a short duration to dissipate their initial axial energy by buffer-gas collisions. Afterwards, the excitation pattern for the resonant buffer-gas cooling is applied, with the values given in tab. 4.2. The ν_c excitation was optimized with a buffer-gas flow of 10^{-5} mbar/(l s). Faster cooling would be possible with higher gas flows but at the cost of an increased pressure in the precision trap. With these settings, a FWHM of the cooling resonance of 11.6 Hz could be achieved. In terms of mass, this translates to a mass resolving power of $m/\Delta m \approx 50000$, *i.e.*, the ability to resolve a mass difference of 3.3 MeV in the given region around 180 u. This was sufficient to exclude possible isobaric contaminant ions to enter the precision trap, but by far not enough to distinguish between ^{163}Ho^{16}O$^+$ and ^{163}Dy^{16}O$^+$.

In the precision Penning trap, a 10 ms RF pulse with 200 mV amplitude at the magnetron frequency $\nu_- = 1140.10$ Hz was applied to increase the ion orbit to an initial radius of approximately 0.1 mm. The RF pulse to convert the magnetron motion into the modified cyclotron motion was split into two 0.2 s pulses with a 1.6 s delay in between, a so called Ramsey excitation pattern [62]. The necessary amplitude for a full conversion was 15 mV, supplied by a 1.5 V output amplitude and a subsequent power attenuation by 30 dB. The RF frequency was scanned in steps of 0.05 Hz over a range

of ±1 Hz around the value for ν_c previously determined in a lower resolution measurement with 0.2 s continuous excitation. For one ν_c measurement, the frequency range was typically scanned 20 to 25 times, taking about one hour in total. Figure 4.3a shows a time of flight spectrum of $^{163}Ho^{16}O^+$ recorded this way. The complete experimental setup proved to be very stable and no retuning of parameters was required for several days. The only necessary change concerned the laser ablation in the Mini-RFQ ion source. To keep the number of detected ions per pulse in the desired range between one and five, the ablation pulse energy or the target rotation angle needed to be slowly adapted to counteract the local sample depletion.

For the determination of the atomic masses of ^{163}Ho and ^{163}Dy, this ν_c measurement pattern was applied cyclically to $^{12}C_{15}^+$, $^{163}Ho^{16}O^+$ and $^{163}Dy^{16}O^+$, with first and final measured ion being $^{12}C_{15}^+$. In this way, certain time dependent changes in the magnetic field and thus in ν_c could be compensated by interpolating ν_c for the reference ion between two successive measurements in the frequency ratio calculation. In total 32 frequency ratios were recorded for each of the isotopes.

In a second measurement phase, ν_c of $^{163}Ho^{16}O^+$ and $^{163}Dy^{16}O^+$ was measured in an alternating fashion without a reference measurement. This served the purpose of acquiring a larger number of direct frequency ratios between the two isotopes to test the possible uncertainty with which Q_{EC} could be determined.

Furthermore, as consistency check, ν_c was measured for three carbon cluster ion species $^{12}C_{14}^+$, $^{12}C_{15}^+$ and $^{12}C_{16}^+$ in the same cyclic fashion as before. Due to the known masses of the three isotopes, any deviations beyond the statistical uncertainties can be attributed to systematic effects. By analyzing three different carbon cluster ions, linear shifts in the frequency ratios can be quantified and corrected in the other cases.

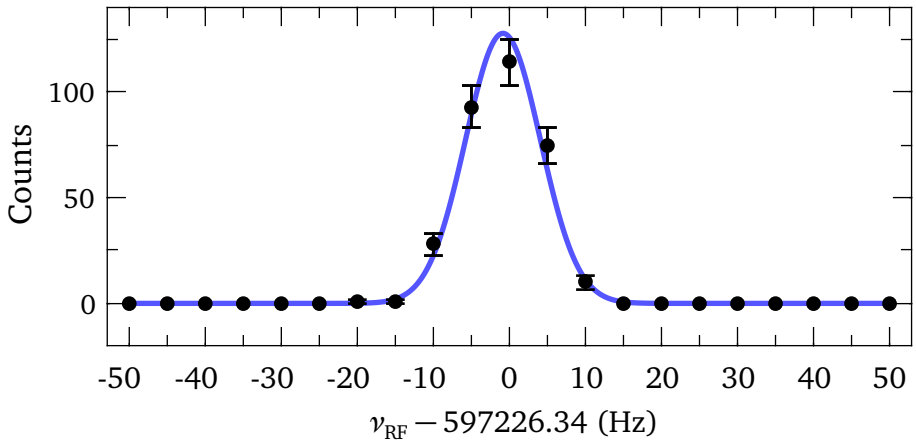

Figure 4.2: Mass-selective resonant buffer-gas cooling spectrum recorded in the preparation Penning trap with $^{12}C_{15}^+$ ions. Except for an RF excitation in a range of ±15 Hz around ν_c, no ions are transmitted through the diaphragm to the detector.

4.3 Data evaluation

In the evaluation processes for either the atomic masses or the Q-value, the cyclotron frequency ratio r has to be determined from the time-of-flight spectra. For this purpose, ν_c was obtained from each recorded spectrum by curve fitting. Subsequently, r was evaluated as the ratio of ν_c for the two ion species. Finally, from all frequency ratios r, a weighted average was composed.

In detail, each time-of-flight spectrum spans over 41 equidistant frequency values in a range of 4 Hz and for each value about 20 to 25 individual trapping cycles were performed. To keep systematic influences small, not all cycles and all detected ions were taken into account for the fitting procedure. In case of ions of a contaminant species stored in parallel, ion-ion Coulomb interaction induces shifts in the measured cyclotron frequency [59, 63, 64]. For ions with a frequency difference smaller than the measurement resolution, the measured frequencies shift towards each other[1]. For species with larger frequency differences, in addition to approaching each other, the measured frequencies decrease. In both cases, the magnitude of the shifts is proportional to the number of contaminating ions in the trap. As such, to eliminate these shifts only those trapping cycles with a single trapped ion should be taken into account. But, with an estimated detection efficiency of 30 %, the number of ions in the precision trap is about three times larger than the number of detected ions and these cycles cannot be unambiguously identified. Another option is to separate the recorded trapping cycles into classes by the number of detected ions and perform the fitting procedure for each of those classes. The unperturbed value of ν_c for a single ion can then be extracted by extrapolation to a single trapped ion, *i.e.*, 0.3 detected ions. But splitting the data into several classes increases the relative uncertainties of the fits in each of the classes and in consequence for the extrapolated value as well. Thus, a large dataset of detected ions is necessary. To be able to work with a smaller total ion count, a compromise was taken in this work: Out of all trapping cycles, only those with one or two detected ions were taken into account in the fitting procedure. The frequency shift is therefore not eliminated, but is expected to be smaller than the statistical uncertainty of the fit. Figure 4.3a shows a recorded spectrum for $^{163}Ho^{16}O^{+}$ with the fitted curve in blue. The time of flight distributions for non-converted ions as well as fully converted ions are shown in fig. 4.3b, highlighting that not only the mean time of flight decreases, but also the width of the distribution.

The theoretical line shape used for the curve fitting is based on the flight time of

[1] In the limit case of a vanishing frequency difference, *i.e.* identical ions, no frequency shift at all occurs with increasing ion numbers.

an ion from the trap center at $z = 0$ to the detector at $z = z_{\mathrm{Det}}$ [65]

$$T_{\mathrm{total}}(\nu_{\mathrm{RF}}) = \int_0^{z_{\mathrm{Det}}} \sqrt{\frac{m}{2(E_0 - qU(z) - \mu(\nu_{\mathrm{RF}})B(z))}}\, dz \tag{4.3}$$

dependent on the initial axial energy E_0, the electric potential $U(z)$ and magnetic field strength $B(z)$ along the drift line. The key parameter is $\mu(\nu_{\mathrm{RF}})$, the ions magnetic moment which in turn depends on the amplitudes and rotational frequencies of its motion:

$$\mu = \frac{2\pi q}{2}(r_+^2 \nu_+ + r_-^2 \nu_-) \tag{4.4}$$

If the ion performed a pure magnetron motion before the quadrupolar excitation, *i.e.*, $r_+ = 0$, the magnitude of μ depends on the degree of conversion achieved by the quadrupolar excitation because of the large difference in motional frequencies $\nu_+ \gg \nu_-$. Mathematically, the degree of conversion F after a quadrupolar excitation with a Ramsey-like pattern of two excitations of duration τ_1, separated by a waiting

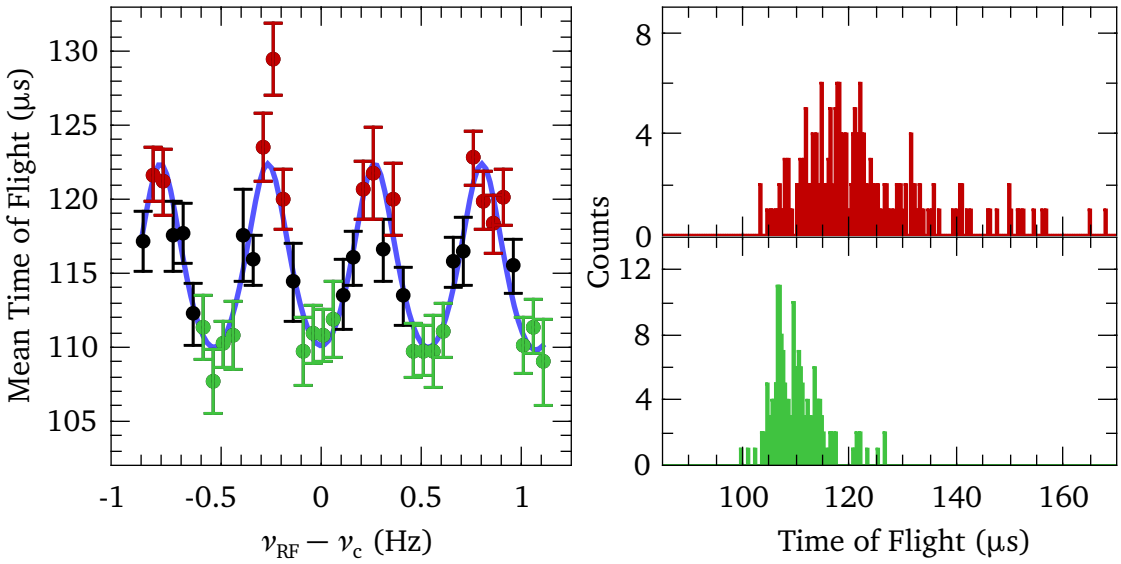

(a) ToF-ICR spectrum of $^{163}Ho^{16}O^+$.

(b) Time of Flight distributions.

Figure 4.3: Time of Flight Ion Cyclotron Resonance (ToF-ICR) spectrum of $^{163}Ho^{16}O^+$ recorded with a Ramsey excitation pattern with two 0.2 s long RF pulses split by 1.6 s. The time of flight distributions depicted in (b) are cumulated for excitation frequencies at which the ions perform a pure magnetron motion (red, upper panel) and frequencies at which a full conversion to a modified cyclotron motion has been achieved (green, lower panel).

time τ_0, can be obtained from Bloch vector calculations as

$$F(\delta = \nu_{RF} - \nu_c, \tau_0, \tau_1, g) = \frac{16g^2}{\Omega_R^2} \sin^2\left(\frac{\Omega_R \tau_1}{2}\right)\left(\cos\frac{\delta\tau_0}{2}\cos\frac{\Omega_R\tau_1}{2} - \frac{\delta}{\Omega_R}\sin\frac{\delta\tau_0}{2}\sin\frac{\Omega_R\tau_1}{2}\right)^2, \quad (4.5)$$

with the Rabi frequency of the excitation $\Omega_R = \sqrt{4g^2 + \delta^2}$ and the coupling constant g, which is proportional to the amplitude of the excitation [62]. The combination of these equations, as well as the evaluation of the integral in eq. (4.3) using measured data for the electric and magnetic field at TRIGA-TRAP is carried out by the software *EVA*[2]. Finally, the line shape is described by the free parameters $\nu_c, F_{max}, r_-, \tau_1, \tau_0$ and T_{offset}, an arbitrary offset to the recorded time of flights. τ_1 and τ_0 are defined by the chosen excitation pattern, whereas the other four parameters are determined by the curve fitting. Although F_{max}, r_- and T_{offset} do not directly influence the evaluation procedure, their values can serve as sanity check during curve fitting or by correlation to ν_c can reveal systematic errors. In these measurements, their typical values are $F_{max} = 0.8 \ldots 1.4, r_- = 0.08 \ldots 0.14$ mm and $T_{offset} = 118 \ldots 126\,\mu$s, as can be seen in figs. B.1, B.2 and B.3 in the appendix. Furthermore, no correlation between any two parameters or ν_c could be identified.

From the dataset of obtained values and uncertainties of ν_c, the frequency ratio for each pair of ions has to be calculated. Because the reference measurements with ions of precisely known mass serving as magnetic field measurement can not be performed in parallel to the ν_c determination of the ion of interest, an interpolated value is used for $\nu_{c,ref}$ of the reference ion. In this way slow, linear changes in the magnetic field strength can be compensated (for a more detailed analysis of the interpolation routine, see [63]). Figure 4.4 shows the obtained values for ν_c of $^{163}Ho^{16}O^+$ and $^{12}C_{15}^+$ from the first day of measurements. Out of these nine frequency measurements, four frequency ratios were extracted, each corresponding to one ^{163}Ho measurement and an interpolated value of two $^{12}C_{15}^+$ measurements. In total, a set of 32 frequency ratios was collected for both $^{163}Ho^{16}O^+$ to $^{12}C_{15}^+$ and $^{163}Dy^{16}O^+$ to $^{12}C_{15}^+$ and 41 ratios for $^{163}Ho^{16}O^+$ to $^{163}Dy^{16}O^+$. The final values were calculated as the weighted average. The uncertainty was obtained from the external error, *i.e.*, from the variation of the individual ratios, because in all cases it was larger than the internal error obtained from error propagation. The ratio χ^2 of the external to the internal error was between 1.5 and 1.8, which has to be caused by external fluctuations causing changes in the measured ν_c not being covered by the statistical uncertainties. Possible effects include magnetic field fluctuations faster than could be tracked with the set of reference measurements.

[2] *EVA* is part of the mass measurement software suite maintained by the LEBIT group of the Michigan State University (`https://groups.nscl.msu.edu/lebit/downloads/index.html`). In this work, EVA 6.1.4.0 was used.

4.4 Results

4.4.1 Calibration with carbon cluster ions

The evaluation of the frequency ratios for the combinations of carbon cluster ions is performed first, to be able to identify significant systematic deviations. The measured frequency ratios r presented in table 4.3 can be compared to the nominal ratios based on the known masses of the carbon cluster ions (under neglection of binding energies) $m(^{12}C_n) = n \cdot 12\,\mathrm{u} - m_e$:

$$\Delta r = r - \frac{n_2 \cdot 12\,\mathrm{u} - m_e}{n_1 \cdot 12\,\mathrm{u} - m_e} \tag{4.6}$$

Furthermore, a relative shift ξ of the ratios dependent on the mass difference $\Delta m = (n_2 - n_1) \cdot 12\,\mathrm{u}$ between the two carbon cluster ions can be extracted:

$$\xi = \frac{\Delta r}{r \cdot (n_2 - n_1) \cdot 12\,\mathrm{u}} \tag{4.7}$$

m_e is the electron mass and would need to be multiplied by the charge state q for non-singly-charged ions. Its relative uncertainty of $3 \cdot 10^{-11}$ is of no significance here. The evaluation of the measured frequencies yield in only one case a ξ consistent with 0, whereas in the other two cases a significant shift was obtained. The error weighted mean of the three values is $8(3) \cdot 10^{-10}\,\mathrm{u}^{-1}$. Such a shift can have different sources, for example mass independent shifts of the measured free cyclotron frequency ν_c caused by an anharmonicity of the measurement trap or a misalignment between trap axis

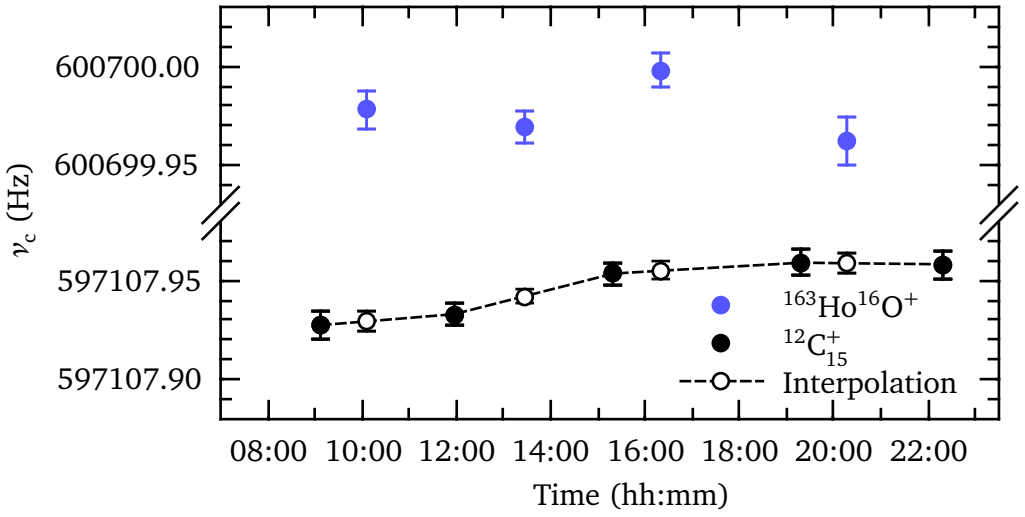

Figure 4.4: Cyclotron frequencies obtained for $^{163}Ho^{16}O^+$ (blue points) and $^{12}C_{15}^+$ (black points) on the first day of measurements. The empty points represent the interpolated value of ν_c used in the frequency ratio evaluation. In between the measurements of $^{163}Ho^{16}O^+$ and $^{12}C_{15}^+$, $^{163}Dy^{16}O^+$ was measured which was omitted for clarity.

Table 4.3: Frequency ratios and mass dependent shifts obtained in the calibration measurements with carbon cluster ions $^{12}C^{+}_{14-16}$.

Target Ion	Reference Ion	Ratio $r = \frac{\nu_{c,ref}}{\nu_{c,ion}}$	deviation from nominal $\Delta r/10^{-10}$	mass dependent shift $\xi/(10^{-10}u^{-1})$
$^{12}C^{+}_{15}$	$^{12}C^{+}_{14}$	1.071 428 815 0(76)	103(76)	8(6)
$^{12}C^{+}_{16}$	$^{12}C^{+}_{15}$	1.066 666 869 2(95)	−6(95)	−1(7)
$^{12}C^{+}_{16}$	$^{12}C^{+}_{14}$	1.142 857 632 7(77)	234(77)	8(3)

and magnetic field [61]. As given in [63] a shift $\Delta\nu$ causes a relative change in the frequency ratio r:

$$\frac{\Delta r}{r} = \frac{\Delta\nu\,(\nu_{ref}-\nu_{ion})}{\nu_{ref}^2}\frac{\nu_{ref}}{\nu_{ion}} \tag{4.8}$$

$$= \frac{2\pi}{qB}\cdot\Delta\nu\cdot(m_{ion}-m_{ref}) \tag{4.9}$$

For example, in case of an axis misalignment by an angle θ, $\Delta\nu$ is given by

$$\Delta\nu^{mis} \approx \nu_{-}\cdot\frac{9}{4}\theta^2. \tag{4.10}$$

Combining eqs. (4.9) and (4.10) then allows the calculation of θ:

$$\theta^2 = \frac{qB}{2\pi}\frac{4}{9\nu_{-}}\frac{\Delta r}{r\cdot(m_{ion}-m_{ref})} \tag{4.11}$$

$$= \frac{4\,m_{ref}\;\nu_{ref}}{9\nu_{-}}\cdot\xi \tag{4.12}$$

By evaluating with the magnetron frequency of the measurement trap $\nu_{-} = 3103\,\mathrm{Hz}$ and $\xi = 8(3)\cdot10^{-10}\,u^{-1}$ one obtains $\theta = 34(7)\,\mathrm{mrad} = 0.20(4)^\circ$ under the assumption that a misalignment is the only source for a mass dependent shift. For the evaluation of the atomic masses of ^{163}Ho and ^{163}Dy, the effect of such a frequency shift is smaller than 10^{-9}, because the mass difference between the ions of interest and the reference ion is only 1 u. Therefore, no further investigation upon the actual cause was carried out, nevertheless, the effect is being considered in the following analysis.

4.4.2 Atomic masses of ^{163}Ho and ^{163}Dy

For the determination of the atomic masses of ^{163}Ho and ^{163}Dy, frequency ratios were recorded using $^{163}Ho^{16}O^{+}$ and $^{163}Dy^{16}O^{+}$ ions, respectively. Therefore to extract the atomic masses, not only the missing electron from the ions has to be considered but in addition the additional oxygen atom. As already mentioned in sec. 4.1, ^{16}O is known with a relative uncertainty of 10^{-11} and its atomic mass was determined to

Table 4.4: Results of the atomic mass measurements of ^{163}Ho and ^{163}Dy. The given frequency ratios include a correction for a mass dependent shift. The literature values M_{AME} are the recommended values from the Atomic Mass Evaluation [35].

Target Ion	Reference Ion	Ratio $r = \frac{\nu_{\mathrm{c,ref}}}{\nu_{\mathrm{c,ion}}}(1+\xi)$	Atomic mass M/u	Difference to AME $(M - M_{\mathrm{AME}})$/u
^{163}Ho^{16}O$^+$	^{12}C$_{15}{}^+$	0.994 020 279 2(53)	162.928 738 92(96)	$-2.1(22)\cdot 10^{-6}$
^{163}Dy^{16}O$^+$	^{12}C$_{15}{}^+$	0.994 020 265 6(48)	162.928 736 47(87)	$-1.8(22)\cdot 10^{-6}$

be $m(^{16}\mathrm{O}) = 15.994\,914\,619\,57(18)\,\mathrm{u}$ [66]. As such, it can be treated as absolute and without significant influence on the uncertainty of the evaluated atomic masses. Table 4.4 lists the determined frequency ratios, including the mass dependent shift correction. The atomic mass M is calculated from the determined frequency ratios given as

$$M = r \cdot (15 \cdot 12\,\mathrm{u} - m_{\mathrm{e}}) - m(^{16}\mathrm{O}) + m_{\mathrm{e}}. \tag{4.13}$$

Finally, a comparison to the recommended values in the atomic mass evaluation 2012 of G. Audi and M. Wang et al. [35] is made. They report an uncertainty of the atomic mass of $2.0 \cdot 10^{-6}$ u in both cases, and an absolute value which is $2.1 \cdot 10^{-6}$ u heavier in the case of ^{163}Ho and $1.8 \cdot 10^{-6}$ u for ^{163}Dy, respectively. As such, they do not disagree with the new values measured in this work. With respect to the uncertainty, the newly measured values are slightly more than a factor of two more precise. It should be noted, that with the network based approach of the atomic mass evaluation, the atomic masses of the two nuclides are strongly coupled by their mass difference, *i.e.*, Q_{EC}, which is reported as 2.555(16) keV. In this work, the two atomic masses were explicitly not coupled and completely independently evaluated because of the discrepancies in the literature regarding Q_{EC}. The difference of the atomic masses given here is $m(^{163}\mathrm{Ho}) - m(^{163}\mathrm{Dy}) = 2.4(12)\,\mathrm{keV}$.

4.4.3 Electron capture Q-value of ^{163}Ho

Although the ToF-ICR method as applied at TRIGA-TRAP is associated with relative uncertainties of at least 10^{-9}, an approach to measure Q_{EC} of ^{163}Ho was taken. The expected result was not supposed to compete with the existing values in literature, for which a relative uncertainty below 10^{-10} would be needed, but to serve as a benchmark of what the achievable uncertainty at TRIGA-TRAP in its current state is. The measurement principle was the same as with the atomic masses before, except that only the two ions of the nuclides of interest were analyzed. In addition to the cyclotron frequencies measured for the evaluation of the atomic mass, an additional set of frequency data was recorded to have a larger dataset. In this way, 41 frequency ratios

were recorded in total as shown in fig. 4.5, with a mean value of $r = 1+1.15(33)\cdot10^{-8}$. Calculating Q by

$$Q = (r-1)\cdot(m(^{163}\mathrm{Dy}) + m(^{16}\mathrm{O}) - m_e) \tag{4.14}$$

results in $Q = 2.51(71)\,\mathrm{keV}$. This is in good agreement with literature values (of either $\approx 2.5\,\mathrm{keV}$ or $\approx 2.8\,\mathrm{keV}$) as well as with the difference of the determined atomic masses. But in comparison the indirect determination through the mass difference, no uncertainty from mass dependent shifts had to be considered in this direct measurement. Furthermore, the difference of the two independently measured masses carries a larger uncertainty from error propagation. Together with the increased dataset of 41 versus 32 frequency ratios, the uncertainty of Q is about 40 % smaller.

4.5 Conclusion

The measurement campaign proved to be very successful, with all goals being reached. A precise determination of the atomic masses of ^{163}Ho and ^{163}Dy was carried out with a relative uncertainty of $6\cdot10^{-9}$. The Q-value of the electron capture decay of ^{163}Ho was measured as well, with an even lower relative uncertainty in the frequency ratios of $4\cdot10^{-9}$. The calibration with different carbon cluster ions revealed a mass dependent shift in the measured frequency ratios, albeit a minor one which could be quantified and corrected for. The final task of establishing the quality of the ^{163}Ho samples and the Mini-RFQ ion source for Penning trap mass measurements was fulfilled as well. No indication of a contamination of ^{163}Dy in the ^{163}Ho sample was observed, for example no trend to larger or smaller frequency ratios over time is visible in fig. 4.5, which would be caused by an increasing cross contamination of the sample caused by laser

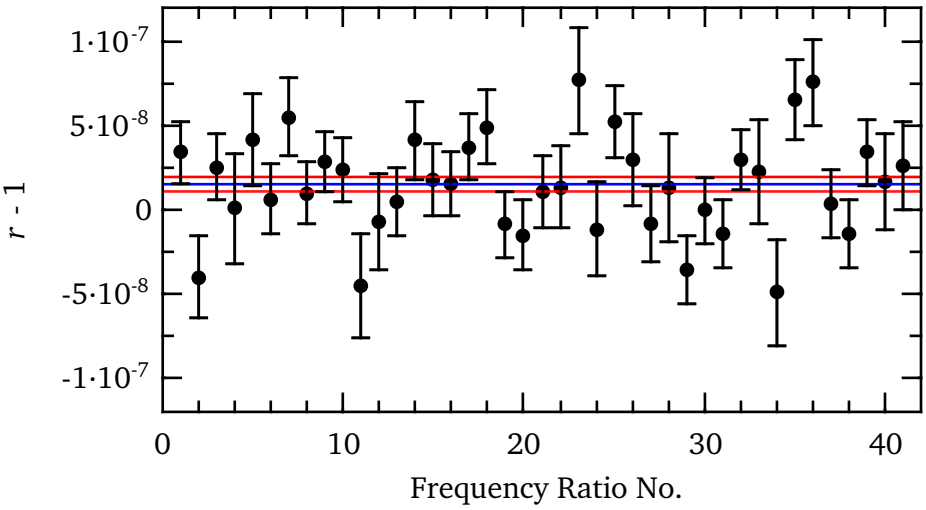

Figure 4.5: Cyclotron frequency ratios obtained for ^{163}Ho^{16}O$^+$ to ^{163}Dy^{16}O$^+$. The blue and red lines mark the mean value of $r = 1 + 1.51(43)\cdot10^{-9}$ and its uncertainty.

ablation. And with the increased yield of the Mini-RFQ ion source, only a fraction of the prepared $6 \cdot 10^{16}$ atoms had to be used as can be seen from the laser trace in fig. 3.3 not completely intersecting the sample spots.

The newly measured atomic masses nicely supplement the data from the atomic mass evaluation [35]. In the listed data, a large stretch of elements in the lanthanide region is apparent, in which no isotope was studied with an uncertainty below $1 \cdot 10^{-8}$. Shown in fig. 4.6 are the isotopes with the lowest relative uncertainty in its mass $\delta M/M$ for the elements from barium to mercury. Here, the new data can serve as anchor points for the network and thereby decrease the uncertainty of neighboring isotopes, if sufficiently precise connections can be made.

The high sample quality made a follow-up measurement at SHIPTRAP feasible, where the Q-value was measured with high accuracy using the new phase-imaging ion-cyclotron-resonance technique [37, 67]. The resulting value of the successful run was $Q = 2.833(30)_{\text{stat}}(15)_{\text{sys}}$ keV. Therefore, the discrepancy between the latest calorimetrically determined values from Ranitzsch *et al.* [27] and Lusignoli *et al.* [44] around 2.80 keV and the previously determined values from Hartmann *et al.* [25] and Bosch *et al.* [42] of 2.55 keV seems to be resolved, as the new value clearly confirms the former. A final, ultra-high precision determination with an uncertainty in the eV range is foreseen at the PENTATRAP setup [68, 69] at the Max-Planck-Institute for Nuclear Physics in Heidelberg, Germany, which is currently under commissioning. In contrast

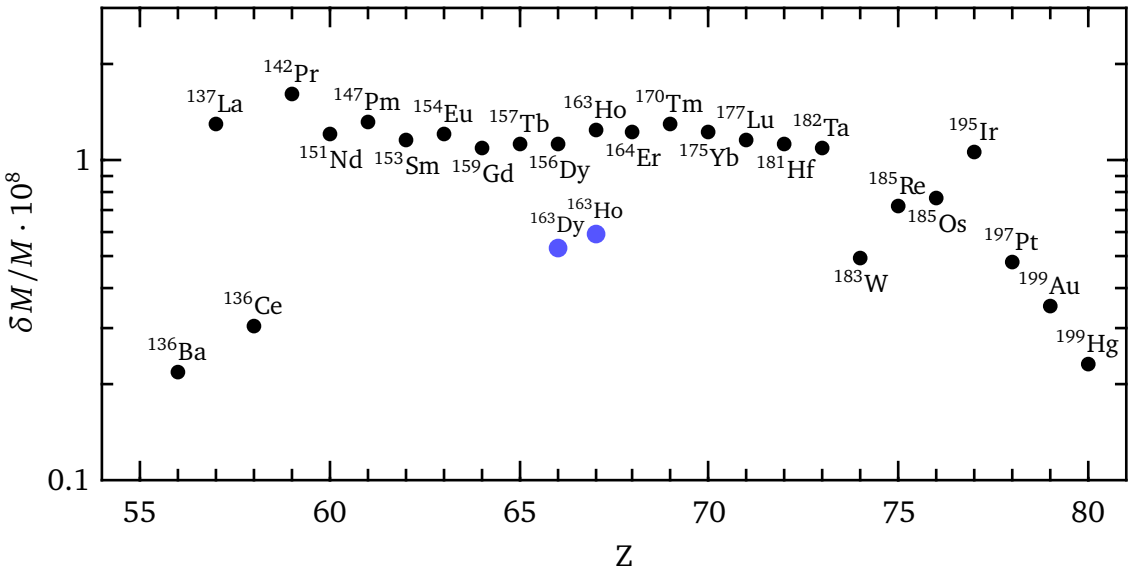

Figure 4.6: Overview of the isotopes with the lowest relative uncertainties in the atomic mass $\delta M/M$ for each of the elements from Ba (Z=56) to Hg (Z=80) as reported in the Atomic Mass Evaluation 2012 [35]. Plotted in blue are the values determined in this work.

to TRIGA-TRAP and SHIPTRAP, highly charged ions produced in an electron beam ion trap will be used to achieve the desired precision. One of the specific difficulties of this Q-value determination will be the ion production, because typically the efficiency from a given sample to ions in high charge states is very low, and the available sample amount is very limited in the case of ^{163}Ho.

Part II

Implantation of ultrapure Ho in Microcalorimeter Arrays

The first ^{163}Ho production and implantation run at ISOLDE made clear that the combined isotope production and ionization only has a rather small yield and introduces significant radioactive contaminations [27]. To improve this, the ^{163}Ho implantation will be carried out after production in a high flux nuclear reactor and a subsequent chemical purification by high-performance liquid chromatography. For the implantation, an ion source and mass separator setup is required that is able to produce nearly isobar-free ion beams. Although in principle possible at ISOLDE, future implantations and development work is handed over to be carried out at the mass separator RISIKO at Mainz. This choice has several advantages: the use of resonant laser ionization, ample available beamtime and the close proximity to the Institute of Nuclear Chemistry. With resonant laser ionization, highest ionization efficiency can be achieved, especially for lanthanide elements, combined with unique element-selectivity. This ideally suits the requirements of ECHo to implant a contamination free ^{163}Ho ion beam. Beyond that, RISIKO was designed with the ISOLDE general purpose separator in mind and has rather similar performance in mass separation. Dedicated operational time for ECHo sample treatment and corresponding adaptations can be allocated in larger amounts compared to ISOLDE, where beamtime is heavily overbooked. Finally, RISIKO is located at the Institute of Physics of the University of Mainz and as such on the same campus as the Institute of Nuclear Chemistry which removes the need of shipping the radioactive samples. These aspects make RISIKO the optimum platform to perform the implantation of about 1 kBq of ^{163}Ho in the first phase of the ECHo experiment. During this time the process can be assessed for upscaling towards the full scale ECHo experiment with a total activity of 1 MBq.

The following chapters outline the RISIKO experimental setup (chap. 5) and present the first evaluations of the ionization, mass separation and implantation processes (chap. 6). Based on the findings, several possible improvements to the process were identified and implemented, which are presented in chap. 7 together with an outlook on the future performance. Parts of the work presented in these chapters was carried out in close collaboration with undergraduates and is therefore also part of these respective theses [70–75]. The results of the sample preparation and ionization efficiency determination have been published by in [76], out of which several figures are reproduced with kind permission of Elsevier publishing.

Chapter 5

RISIKO Experimental Apparatus

The mass separator setup RISIKO was designed and installed at the institute of physics of the university of Mainz in 1990 [77] with the task of performing ultra-trace analysis on strontium isotopes ^{89}Sr and ^{90}Sr, that gathered large interest in the wake of the 1986 Chernobyl nuclear accident. A concept was developed involving high efficiency surface ionitation, mass separation and reneutralization of the ions in a charge exchange cell to meet the required demanding specifications in sensitivity and selectivity with an isotopic ratio well below 10^{-10} in respect to dominant ^{88}Sr. Collinear resonant laser ionization on a fast atomic beam served as dedicated isotope selective ion counting [78][1]. After successful demonstration of the technique, the collinear laser spectroscopy setup was dismantled around the year 2000 and the main usage of RISIKO shifted towards the development of resonant laser ionization ion sources. An overview of the layout is shown in fig. 5.1. The setup consists of four key components: an ion source, ion optics including the separator magnet, ion detection and a laser system. The following chapters will describe these individual parts in detail.

[1] Hence the name as abbreviation for the German descriptor ***R**esonanz**i**onisations**s**pektroskopie **i**n **ko**llinearer Geometrie*

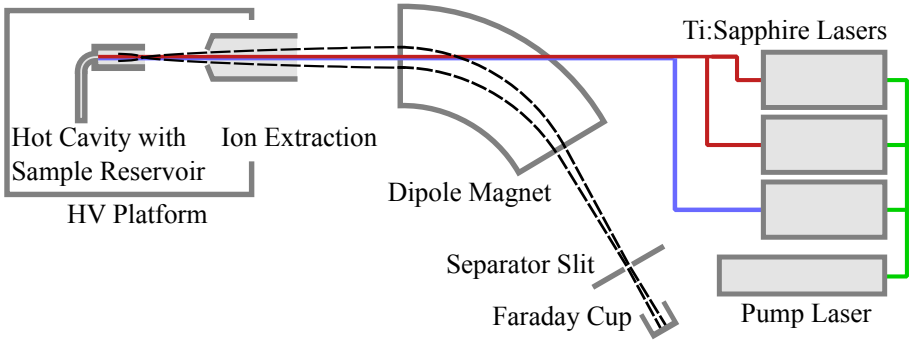

Figure 5.1: Schematic view of the RISIKO mass separator. Taken from [76].

5.1 Resonant laser ionization ion source

The ion source region was designed as a copy of the ISOLDE II ion source. As such it features a modular design, allowing different ion sources to be installed in the ion source vacuum vessel, as well as a quick exchange of the complete ion source vessel by the use of a special connector flange. For the work described here, the regular combination of a tantalum atomizer and sample reservoir was installed. Figure 5.2 shows a technical drawing of the ion source, made up of a tantalum atomizer tube and a tantalum capillary serving as sample reservoir. The parts are mounted at their respective ends and at a combined mounting point where the reservoir is connected to the atomizer. These three mounting points further serve as electrical contacts for individual resistive heating of the parts. A current of typically 250 and 300 A is sent through the atomizer in this way to reach temperatures of up to 2200 °C. The sample reservoir is heated in a similar manner with currents up to 100 A to reach the same temperature.

5.2 Ion optics and separator magnet

The ion source region, including the high current power supplies are all situated on a high voltage insulated platform. This high voltage of typically 30 kV is then used to accelerate ions created in the ion source towards the mass separator. The acceleration is done in two steps with a first extraction electrode 40 mm after the ion source at an intermediate potential of 19 kV and a second acceleration stage afterwards, in which the ions reach the full 30 keV kinetic energy. The intermediate potential is chosen to create a slightly divergent beam which is collimated by an einzel lens. In this way, a large diameter, parallel beam can be achieved, maximizing the obtainable mass res-

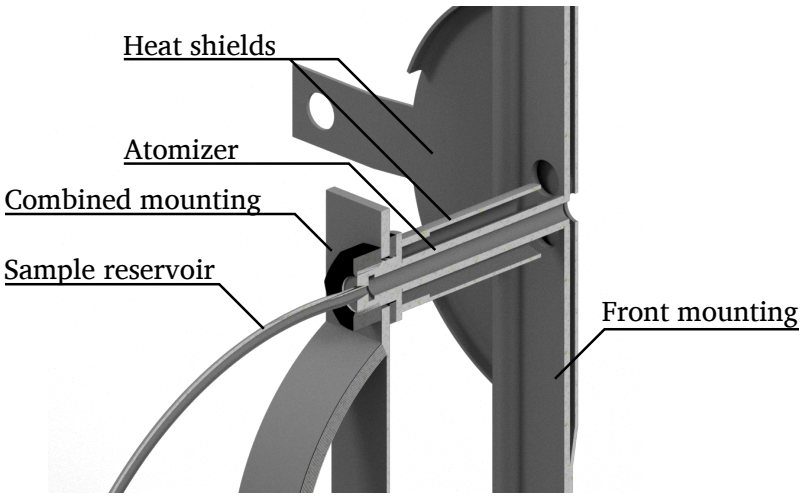

Figure 5.2: Computer rendered view of the ion source region.

olution of the magnet. A set of parallel plate deflectors can be used to steer the ion beam to correct for slight geometrical misalignments. Detailed drawings of the parts can be found in [79].

The separator magnet is a 60° deflection angle, homogeneous field dipole magnet with a bending radius of 750 mm. It allows for a maximum field strength of 0.52 T, which is sufficient to separate singly charged ions with 30 keV energy up to masses of 240 u. It was designed by Danfysik[2] as double focusing type by tilting the entry and exit faces by 14.7° and 18.0°, respectively. The asymmetric angles are chosen to minimize second order imaging aberrations when used with a collimated incoming beam. Due to machining imperfections the angles actually slightly deviate and are 14.2° and 17.2°. This leads to calculated focal lengths of $f_x = 1043\,\text{mm}$ and $f_y = 1147\,\text{mm}$. Further features of the dipole magnet are a pole gap of 50 mm, approximated Rogowski-chamfered pole edges and field shunts in 50 mm distance with a 50 mm gap, designed to match the effective field boundary to the physical pole faces (for more information on the effect of these parameters in dipole magnet design, see [80]).

The actual mass separation is achieved by a slit positioned at the horizontal focus position behind the magnet. The slit width is adjustable between 0.5 mm and 10 mm, with a typical size of 1.5 mm, which maximizes the mass resolution without significant losses in transmission. To accommodate the astigmatic focusing, the beam is not confined in the vertical direction.

5.3 Ion detection

Directly behind the mass separation slit, a Faraday cup is installed for beam monitoring. It is fitted with a ring electrode set to 30 V to suppress secondary electrons. Furthermore, it is mounted on a retractable arm with pneumatic control to quickly insert it into the beam or remove it when needed. About 500 mm downstream, the beamline ends in the detector chamber. Here, either a secondary electron multiplier for single ion detection or another Faraday cup with a diameter of up to 50 mm can be installed. In this work, a dedicated Faraday cup assembly was used to directly mount the ECHo detector chips for ion implantation.

As a consequence of the first ion implantation studies presented in sec. 6.4, the ion detection region was redesigned to incorporate additional focusing and steering ion optics, as well as an independent vacuum generation with the ability to close off the connection to the RISIKO beam line. In this way, faster venting and pumping cycles for the exchange of the implantation target are ensured. These changes are described in sec. 7.3.

[2] Danfysik A/S, Denmark `http://www.danfysik.com/`

5.4 High-repetition Ti:sapphire laser system

Closely linked with the development of resonant laser ion sources in Mainz is the corresponding laser system. It employs Ti:sapphire lasers that are pumped by high-repetition rate, frequency doubled Nd:YAG lasers. The main advantage of this configuration is the ultra-broad tuning range of the Ti:sapphire medium, ranging from below 700 to above 950 nm. Combined with a three stage wavelength selection, involving mirror reflectivity ranges, a Lyot-filter and a Fabry-Pérot etalon, it delivers output pulses around 300 µJ with a duration of 50 to 100 ns and a spectral width of 3 to 5 GHz. The latter nicely matches the typical Doppler broadened transition bandwidths of atoms in a 2000 °C hot cavity. In addition, together with a high beam quality, the pulse energy is sufficient for a reliable single pass generation of higher harmonics in non-linear optical crystals, *e.g.*, β barium borate (BBO) crystals. With the generation of second, third and fourth harmonics, the wavelength range is extended from 460 nm down to 200 nm. Finally, the high repetition rate of 10 kHz dictated by the pump laser nearly guarantees the interaction of each atom with at least one laser pulse in the atomizer.

The resonator design of a Z-shaped standing wave cavity has been basically kept the same since the original development work presented in [81], while numerous smaller modifications have been made. The current design is summarized in [82], introducing an optional, second Fabry-Pérot etalon to decrease the spectral bandwidth down to 1 GHz. For specific applications, several variations of the design were created, *e.g.*, a version tuned by an optical grating in Littrow geometry [83, 84] as well as a bowtie ring resonator variant with an external wavelength seed to produce single-mode pulses with bandwidths below 100 MHz [84–86]. The reliability of the operation as well as the versatility made this laser system very popular up to the point that several major large scale research centers have adopted them for the use with resonant laser ionization ion sources, including ISOLDE/CERN (Geneva, CH), TRIUMF (Vancouver, CA), SPIRAL2/GANIL (Caen, FR), HRIBF/ORNL (Oak Ridge, US), and the University of Jyväskyla (FI).

Chapter 6

Initial evaluation of the ^{163}Ho ionization and separation process

The process following the chemical purification of the ^{163}Ho sample to the MMC detector loading, although performed in direct succession, can be split into several independent subtopics. First step is the sample preparation for use at RISIKO. After placement in the sample reservoir, the sample is evaporated and resonantly ionized. The ions are accelerated to form an ion beam which undergoes mass separation. Finally, the $A = 163$ component of this beam is directly implanted into the detectors. The efficiency defined as the final yield divided by the number of initial atoms or ions inserted, is crucial for all subprocesses, . Similarly the isolation of ^{163}Ho from all other sample components needs to be quantified and the introduction of any other contaminants prevented. Finally, the reliability with which these parameters can be fulfilled is of similar importance, as for the large numbers of MMC detectors needed, the rejection rate has to be kept as low as possible.

6.1 Sample preparation

Before a certain number of ^{163}Ho atoms can be introduced into the reservoir of the RISIKO ion source, they have to undergo careful preparation. Primarily, the samples have to be transfered into solid state on a carrier substrate. This is necessary, because liquid samples can not be properly positioned in the reservoir and would distribute due to wetting and capillary forces. With typical samples sizes below the µg range, *i.e.*, 10^{15} atoms or less, handling is more comfortable if deposited on a carrier substrate. In addition, the choice of substrate material strongly influences the chemical behavior of the sample at the high atomizer operation temperatures. The optimum substrate material induces a continuous release of sample material and serves as reducing agent to provide a steady supply of atomic vapor to be ionized by resonant laser light. Finally, the preparation process must reproducibly produce samples with a quantifiable amount of atoms with next to no losses.

The samples used in this work are either ^{163}Ho from the batch produced at the ILL

high flux reactor, or stable ^{165}Ho for all optimization and evaluation measurements. The ^{163}Ho was transferred to deionized water after the chromatographical separation with a concentration of $3 \cdot 10^{13}$ atoms/µl. Stable Ho was prepared in a similar way as described in sec. 3.4: 18.3(5) mg of $Ho(NO_3)_3 \cdot 5\ H_2O$ were weighed and dissolved in 25 ml of deionized water [71]. From this initial batch, a dilution was prepared by pipetting 2.5 ml and adding 22.5 ml of water as well as a further 1:9 dilution from the diluted solution. In this way, three well quantified base solutions were prepared with ^{165}Ho concentrations of 10^{13}, 10^{14} and 10^{15} atoms/µl, within relative uncertainties of 5 % [71].

Titanium was chosen as substrate material based on previous experiments with resonant laser ionization of lanthanides [79, 87]. Although not studied in detail, the process from sample to elementary vapor is assumed to obey the following scheme: After a 10 µl drop of one of the solutions is pipetted onto the Ti substrate, it is heated up in air to about 100 °C for 10 minutes to evaporate the solvent. According to Balboul [88] and Wendlandt *et al.* [89] the residue is again $Ho(NO_3)_3 \cdot 5\ H_2O$ at temperatures below 120 °C, $Ho(NO_3)_3 \cdot 4\ H_2O$ at 120 °C, or $Ho(NO_3)_3 \cdot 3\ H_2O$ at 140 °C. After introduction into the sample reservoir and by slowly increasing temperatures, the compound further evaporates water and the nitrate group undergoes decomposition in several steps until at temperatures above 560 °C Ho_2O_3 remains [88]. The latter is thermally very stable and has a high melting point of 2415 °C. Nevertheless, in combination with the Ti substrate, the equilibrium of the redox reaction

$$2\,Ho_2O_3 + 3\,Ti \rightleftharpoons 4\,Ho + 3\,TiO_2 \tag{6.1}$$

leads to a partial reduction to Ho. Close to and above its melting point of 1474 °C [90], the evaporation rate strongly increases, allowing Ho vapor to escape. Conversely, the higher melting points of the other components (Ti: 1668 °C, TiO_2: 1840 °C) incur lower evaporation rates, overall leading to a shift of the equilibrium of the redox reaction to the right. In turn, this induces the reduction of further Ho to balance the evaporation losses.

The dimensions of the Ti substrate were 6 mm × 6 mm × 12.5 µm, based on the mechanical requirements to be large enough to carry a drop of 10 µl and thick enough for folding without breaking, while using as little material as possible. After evaporation to dryness, the substrate is folded two or three times to fit into the sample reservoir and to increase the contact surface of Ho_2O_3 and Ti.

To verify the reliability of the preparation, the ^{165}Ho content of all solutions and samples needs to be analyzed. Two methods are directly available at the institute of nuclear chemistry in Mainz for this purpose: inductively coupled plasma mass spectrometry (ICP-MS [91]) and instrumental neutron activation analysis (INAA [92]). ICP-MS generally uses liquid samples that are injected with a certain flow rate and

ionized in a plasma torch. The ions are then mass separated in a quadrupole mass filter and counted by a secondary electron multiplier or similar detector. The system is calibrated using standard solutions with known concentrations and thus allows an absolute concentration measurement. Although element identification is possible by the analysis of the isotope composition, ICP-MS offers no inherent element selectivity and has its limits at low concentration with considerably strong isobaric contaminations. In contrast, INAA is based on γ-radiation emitted in the decay of radioactive isotopes: Sample material of either solid or liquid form is irradiated by thermal neutrons in a nuclear reactor core. If the product of the neutron capture reaction

$$ {}^{A}_{Z}X + \mathrm{n} \rightarrow {}^{A+1}_{Z}X \tag{6.2} $$

is radioactive, the emitted characteristic γ-radiation can be detected afterwards to identify and quantify contents of the sample. Although a coarse approximation of the sample size can be calculated on the basis of the neutron flux, capture cross-section, γ branching ratio and detection efficiency, much more precise values are obtained by calibration with samples of known size. The downside of INAA is its limitation to isotopes that are activated to radioactive species. Furthermore, the detection threshold is governed by the capture cross section and the half-life of the product.

In this work, samples of 10^{14} to 10^{16} atoms ^{165}Ho were irradiated for 6 hours in the carousel irradiation position of the research reactor TRIGA Mainz with a thermal neutron flux of $0.7 \cdot 10^{12}\,\mathrm{cm^{-2}\,s^{-1}}$. With a neutron capture cross section of 58 b for the reaction

$$ {}^{165}\mathrm{Ho} + \mathrm{n} \rightarrow {}^{166}\mathrm{Ho} \tag{6.3} $$

the expected produced amount after irradiation was $8.7 \cdot 10^{8}$ atoms ^{166}Ho for 10^{14} atoms ^{165}Ho. The half-life of 26.8 h and the relative intensity of 6.6 % for the strongest γ line at 80.6 keV lead to an activity of 39 Bq in this case[1]. The measured activities were about 60 % larger, which had two possible causes. On one hand, the actual neutron flux depends on the amount and positioning of neutron absorbers in the reactor core and can vary for each irradiation. On the other hand, the neutron capture cross section of ^{165}Ho exhibits a dense set of resonances from 4 eV to 1200 eV incident neutron energy. Although the fraction of neutrons in this range is small, the strengths of the resonances lead to a significant contribution to the production rate.

Two γ detectors were used with different parameters. For the intercomparison between samples on Ti foil a standard detector with a calibrated detection efficiency of 1.9 % at 80 keV was used. For quantification measurements, in which a reference sample from the solutions was irradiated as well, this configurations showed strong deviations between the different sample types. As a consequence, a second detector

[1] Nuclear data taken from National Nuclear Data Center, Brookhaven National Laboratory `http://www.nndc.bnl.gov/`

Table 6.1: Results of the quantitative analysis of the prepared ^{165}Ho samples by INAA and ICP-MS [71]. For more details, see text.

Nominal sample size	10^{14}	10^{15}	10^{16}
Base solution content in 10 µl	$1.09(5)\cdot10^{14}$	$1.14(5)\cdot10^{15}$	$1.24(5)\cdot10^{16}$
Transfer efficiency to substrate		103(5) %	
Relative standard deviation	8 %	5 %	4 %

was used with higher energy resolution and a larger sample distance to eliminate sample geometry dependencies. The drawback of this arrangement was a much lower detection efficiency of 0.22 % [71]. Absolute quantification of the three base solutions was carried out by the group of Prof. Reich using ICP-MS. Table 6.1 summarizes the results of the INAA and ICP-MS analysis, highlighting the good reproducibility of the sample preparation. The absolute sample sizes could not be quantified precisely as the detection efficiency was strongly dependent on the sample state, *i.e.*, liquid or solid. However, no indication of losses in the transfer and drying were visible and the calibration of the pipettes used could be confirmed to be within 2 %. Thus, a sample size of 10 µl of the base solution concentration was assumed with a relative uncertainty of 10 %.

6.2 Ionization efficiency

The next step in the process is the evaporation of sample material from the reservoir, ionization in the atomizer as well as extraction of an ion beam. The obvious goal is to transfer all of the desired sample, *i.e.*, ^{163}Ho for the implantation into microcalorimeters or ^{165}Ho during the commissioning phase, into the ion beam. At the same time, the ionization of all other contaminants in the sample, the reservoir or the atomizer should be minimized. With resonant laser ionization, atoms of a single element can be specifically addressed and ionized with high probability, while the ionization rate for atoms of other elements is mostly unaffected and independent of wavelength or power of the used lasers. These advantages of resonant laser ionization are the most distinct when applied to the lanthanide elements. Their chemical behavior allows a reduction when combined with a substrate like Ti as explained in the previous section and the necessary laser wavelengths are typically in the visible to near-UV range, which simplifies the generation by pulsed dye or Ti:sapphire lasers. This combination enables a high ionization efficiency with an unsurpassed elemental selectivity. Other ion source techniques that offer high ionization efficiencies like surface ionization are either non-selective towards different elements or the selectivity is only dependent on the difference in ionization potentials. Therefore, the ionization efficiency for differnt

lanthanide elements would be very similar and the selection of a single element would not be possible.

The application of resonant excitation of lanthanides at on-line isotope separator facilities was already reported in 1992 by Alkhazov *et al.* for the ionization of radioactive ytterbium at the IRIS separator facility at Gatchina, Russia [93]. The same group reported a year earlier ionization efficiencies as high as 35 % for stable ytterbium and presumably a few percent for holmium [94] achieved at the same type of ion source operated. The operated in off-line conditions using a three-step excitation scheme driven by pulsed, high repetition rate, high power dye lasers. The selectivity or enhancement defined as the ratio of the ion signal with resonant ionization to the signal with blocked lasers was as high as 300. Using the mass separator RISIKO and Ti:sapphire lasers, similar values could be demonstrated for ytterbium (10 %, 150 [79]). In the case of holmium even higher ionization efficiencies of 22 % and 29 % in two single measurements could be achieved [87]. The same laser system as used in these measurements was also installed at the ion source test facility ISTF-2 at the Oak Ridge National Laboratory. In a one-off experiment, an outstanding ionization efficiency of 40 % was achieved with a sample size of 10^{17} atoms ^{165}Ho [95]. These measurements were the starting point for the studies in this work, with the task of determining an ionization efficiency that can be reliably reproduced and quantifying the selectivity, which was not studied before. The results are reported in complete detail in [76] as well as the bachelor thesis of K. Chrysalidis [70].

The excitation scheme used identically in the successful experiments at RISIKO and

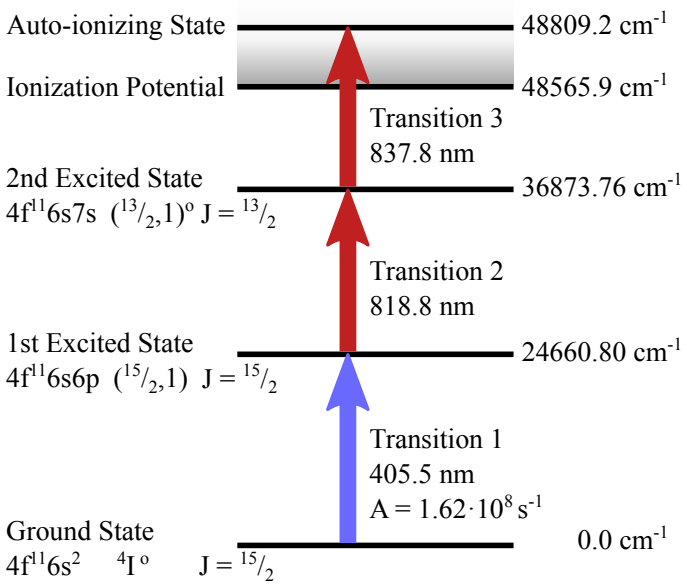

Figure 6.1: Excitation scheme for holmium used in this work and previous experiments [87, 95]. Figure taken from [76].

ISTF-2 was developed by T. Gottwald in Mainz [87]. As shown in fig. 6.1, it comprises three resonant excitation steps towards an auto-ionizing state. The first transition was driven by the second harmonic of a Ti:sapphire laser, whereas the other two transitions were excited by fundamental wavelengths, thus having more power available. With all three fundamental wavelengths being close to each other (811 nm, 819 nm, 838 nm), all resonators were equipped with the same mirror set („*Larissa Type III: 800-880 nm*“) and could be temporally synchronized without the use of Pockel's cells but instead by small changes of the longitudinal focus position of the pump beam. Pumped with 15.5 W power at a repetition rate of 10 kHz and a wavelength of 532 nm, the resonators emitted between 2.8 and 3.2 W power in the fundamental wavelength. Up to 300 mW power was available after second harmonic generation for the first transition. All three beams were focused to and overlapped in the atomizer. All relevant parameters of the lasers, output power, wavelength, beam position and temporal synchronization, were very stable and required only minuscule realignments over the course of several days.

For the evaluation of the excitation scheme a sample of 10^{16} atoms ^{165}Ho was used and the sample reservoir was kept at a rather low temperature. In this way a stable atom flux could be generated for hours. Spectra of the resonances and the dependency of the ion signal on the laser power were recorded for all three excitation steps as shown in fig. 6.2. The first transition could be well saturated leading to a strongly broadened resonance. The second transition could also be saturated thanks to the larger available power, whereas in the third transitions even at maximum available laser power a linear dependence of the signal was observed. The spectral shapes of the transitions were either Gaussian or, in cases with significant power broadening, a modified Gaussian. Curve fitting was performed to describe the saturation behavior in dependence of the input power P_{in} according to

$$I(P_{\mathrm{in}}) = C_1 \frac{1}{1 + P_{\mathrm{sat}}/P_{\mathrm{in}}} + C_2 P_{\mathrm{in}} + C_3, \tag{6.4}$$

with the saturation power P_{sat} and free parameters C_1 to C_3. Eq. (6.4) was also used in combination with a Gaussian to describe the saturated profiles by

$$I(\nu) = C_1 \frac{1 + S^{-1}}{1 + S^{-1} \exp\left(\frac{(\nu - \nu_{\mathrm{center}})^2}{2\sigma^2}\right)} + C_2, \tag{6.5}$$

with the saturation strength S. The curves reproduce the data quite well and the values for S are in agreement with the ratio of input laser power to the saturation level determined from the curves in the panels on the right in fig. 6.2. The extracted linewidths are between 25 and 32 GHz when excited with the maximum available power (tab. 6.2). In the first transition this is mostly caused by power broadening as can be seen by the much narrower shape at 0.2 mW laser power. The most narrow

Table 6.2: Results of the analysis of spectral profiles and saturation curves of the three transitions used. The given linewidth were measured at maximum output powers P_{max}. Adapted from [76].

Transition	ν_{exp} (cm^{-1})	ν_{lit} [96] (cm^{-1})	P_{sat} (mW)	P_{max} (mW)	*FWHM* (GHz)
1	$24660.822(4)_{stat}(20)_{sys}$	24660.80(5)	1.0(1)	267	31.8(6)
2	$12212.934(6)_{stat}(20)_{sys}$	12212.96(5)	1070(140)	2600	31.2(6)
3	$11935.052(7)_{stat}(20)_{sys}$	-	-	2600	25.2(6)

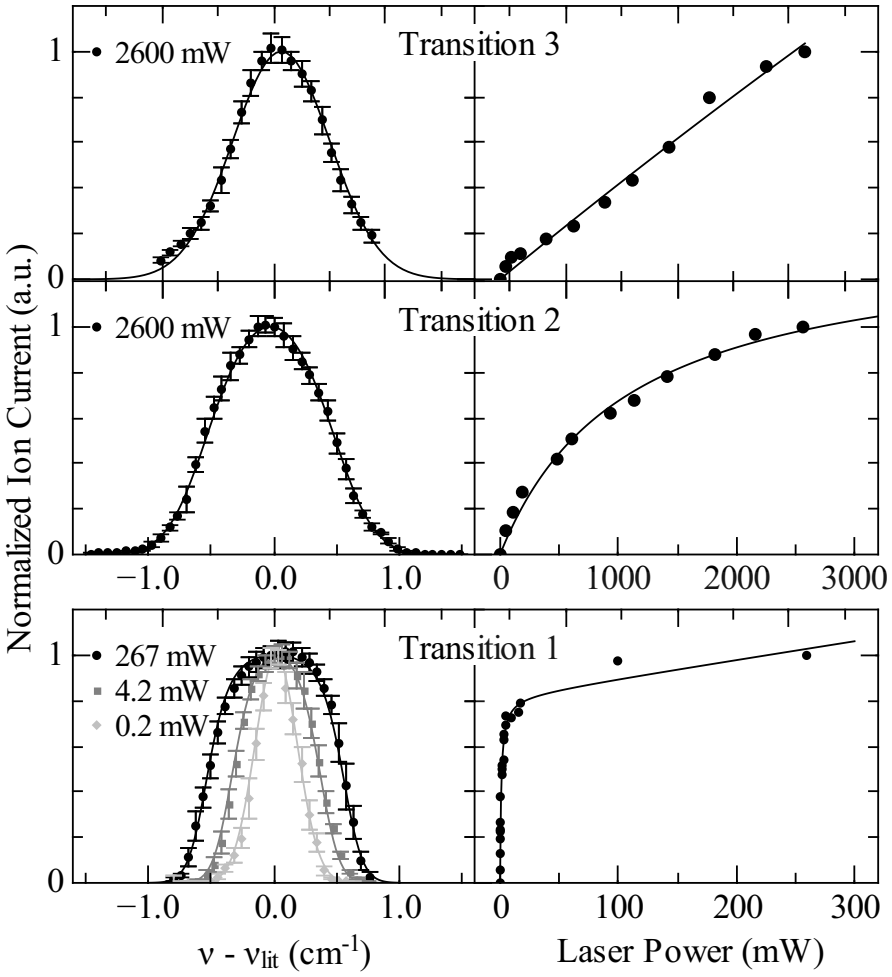

Figure 6.2: Resonances and saturation curves of the three transitions of the excitation scheme. Results from curve fitting are presented in table 6.2. Figure taken from [76].

Table 6.3: Operational parameters of RISIKO used for the determination of the ionization efficiency of holmium.

Parameter	Value
Atomizer heating current	270 A
Acceleration voltage	30000 V
Extraction electrode	18000 V
Einzel lens potential	11700 V
Deflection horizontal	250 V
Deflection vertical	150 V
Separator slit width	2 mm

linewidth measured was 6.0(1) GHz, matching the spectral width of the Ti:sapphire laser after second harmonic generation. Although the measured linewidth is similar for the other two transitions, there the effect from power broadening is much weaker. A possible reason for the larger inherent width is an unresolved hyperfine structure in the second excited state at 36873 cm^{-1}. As such, it would increase the observed linewidth in transitions 2 and 3 but would not affect the first transition. Because of the identical nuclear spin $I = {}^{7}/_{2}$ of ^{165}Ho as well as ^{163}Ho, no strong deviation is to be expected in the spectral shapes of the transitions, which was confirmed by recording the same spectra with a ^{163}Ho sample.

To determine the ionization efficiency, twelve individual runs were carried out with varying sample sizes of 10^{14}, 10^{15} or 10^{16} atoms. Between the different runs,

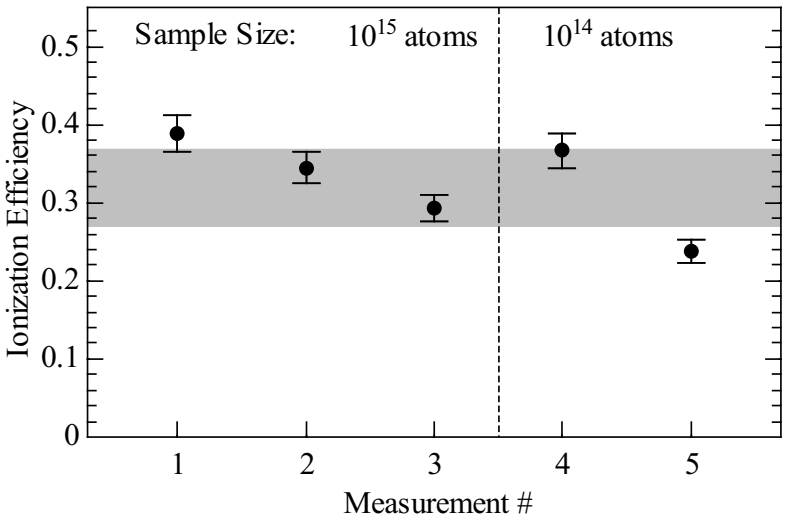

Figure 6.3: Overview of the measured ionization efficiencies for holmium. Out of the individual measurements a mean value of 32 % with a standard deviation of 5 % was determined as indicated by the grey band. Figure taken from [76].

several parameters were optimized, like the voltages of the ion optics, the position of the sample in the reservoir and the atomizer temperature. The best parameter set is listed in table 6.3. The last five of the twelve measurements were carried out with these parameters and analyzed to determine the ionization efficiency. The measured values with a mean of 32(5) % are shown in fig. 6.3. The uncertainties shown for each measurement only account for the sample size quantification and the ion current measurement. Further variations like the precise sample position or the conditioning of atomizer and sample reservoir could not be quantified, but certainly affect the achievable ionization efficiency. A detailed analysis of each run further reveals a pattern which all of these measurements follow. Figure 6.4 shows the reservoir heating current, the acquired ion current and the accumulated ionization efficiency over the course of measurement #2. Corresponding to the set heating current, four phases can be defined: (I) warm up, (II) initial sample release, (III) main measurement and (IV) bake-out. The sample reservoir is too cold in the first phase to start the evaporation driven reduction of Ho. This process initiates at a certain heating current, defining the start of the second phase. With further increasing the heating current, the evaporation rate increases leading to higher detected ion currents. The temperature is raised until a defined ion current of 10 nA is reached. Following that is the main phase of the measurement during which the heating current is only increased to counteract the slow decrease in ion signal from (local) sample depletion. As can be seen in the lowermost panel of fig. 6.4, the majority of ions is detected during this phase. The last phase covers the time after the maximum temperature level is reached, when the ion current decreases and the rest of the sample is slowly baked out. Although the rate of increasing the heating current as well as the maximum ion current is chosen by the operator, it is quite remarkable that for all five measurements in fig. 6.3, the transition to phase II occurs at a heating level of 50 to 55 A [70]. Such a reproducibility was not observed at RISIKO before and can only be attributed to the careful preparation of the samples and the ion source. Further insight was gained by studying temperature distribution simulations [72]. These were generated by heat flow calculations using computation fluid dynamics methods in Autodesk CFD[2]. Pyrometrically measured temperatures of various parts of the ion source at several heating currents served as calibration. These data indicate that at a heating current of 55 A the reservoir temperature at the sample location reaches 1500(30) °C as depicted in fig. 6.5. A comparison with the melting point of holmium of 1474 °C confirms the concept of an evaporation driven reaction. Similarly, even at maximum reservoir heating current, the temperature at the coldest point, the combined mounting point between reservoir and atomizer, is only 1420 °C. Here, holmium atoms can condensate and either remain there or at least have a long retention time before they evaporate again. This is most likely the reason for the slow

[2]Autodesk Inc., `http://www.autodesk.com/products/cfd/`

decay of the ion current in the last phase of the measurements.

6.3 Mass separation

The generated ion beam must be separated by mass of the charged particles to isolate ^{163}Ho and eliminate contaminations of *e.g.* ^{166m}Ho. At RISIKO this is carried out by sending the ion beam through the homogeneous magnetic field of a 60° sector field magnet. As outlined in sec. 5.2, the magnet is designed to bend the beam on a radius $\rho = 0.75$ m and focus a parallel incoming ion beam to a plane crossing the beam trajectory at 1043 mm behind the exit of the magnet yoke. At this position, the displacement between two ion beams of different mass is the largest in comparison to the beam diameter. The displacement can theoretically be calculated by the relative mass difference $\Delta m/m$ multiplied by the dispersion

$$D_{\mathrm{m}} = \frac{\rho}{2}(1 - \cos\phi + \frac{f_x}{\rho}\sin\phi), \tag{6.6}$$

with the deflection radius ρ, deflection angle ϕ and the focal position f_x [80]. In the mass region of ^{163}Ho, the displacement of two ion beams in RISIKO with $\rho = 0.75$ m,

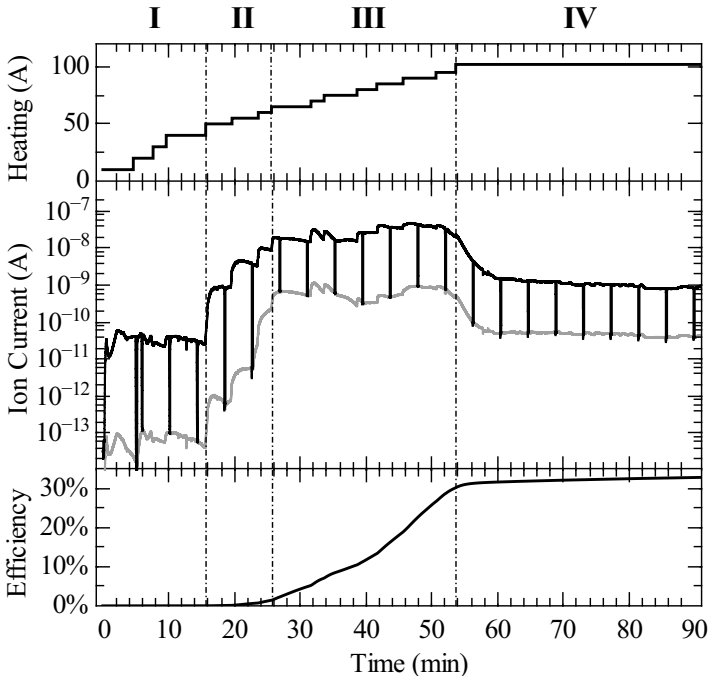

Figure 6.4: Resistive heating current, measured ion current and accumulated efficiency over the course of a measurement with a sample of 10^{15} atoms ^{165}Ho. The gray curve represents the background from surface ionization, detected by blocking the ionization lasers in regular intervals. For more details, see text. Figure adopted from [76].

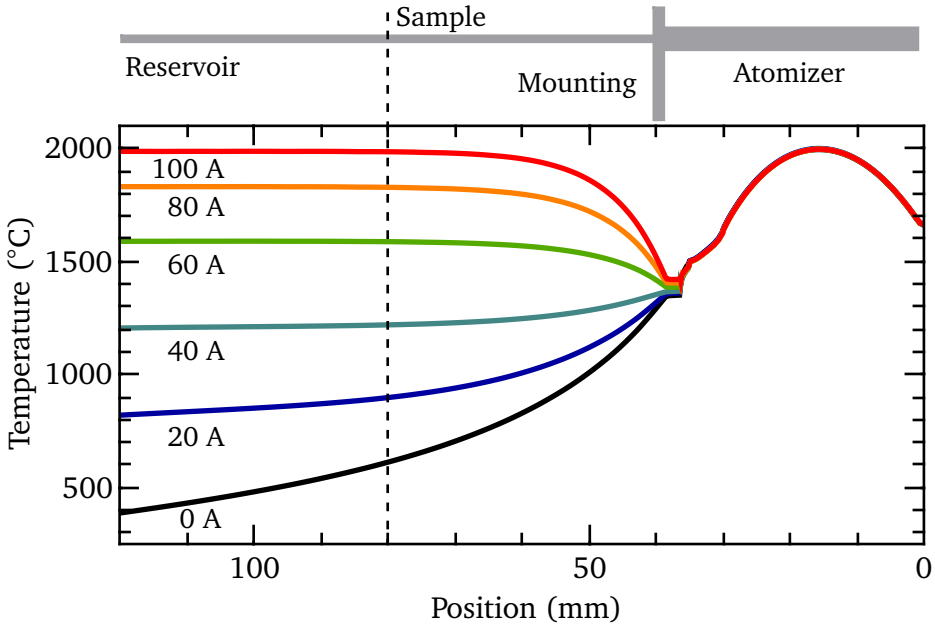

Figure 6.5: Simulated temperature distributions of the atomizer and sample reservoir. The curves were simulated for an atomizer heating current of 270 A and reservoir heating currents from 0 A to 100 A as labelled. The dashed line marks the sample position.

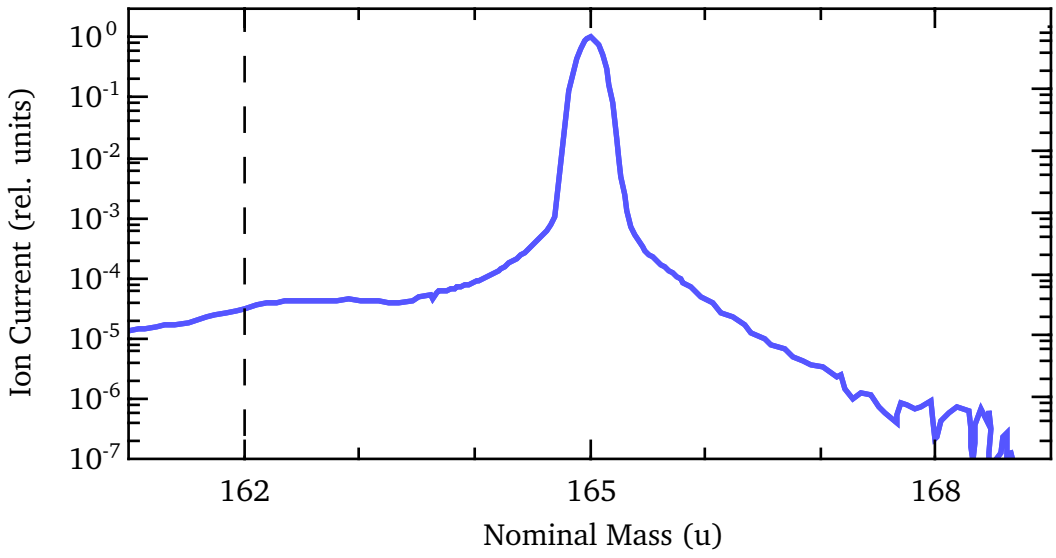

Figure 6.6: Transmission peak of $^{165}Ho^{+}$ recorded at RISIKO. The dashed line marks the position at $\Delta m = -3$ with a relative transmission of $3 \cdot 10^{-5}$, which represents the suppression of ^{166m}Ho while implanting ^{163}Ho ions.

$\phi = 60°$ and $f_x = 1.04\,\mathrm{m}$ equals to $3.9\,\mathrm{mm/u} \cdot \Delta m$. From a given horizontal beam diameter w_x, the obtainable mass resolving power can be calculated as

$$R_\mathrm{m} = \frac{D_\mathrm{m}}{w_\mathrm{x}}. \tag{6.7}$$

In the experiment, the resolving power can also be obtained from the width w_m (in units of mass) of a single transmission peak for ions of mass m in the mass spectrum:

$$R_\mathrm{m} = \frac{m}{w_\mathrm{m}}. \tag{6.8}$$

At RISIKO, values of R_m of 500 to 700 are regularly achieved. By decreasing the width of the separator slit to limit w_x, even larger values up to 1000 can be reached at the trade-off of a lower transmission. However, since w_x and w_m are measured as the full width at half maximum, the resolving power R_m has little significance regarding the suppression of neighboring masses. In the far wings of the profile, the Gaussian part is insignificant and background processes connected with wider profiles dominate the measured ion current. Figure 6.6 shows a transmission peak of $^{165}\mathrm{Ho}^+$ ions recorded with RISIKO. The center is nearly Gaussian with a width of $w_m = 0.32\,\mathrm{u}$ yielding a mass resolving power of $R_m = 515$. For $|\Delta m| \geq 0.5\,\mathrm{u}$ a much wider, asymmetric structure becomes visible, determining the suppression of neighboring masses. The most important point for this work is the relative transmission at $\Delta m = -3$ of $3 \cdot 10^{-5}$. This value represents the relative transmission of $^{166\mathrm{m}}\mathrm{Ho}^+$ ions while the separator is set to transmit $^{163}\mathrm{Ho}^+$ ions. Combined with the relative concentration of 0.02 % in the sample, the ion beam after the separation supposedly has a $^{166\mathrm{m}}$Ho content of $5 \cdot 10^{-9}$. This is already very close to the target value of $1 \cdot 10^{-9}$.

To estimate further stable contaminations of the beam, mass spectra were recorded using the available ^{163}Ho sample. Figure 6.7 shows a comparison of two spectra recorded with either the ionization laser irradiating the atomizer or with blocked lasers, respectively. The ratio ^{163}Ho:^{165}Ho is 3.4, in discrepancy with the expected ratio of 2.0. This is caused by a strong downwards trend of the ion current during the measurement. The ^{165}Ho current was affected to a larger degree than ^{163}Ho by this because the spectrum was recorded scanning from light to heavy masses. Nevertheless, an estimation of contaminants is possible, albeit at an unknown level of precision. Because the signal on mass 166 u was mostly unaffected by the laser light, it was not only caused by $^{166\mathrm{m}}$Ho ions but predominantly by surface ions of the neighboring element erbium. Including this, the main contamination species are ions with mass 162 u, 164 u and 166 u, as well as 168 u and 170 u (not shown in graph), detected with relative strengths of 0.6:0.3:1:0.9:0.2. These relative levels roughly match the signature of the erbium target material as determined independently by ICP-MS measurements. Its occurence is in agreement with a typical suppression factor of 500 [33] for erbium

in the liquid chromatography: Out of the original 30 mg Er, about 60 µg, equivalent to $2 \cdot 10^{17}$ atoms, are still contained in the sample of $2 \cdot 10^{18}$ ^{163}Ho atoms. Because no other signals in this mass range are detected, any further stable contaminations is assumed to be negligible. Based on these findings, the expected final beam constitution for the ion implantation is listed in table 6.4. It was calculated from the transmission function shown in fig. 6.6 and the isotope constitutions of the ^{163}Ho sample as well as the erbium target material after irradiation.

6.4 Ion implantation

Ion implantation is a technique regularly used to permanently fixate dopant ions within a target near the surface. With typical ion kinetic energies of 10 to 100 keV the implantation depth is 0.1 to 100 nm, mostly depending on the atomic masses of projectile and target. The stability of implanted ions is highlighted by applications in which nitrogen ions are implanted with 20 to 40 keV into steel or titanium alloys to drastically reduce friction wear of and increase lifetimes of tools [97]. For the ECHo experiment, ion implantation is a promising method of directly transferring already ionized ^{163}Ho into the gold absorbers without the need for additional processing steps. Furthermore, implanted holmium atoms are located in the gold crystal lattice below the surface instead of a single layer close to each other on top of the surface, which

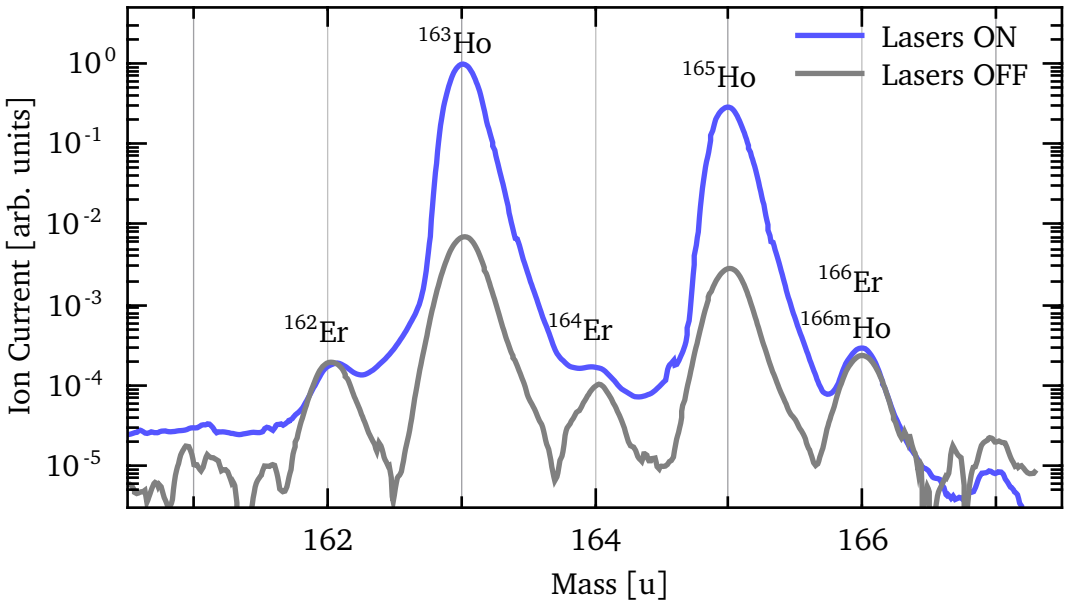

Figure 6.7: Mass spectra of the ^{163}Ho sample recorded with resonant laser ionization (blue) and surface ionization only (gray). The peaks on even mass numbers are residuals from the erbium target material.

Table 6.4: Assumed constitution of the ion beam during ^{163}Ho implantation. A selectivity of 100 is assumed for the resonant laser ionization.

Isotope	rel. concentration
^{163}Ho	99.998 %
^{165}Ho	$2 \cdot 10^{-5}$
^{166m}Ho	$5 \cdot 10^{-9}$
^{162}Er	$7 \cdot 10^{-9}$
^{164}Er	$3 \cdot 10^{-9}$
^{166}Er	$9 \cdot 10^{-9}$
^{168}Er	$4 \cdot 10^{-9}$
^{170}Er	$0.7 \cdot 10^{-9}$

would be the case with deposition techniques. Handling of the loaded detectors similarly would not require special precautions for weakly bound material, too. Instead, even cleaning with solvent to remove dust particles would be possible.

For given parameters of incoming ions the implantation process can be simulated by the software SRIM[3]. It calculates the energy loss of the projectile by recoiling or ionizing atoms in the target. From Monte-Carlo simulations of many ions, depth profiles and lateral distributions of the implanted atoms can be generated. The calculation for the implantation of ^{163}Ho$^+$ ions at 30 keV energy into gold results in a mean depth of 5.6 nm with a straggling range of 3.3 nm as shown in fig. 6.8. With a foreseen activity of 1 Bq per detector pixel ($= 2 \cdot 10^{11}$ atoms per 170 µm × 170 µm detector pixel), the

[3] SRIM - The Stopping and Range of Ions in Matter, version srim-2013.00 [98] `http://www.srim.org/`

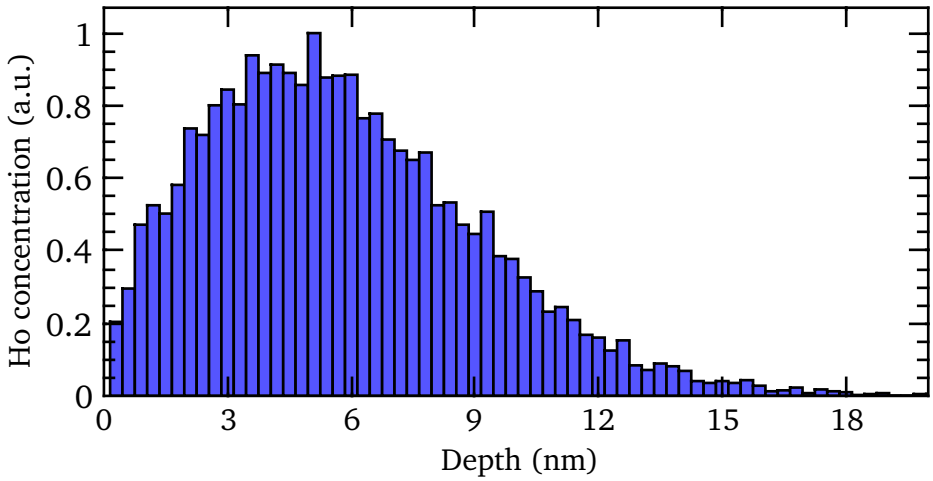

Figure 6.8: Depth profile for the implantation of ^{163}Ho ions into gold at 30 keV incident energy calculated with SRIM [98].

concentration of holmium to gold atoms is 0.7 % in the relevant depth up to 10 nm. This fulfills the goal of observing individual ^{163}Ho atoms (or, more precisely, excited ^{163}Dy atoms after an electron capture) interacting with the Au lattice but not with each other. Based on these findings, ion implantation seems to be the ideal method for the ECHo detector loading.

To perform the ion implantation at RISIKO, several aspects had to be evaluated. First of all, the ion beam spot size has to be quite small to implant a significant fraction into the microscopic detector pixels. Based on the design of the development detectors with four $170 \times 170\,\mu m^2$ pixels in a 2×2 layout with $20\,\mu m$ gaps, an FWHM beam waist of 0.5 to 1 mm would offer the best compromise between geometrical efficiency (42 % to 14 %) and implantation density variation (ratio between highest and lowest of 4.2 to 1.4). Smaller beam sizes would require scanning across the detector area to ensure a uniform density of implanted Ho ions. In addition to the beam size, the beam current and a stable beam position are of interest. The beam current along with a known beam waist defines the necessary implantation time to accumulate a given number of ions, as long as the beam is stationary and centered on the detector. Ideally, all three parameters should be monitored in parallel to the implantation process, but since the necessary detection elements are not all present at RISIKO, some limitations have to be accepted.

The beam waist was determined by implanting ^{165}Ho ions into a 99.9 % purity aluminum foil exposed in a dedicated Faraday Cup unit. The latter was mounted in the same location where the detector implantation is foreseen, 500 mm downstream of the separation slit. This allowed a direct measurement of the implanted beam current with an estimate of 10^{15} implanted ions. The foil was then irradiated for six hours in the research reactor TRIGA Mainz. After irradiation and a short cool down period, the neutron activation product of aluminum (^{28}Al, $T_{1/2} = 2.2\,\text{min}$) has decayed to stable ^{28}Si and the only remaining radioactivity is the produced ^{166}Ho ($T_{1/2} = 26.8\,\text{h}$). The visualization of the distribution is carried out by radiographic imaging using plates of photostimulable X-ray storage phosphors [99]. X-rays released in radioactive decays create electron-hole pairs in the plate that are stable and locally captured. After imaging, light from a focused HeNe laser locally excites electrons, leading to the recombination of electrons and holes under emission of visible light, which is amplified and detected. The advantage to X-ray imaging films is the gain in spatial resolution from controlled readout by the laser light. The FWHM beam waist determined by this method was 3.5(1) mm in the horizontal and 1.9(1) mm in the vertical direction [72]. The strong ellipticity is caused by the astigmatic focusing of the separator magnet, although it was expected only to a smaller extent based on the difference in focal positions of $f_x = 1043\,\text{mm}$ and $f_y = 1147\,\text{mm}$ compared to to the measurement position at $x_{\text{meas}} = 1550\,\text{mm}$. A possible explanation is a weaker vertical focusing as calculated

by the magnet manufacturer. In agreement with the work of Wollnik [80], the given focal positions are calculated for a magnet with the given tilt of the entry and exit plane and Rogowski chamfered pole shoes. The latter are used in combination with field shunts to generate a defined field gradient outside of the pole shoes in a way that the effective field boundary matches the pole dimensions. In this way an effective field can be considered that is of constant strength inside of the pole shoes and zero outside for calculating the horizontal deflection and focusing. But Wollnik further shows that a more precise inclusion of the field shunts introduces an additional vertical defocusing [80]. The defocussing strength depends on the precise geometry of the coils and the fringing field shunts, but can be approximated to change the vertical focal position from $f_y = 1147\,\text{mm}$ to $f_y = 1270\,\text{mm}$ in the case of the RISIKO separator magnet if this effect was not included in the magnet design. In that case, the vertical focal position would be closer to the measurement position, incurring a strong ellipticity as seen in the radiographic imaging. For the ion implantation, this ellipticity is of minor concern, but the large beam waist in general reduces the geometrical efficiency to only 1.5 %.

For the ion beam implantation into the ECHo microcalorimeters, a large diameter Faraday cup to mount a detector was constructed [72]. The design, pictured in fig. 6.9,

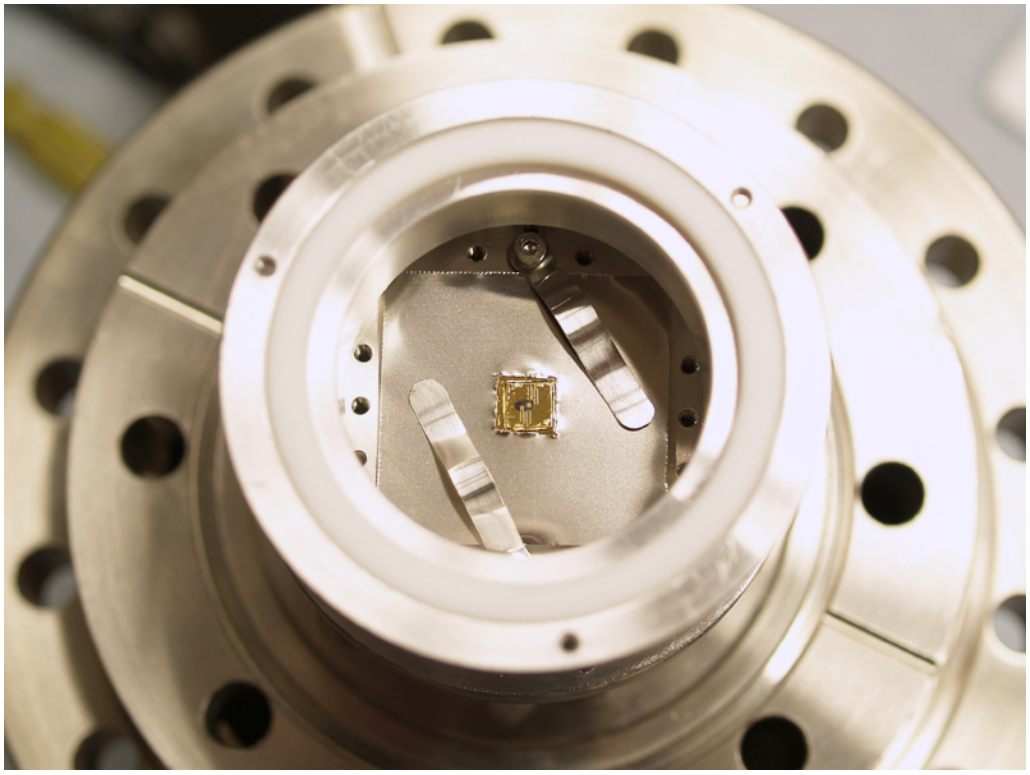

Figure 6.9: Photograph of a microcalorimeter mounted in the Faraday cup after implantation of ^{165}Ho ions. The center dark area of the gold covered detector is due to ion implantation. Photograph adopted from [72].

includes an interchangeable front plate to adapt to different uses as well as an internal electrode to suppress secondary electron created from the impinging ions. The front plate used for implantation features a 2 mm diameter aperture, large enough to transmit the relevant part of the ion beam but still offering the possibility to center the ion beam with steering electrodes by locating the position of maximum transmission. To be able to measure a beam current while implanting ions, as well as to only implant ions into the detector absorbers and not their surroundings, they are pre-treated by the group of L. Gastaldo at the University of Heidelberg. The detectors are completely covered with a thick ($\approx 1\,\mu$m) layer of photoresist. The area of the absorbers to be implanted is then exposed to UV light, making the photoresist layer soluble only in these locations. It is then removed, opening the absorber to incoming ions, whereas the rest of the substrate is protected by the photoresist layer. Finally, a 100 nm layer of gold is added to the detector to inhibit local charge buildup and enable the possibility to readout the ion current across the full surface. In fig. 6.9 a gold covered detector is mounted in the Faraday cup. To prevent damage to the gold and photoresist layer, it is additionally protected by a steel foil passe-partout.

6.5 Summary

The evaluation measurements have shown that ion implantation of ^{163}Ho into microcalorimeter detectors is generally possible with RISIKO, albeit with minor restrictions. The expected efficiency of the complete process, *i.e.*, transfer from the liquid sample to the detectors, is only 0.5 %. Although the sample preparation induces no losses and the ionization can be performed with an excellent efficiency of 32(5) %, the implantation efficiency is hampered by the large beam diameter.

The ^{166m}Ho level of 0.02 % in the sample would be reduced by the mass separation to a level of $5 \cdot 10^{-9}$. This is sufficient for the first stage of the ECHo experiment but does not completely match the requirements of being below $1 \cdot 10^{-9}$. Besides these restrictions, the complete implantation process was successfully demonstrated with stable ^{165}Ho samples implanted into detectors with equivalent amounts of 1, 10 and 100 Bq for heat capacity measurements. Including sample introduction, evacuation and changes of the calorimeters, the complete process could be completed in a few hours.

Chapter 7

Improvements to the implantation process

Based on the experience gained by the evaluation measurements, several parts of RISIKO were upgraded, and in addition, possible improvements were identified. First and foremost, the implantation region was moved further downstream to include a new lens system for beam refocusing. Furthermore a number of, modifications of the ion source were implemented to improve the temperature distribution. To reach the desired suppression of ^{166m}Ho during implantation, an additional temporal separation is suggested as described below.

The following sections present these upgrades in detail in the order of appearance along the RISIKO beam path.

7.1 Ion source temperature optimization

The analysis of the ion current development over a complete ionization and collection sequence of a sample (see fig. 6.4) revealed the melting point of holmium as most critical temperature above which the reduction and evaporation process starts and below which atoms condensate with long retention times. At the same time the selectivity of the resonant ionization, *i.e.*, the ratio of the resonant ion current to the non-resonant ion current, is limited by the level of non-resonant ionization. The dominant disturbing process is surface ionization at the hot atomizer walls. The Saha-Langmuir equation [100] describes the temperature dependence of the equilibrium ratio of ions n_i and neutrals n_0 as

$$\frac{n_i}{n_0} = \exp\left(\frac{\phi - IP}{kT}\right), \tag{7.1}$$

with the work function ϕ of the atomizer material and the ionization potential *IP* of the element of interest. A more complete description leading to the actual ionization efficiency of a surface ionization ion source is given by Kirchner *et al.* in [101]. His findings are based on the assumption of a quasi neutral, non-thermalized plasma in the atomizer created by neutral and ionized species of the atomizer material, contaminations therein, the sample material if present, and glow-electrons emitted by the

hot surface. This plasma leads to a strong amplification of the ionization efficiency, depending on the degree of thermalization of the created ions. For typical ISOL type surface ion sources, this factor can reach values of typically 150, and up to 700 if operated with a high pressure of neutral particles [101]. A decrease of surface ionization of Ho itself as well as contaminant species is therefore possible by either changing the atomizer material to decrease the work function, by modifying operational parameters that influence the thermalization of the plasma, or by decreasing the ion source temperature. A change of material is difficult, because the direct ohmic heating requires a conductive material with structural and chemical stability at high temperatures. Considering pure metals with a melting point above 2500 °C (Mo, Ta, Os, Re, W), tantalum already offers the lowest work function. Similarly, the parameters dictating the amplification factor are either difficult to access or a change would also influence the resonant laser ionization. Thus, a decrease in temperature is the most effective way to lower surface ionization rates. Due to the exponential effect, changing from 2200 °C to 2000 °C already reduces the ionization efficiency for holmium ($IP = 6.0\,\mathrm{eV}$) in a tantalum cavity ($\phi = 4.2\,\mathrm{eV}$) by a factor of two. Optimizing the temperature distribution of an atomizer cavity for resonant laser ionization therefore implies a decrease of the maximum temperature while keeping the lowest temperatures above the melting point of the element of interest. The ultimate goal would be a completely uniform temperature distribution along the atomizer.

The CFD model of the ion source region of RISIKO developed to simulate the temperature distribution [72] is able to reproduce pyrometrically measured temperatures quite well. With a more extensive calibration to a larger set of temperatures measured at different positions and heating currents [74] to establish suitable values for contact resistances, the model is now able to predict the temperature distributions also for changes in the geometry or materials. The main heat loss channels of the atomizer and the sample reservoir are thermal conduction at the mounting points to the water cooled vacuum vessel and black-body radiation. Both channels were analyzed: On one hand, a decrease of the cross-sections of the mounting pieces at front and back of the atomizer to reduce heat transport only induced a rather small temperature gains of about 30 K at the respective positions. On the other hand, a reduction of the emissivity and surface area of hot parts caused more drastic increases in temperature. The combined mounting point of atomizer and reservoir was the coldest parts of the assembly, causing long retention times of holmium atoms as seen in the measurement of the ionization efficiency (phase IV in fig. 6.4). The removal of non-structural material (see fig. 7.1) increased the temperature of the back of the atomizer by about 200 K when heated at the identical current. Another increase could be gained by covering the graphite fastening nut with tantalum foil. Although the nut was not directly replaced with a Ta nut to prevent welding to the atomizer, covering with a Ta foil similarly de-

creases the emissivity from $\epsilon_C = 0.9$ to $\epsilon_{Ta} = 0.13 - 0.35$, increasing the temperature at this point by an additional 40 to 90 K, depending on the actual heating current. The measured total temperature change of 240 to 280 K as listed in table 7.1 also roughly matches the prediction of the simulation of 300 K [74]. However, not only the temperature of the parts that were modified, but also along the complete atomizer cavity increased. From the simulation, an increase of the maximum temperature by 120 K was expected. Thus, to actually achieve a decline of surface ionization as well as of holmium condensation, the atomizer has to be operated at a lower heating current. A value between 250 and 260 A seemed the most promising to ensure a minimum temperature of 1500 °C for all parts while still keeping the maximum temperature lower than originally.

These modifications motivated a new series of measurements to again determine the optimum parameter set and to quantify possible improvements in ionization efficiency and selectivity. The procedure was the same as in chapter 6.2 using sample sizes of $3.7 \cdot 10^{14}$ atoms of ^{165}Ho. In these runs, a very high reproducibility as well as a significantly increased ionization efficiency of 40(6) % was achieved as shown in fig. 7.2 for a heating current of 255 A. This effectively prevented condensation or at least reduced retention times substantially, causing an increased ionization efficiency as well as a faster exhaustion of the sample in the final measurement phase. Whereas

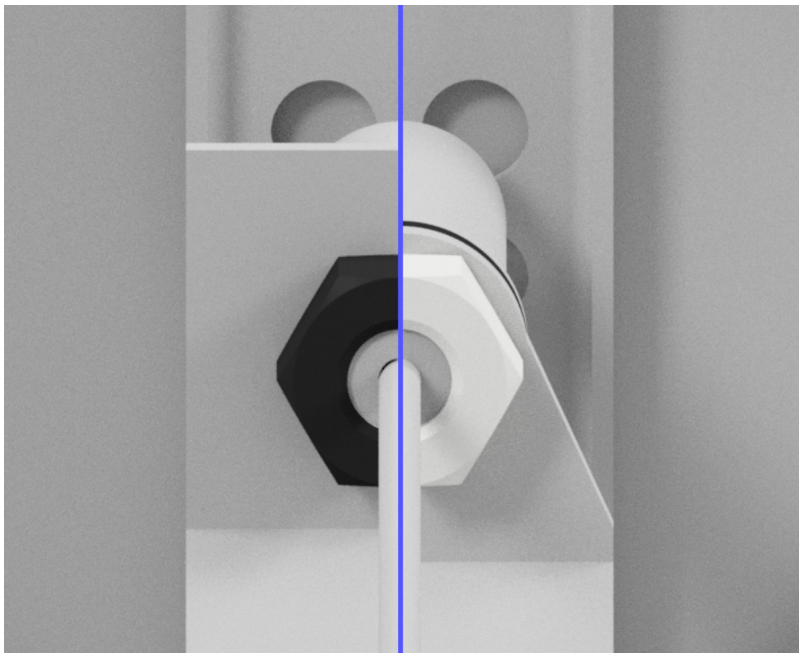

Figure 7.1: Side by side comparison of the atomizer mounting structure and fastening nut designs. The previous design (left) had a graphite nut, while the improved design uses a tantalum cover for the nut as well as less non-structural material to reduce losses from black-body radiation.

Table 7.1: Measured temperatures of the atomizer close to the combined mounting point at different heating currents in the previous design and with the improvements installed to reduce heat loss from radiation. Values adopted from [74].

Design	Temperature (°C)		
	$I_{\mathrm{heat}} = 200\,\mathrm{A}$	$I_{\mathrm{heat}} = 250\,\mathrm{A}$	$I_{\mathrm{heat}} = 300\,\mathrm{A}$
Original mounting piece	1010	1280	1490
Removed non-structural part	1190	1470	1680
Ta covered graphite nut	1280	1530	1720

previously the measured ion current decreased from 1 nA to 100 pA over the course of several hours (see phase IV in fig. 6.4), the current now settles at a level of 10 pA within an hour after the end of the main measurement phase as shown in fig. 7.3. The maximum temperature in the atomizer is expected to be 50 to 100 °C lower than before, which is reflected in favorably lower ion currents from surface ionization. For most of the main measurement phase, the selectivity was larger than 100 in these runs, up to a maximum value of 250. The newly introduced modifications of the atomizer mounting thus clearly improved the sample release behavior and lead to an optimized ionization efficiency 1.3 times as large as before. The successful prediction of the temperature gains by the simulation also motivates to digitally investigate further changes in the ion source assembly to move towards a more uniform temperature distribution.

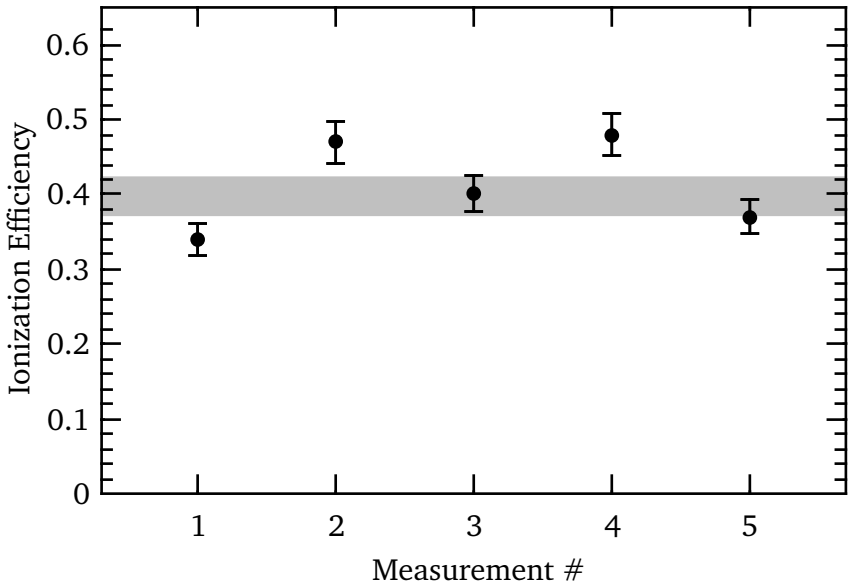

Figure 7.2: Overview of the measured ionization efficiencies for holmium with improved atomizer mounting. A mean value of 40 % with a standard deviation of 3 % was determined as indicated by the grey band.

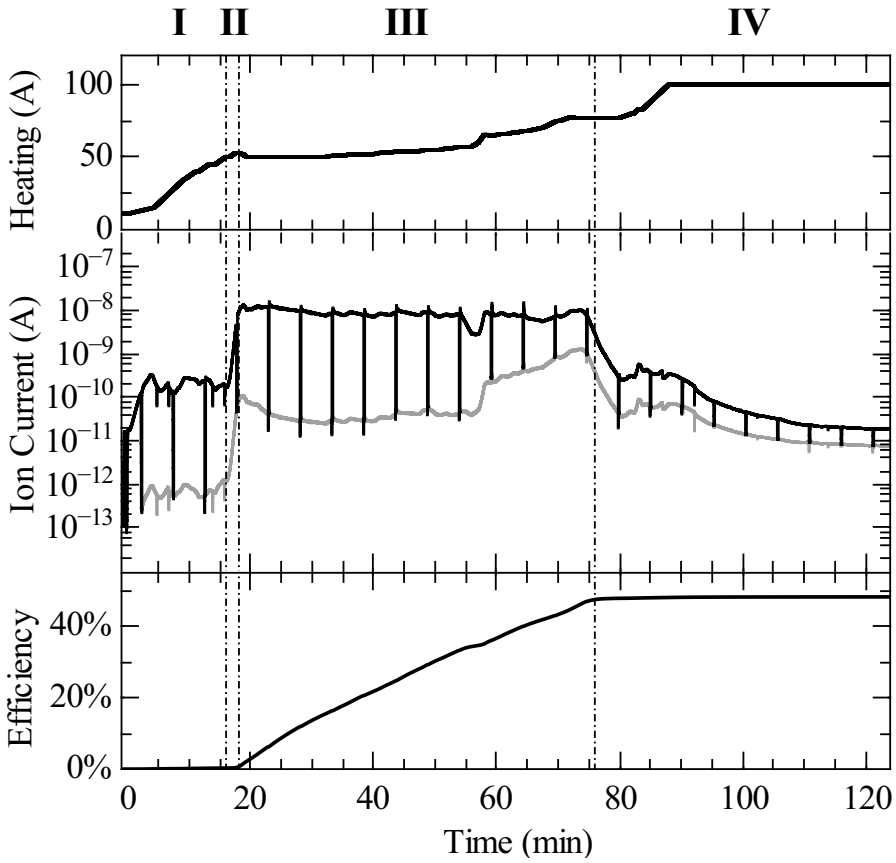

Figure 7.3: Resistive heating current, measured ion current and accumulated ionization efficiency over the course of a measurement with a sample of $3.7 \cdot 10^{14}$ atoms ^{165}Ho. The gray curve represents the background from surface ionization.

7.2 Reduction of beam contamination

One of the key requirements for the ECHo detector implantation is the separation of ^{166m}Ho down to a relative concentration of 10^{-9} in respect to ^{163}Ho. The evaluation of the process at RISIKO showed that this prerequisite is not yet completely fulfilled with a lowest achievable concentration of $5 \cdot 10^{-9}$ as determined in sec. 6.3. This limitation is caused by the far wings of the ion beam transmission profile behind the separator magnet. As shown in fig. 6.6, the center part of the beam has an almost Gaussian shape with a sufficiently small width for an insignificant transmission if the magnetic field is adjusted for ions of a 3 u lighter mass. However, an underlying structure with by far more slowly declining wings increases the relative transmission at $\Delta m = -3$ to a level of $3 \cdot 10^{-5}$, whereas a value of $\leq 5 \cdot 10^{-6}$ would be needed for the current sample composition. With Er in higher enrichment grades, especially a higher ratio of ^{162}Er:^{164}Er,^{163}Ho samples produced in future irradiations are expected to have correspondingly lower ^{166m}Ho concentrations. Nevertheless, the mass separation should be improved to ensure the required depletion of ^{166m}Ho with the existing sample, too.

The dominant processes leading to peak shapes as in fig. 6.6, are described by Menat as elastic and inelastic scattering processes [102, 103]. These induce deflection of ions from the principal trajectory with detection at differing magnetic field strengths. In [102] Menat presents a quantitative description of the scattered ion current for simple slit type mass separators, separately addressing three regions: between ion source and magnet, within the magnetic field, and between the magnet exit and the collection slit in the focal plane. This description is extended to double-focusing

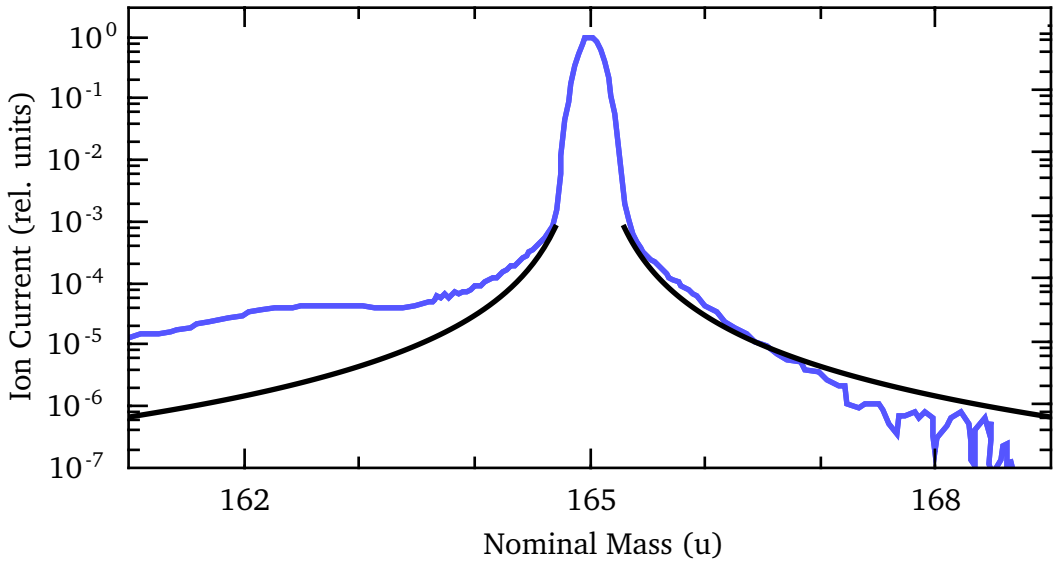

Figure 7.4: Transmission peak of $^{165}Ho^+$ recorded at RISIKO (blue) and calculated distribution of elastically scattered ions from eq. (7.2) (black).

mass separators in [103]. The elastic scattered ion current i relative to the nominal current I in dependence on the apparent mass difference Δm is

$$i/I = n_{\mathrm{r}}\sigma_0 \frac{\pi r_{\mathrm{D}}^2}{\rho} T(\phi)\left(\frac{m}{\Delta m}\right)^n \tag{7.2}$$

for a fringe-field focusing device, with the atom density of the residual gas n_{r}, the scattering cross section σ_0 and the setup specific dimensions of the Faraday cup aperture radius r_{D}, sector field deflection angle ϕ and radius ρ. The configuration factor $T(\phi)$ is calculated by Menat to be 1.9 for a sector angle ϕ of 60°. The angle dependence factor n lies between 2.65 and 2.95, dependent on the ion mass, with heavy ions having a smaller n. Interpolation of the values given in [103] results in $n = 2.74$ and $\sigma_0 = 1.8 \cdot 10^{-18}\,\mathrm{cm}^2$ for the scattering of Ho ions in residual air. This allows the calculation of the expected scattered ion current in RISIKO with a typical pressure of $5 \cdot 10^{-7}$mbar as shown in fig. 7.4. For the heavy side of the peak the model predicts the ion current at the correct order of magnitude, although the theoretically predicted decline towards larger mass differences is not as strong as measured. This discrepancy is most likely due to the difference in geometry of RISIKO and the model in [103], where a double focusing sector magnet operated in a symmetric point-to-point imaging mode with the ion source in one focal point and the collector Faraday cup in the other focal plane is assumed. In contrast, at RISIKO the magnet is used in parallel-to-point imaging, using a parallel ion beam from a distant ion source. In addition, the ions are not collected in the focal plane but pass the separation slit ($w = 2\,\mathrm{mm}$) and are detected about 500 mm downstream in a Faraday cup with $r_D = 1\,\mathrm{mm}$. Thus, a reevaluation of the scattering integrals of [102] adapted to RISIKO would be required to precisely describe the scattered ion beam profile. In a simpler, more qualitative description the combination of the separator slit and the small Faraday cup serves as an angular filter, only allowing the detection of ions which cross the focal plane at small angles. This could already explain the steeper slope in fig. 7.4 at heavy masses, where larger scattering angles occur. Based on this, elastic scattering can be safely assumed as origin for the extended peak tails towards heavy masses. On the other hand, the scattering theory produces a symmetric distribution and thus cannot explain the much stronger contamination towards lighter ions a further source has to be found for this.

Menat further lists inelastic scattering processes, with charge exchange having the largest cross section [102]. In his calculations, both scattering partners are relevant in regards of beam contamination: neutralized ions from the beam and ionized particles of residual gas. However, the Faraday cup detection at RISIKO in insensitive to neutral particles, thus their contribution can be neglected at this point. In contrast, the ionized particles created by charge exchange can be critical if they are heavier than the ion of interest and if the charge exchange occurs in the extraction gap in front of the ion source. In this case, the ions are accelerated towards the separator magnet and

can be detected afterwards. The key parameter is the distance from the ion source: With increasing distance z to the source, the electric potential decreases as shown in fig. 7.5. Thus, ions created further away do not attain the complete nominal kinetic energy U_{nom} but rather a lower energy $U_{\mathrm{dec}}(z)$, coined by Menat as *chromatic* ions. These have correspondingly a lower magnetic rigidity:

$$\chi = \frac{mv}{q} = \frac{m}{q}\sqrt{\frac{2qU_{\mathrm{dec}}}{m}} = \sqrt{\frac{2mU_{\mathrm{dec}}}{q}}. \tag{7.3}$$

As particles of same χ follow the same deflection radius in a magnetic field [80], chromatic ions effectively behave like ions with energy U_{nom} and an apparent mass $m_{\mathrm{app}} = mU_{\mathrm{dec}}/U_{\mathrm{nom}}$. As an example, a $^{166\mathrm{m}}\mathrm{Ho}^{+}$ ion with a kinetic energy of 29458 eV would have the same trajectory in the separator magnet as ^{163}Ho ionized inside the atomizer. Using the curve shown in fig. 7.5, this can be translated to a starting position 2.9 mm in front of the atomizer. This scenario is entirely possible: With an ionization efficiency of 40 %, significant amounts of the material are bound to leave the atomizer in neutral form. In such a small distance to the atomizer orifice, the number density of holmium atoms is therefore non-negligible.

Adding to this matter, the application of resonant laser ionization opens another channel for a very similar contamination. The laser beams are sent in anti-collinearly which allows atoms all along the beam path to the separator magnet to interact with the laser light. This especially includes atoms of Ho in close proximity to the atomizer, again leading to an increased contamination on the lighter side in the mass spectrum. Compared to the charge exchange process, the strength of this contamination is even independent on the initial ion beam current, possibly making it the dominant source

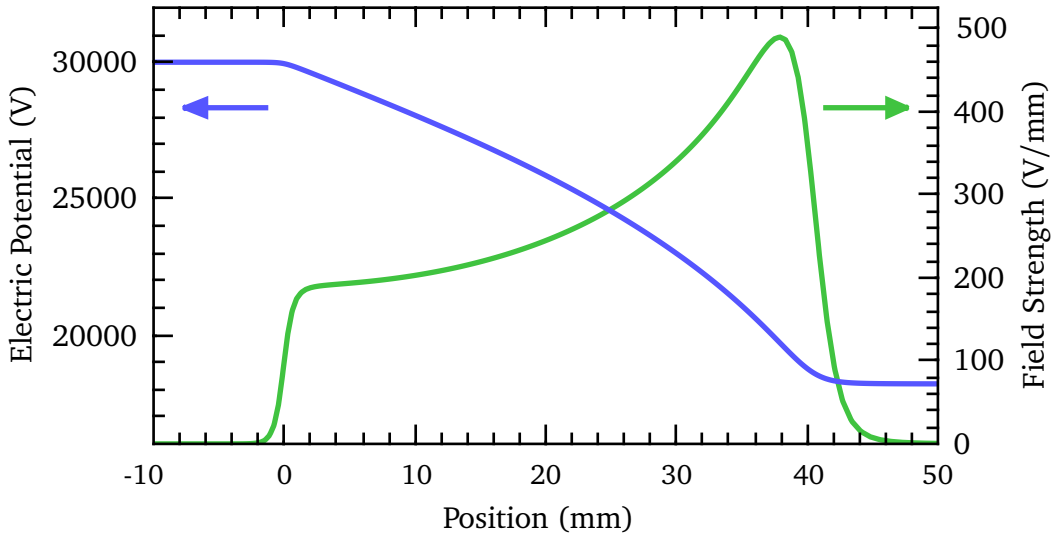

Figure 7.5: Calculated potential and field strength of the accelerating electric field in the gap between the atomizer and the extraction electrode at 40 mm.

of chromatic ions. An estimation of the relative strength compared to the initial ion beam cannot be given for none of these processes due to large uncertainties in the charge exchange cross section being partly resonant for same species interaction, or even unknown values like the ionization cross section of the resonant ionization and the density of Ho atoms in front of the atomizer.

A further study of the underlying effects can be done by exploiting the pulsed structure of ion bunches created by (resonant) laser ionization with pulsed lasers. A time-resolved detection allows the further assignment of properties beyond the magnetic rigidity to the ions. Such studies were performed by Richter with ytterbium ions in RISIKO [79]. The ionization scheme consisted of two transitions, whereas the first transition with a wavelength of 267.3 nm excited the atoms to an intermediate level and second transition with a wavelength of 736.7 nm lead to the ionization through an auto-ionizing state. The sample reservoir and atomizer were operated to create low intensity ion beams with currents below 10 fA, translating to average ion rates of about to 10^5 ions per second. This allowed a time resolved detection using a secondary electron multiplier combined with multichannel scaler. Figure 7.6 shows the recorded bunch shape accumulated over several laser shots. Above the time independent signal level from surface ionization in the atomizer, three structures can be differentiated: a

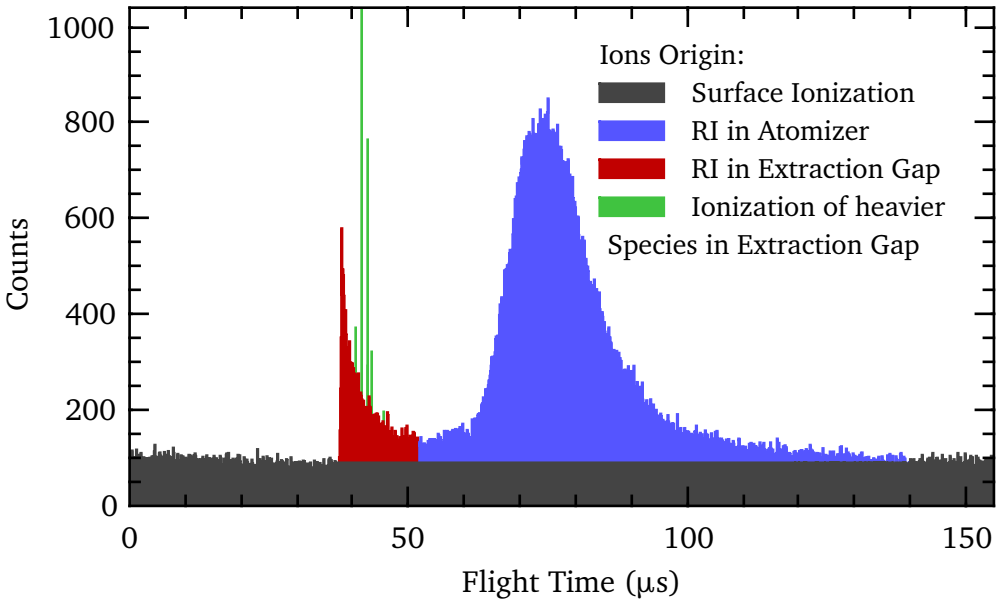

Figure 7.6: Temporal ion bunch shape of resonantly ionized ^{174}Yb. The zero point on the time axis marks the laser shot. Four contributions can be identified: constant, laser independent background from surface ionization (gray), resonant ionization in the atomizer (blue), resonant ionization in the extraction gap (red) and non-resonant laser ionization of heavier elements in the extraction gap (green). For details to the identification, see the text.

dominant peak from ionization of Yb in the atomizer, the smaller first structure originating from chromatic Yb ions created in the extraction gap and set of a sharp peaks of chromatic ions of larger mass. The individual identification is possible on the basis on the respective height and flight time. The kinetic energy of the chromatic Yb ions is only slightly smaller than $U_{\mathrm{nom}} = 30\,\mathrm{keV}$, as they are still detected at their nominal magnetic rigidity. However, due to being created inside the strong extraction field, they are immediately accelerated and therefore arrive the earliest at the detector. In contrast, ions created in the atomizer first have to move towards the exit to reach the extraction field, only guided by a weak electric field of about $0.1\,\mathrm{V/mm}$ caused by the potential drop of the heating current. Both structures are only present if both lasers are sent into the atomizer at the correct wavelength. On top of the chromatic ions, several very sharp peaks arise. These were not influenced by the second, infrared laser and also independent of the precise wavelength of the first, ultraviolet laser. This non-resonant behavior excludes them from being Yb ions, thus they necessarily are non-resonantly ionized other species. A more thorough investigation of all these structures across a large range of magnetic rigidities is shown in fig. 7.7 adapted from [79]. Here, chromatic ions are visible as diagonal structures diverging from the vertical lines of ions from the same species. Based on this, the sharp peaks can be identified as chromatic ions of heavier species. The detailed analysis revealed the detection of ions that were created up to 20 mm in front of the atomizer, having about 25.8 keV kinetic energy. Quite possibly, ions with even lower energy were generated as well, but were not detected due to experiencing a significantly stronger focusing effect from the einzel lens. In conclusion, the source for chromatic ions in RISIKO is most dominantly the laser ionization of atoms in the extraction gap. Charge exchange as a source for chromatic ions can be excluded on the basis of the bottom panel of fig. 7.7 containing no indication for chromatic ions that are not synchronized to the laser pulses. These would be observed as continuous asymmetric extensions of the vertical traces, especially of strongly surface ionized species like Ta ($m = 181\,\mathrm{u}$) or TaO ($m = 197\,\mathrm{u}$).

After identification of contaminations, in particular regarding the contamination of heavier species when collecting lighter ions, direct countermeasures can be prepared. Most promising is a pulsed operation of the ion optics in synchronization to the laser pulses to remove laser generated chromatic ions. One possibility would be a pulsed extraction similar to secondary ion mass spectrometers. For this, the extraction electrode would be kept at the same potential as the atomizer, *i.e.*, 30 kV, during the laser pulse. Afterwards it is pulsed to its nominal value. In this way, atoms ionized in the gap are accelerated to the full nominal energy of $U_{\mathrm{nom}} = 30\,\mathrm{keV}$. Another possibility is not to guarantee the complete acceleration of chromatic ions, but to remove the ions from the beam instead. As shown in fig. 7.6 chromatic ions arrive at the detector before the

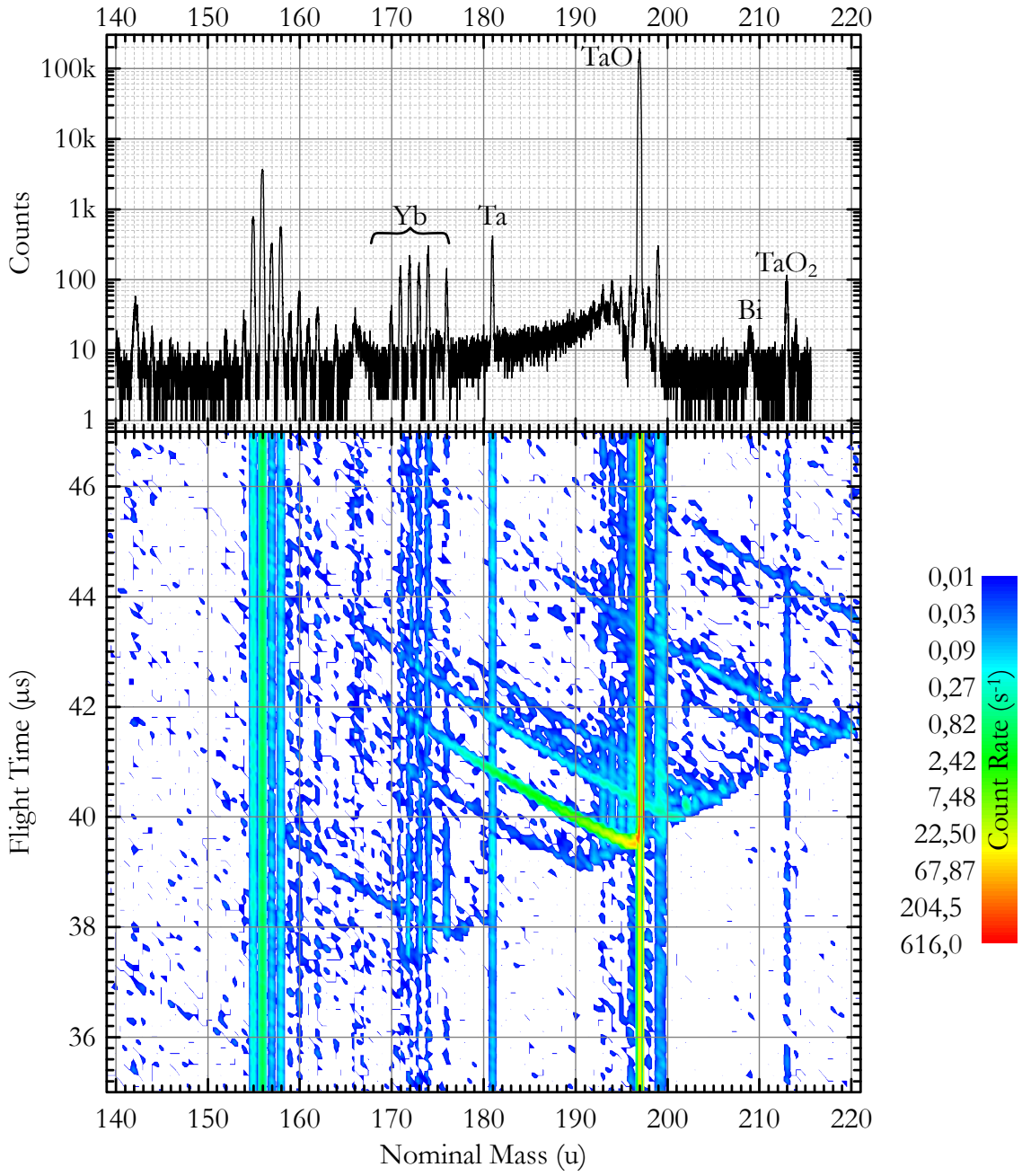

Figure 7.7: Top: Mass spectrum recorded in RISIKO with resonant laser ionization of ytterbium (^{168}Yb-^{176}Yb). Identified contamination peaks are labeled. Bottom: Color map of the bunch shapes recorded at different magnetic field settings, the displayed time range only contains ions originating from the extraction gap (compare fig. 7.6). The diagonal structures stem from the same species ions ionized at different positions in the extraction gap and thus have different kinetic energies. For more details, see text or [79]. Figure adopted from [79].

main ion bunch, therefore they could be selectively deflected off the beam axis with a pulsed deflection system. Such a system is easier to implement as the voltages to be switched with $< \mu s$ rise times would be on the order of just some 100 V instead of 10 to 15 kV as would be the case with a pulsed extraction. Concerning chromatic ions created by charge exchange, neither method is able to suppress these, as they would mostly be created when the main bunch is being accelerated through the gap and as such do not arrive at the detector at a significantly different time. Further investigations about their significance will be possible when the laser generated chromatic ions are removed.

7.3 Beam refocusing

With the high efficiency in sample preparation and ionization demonstrated in 6, the obvious bottle neck in the microcalorimeter implantation of ^{163}Ho for ECHo is the large beam spot at the implantation position in comparison to the microcalorimeter pixel size. The FWHM beam size at the implantation region as shown in fig. 7.8b was measured to be 3.5(1) mm (horizontal) × 1.9(1) mm (vertical). A reduction would be possible by performing the implantation directly behind the separator slit, where the beam is focused to a size of 1.2(1) mm × 2.0(1) mm. But in this case the installation of the Faraday cup or an exchange of the microcalorimeter would require opening the 600 mm main flange of the vacuum chamber due to a lack of other access possibilities. A clearly better solution is the installation of new dedicated ion optics to refocus the beam further downstream. In addition to the freedom of choice for the implantation position, a focusing system can be designed to have a magnification below 1, *i.e.*, producing a scaled down image of the separator slit focus. For this purpose the detection region vacuum chamber was replaced by an extended setup, separated from the previous parts by a gate valve as shown in fig. 7.9b. Detector changes between implantation runs therefore only require venting and re-pumping of the relatively small vacuum section of 20 l instead of a much larger 200 l vacuum chamber as originally.

The design requirements of the new optics included a simple one-parameter tuning of the focusing strength and the inclusion of a deflection system for beam positioning and scanning on the implantation target across a region of 15 mm × 15 mm. To fulfill these requirements, a combination of a two stage einzel lens and a subsequent deflection stage was chosen in the thesis of S. Junck [73]. The advantage of a two stage einzel lens is the operation with lower voltages to reduce the risk of sparking or discharges to protect sensitive detectors and connected electronics. In addition, in a decelerating-accelerating operation of the lens, the beam waist is not as strongly enlarged, lessening the effect of imperfect electric fields. Figure 7.10 depicts a section view of the final design including the potential along the beam axis. To simplify align-

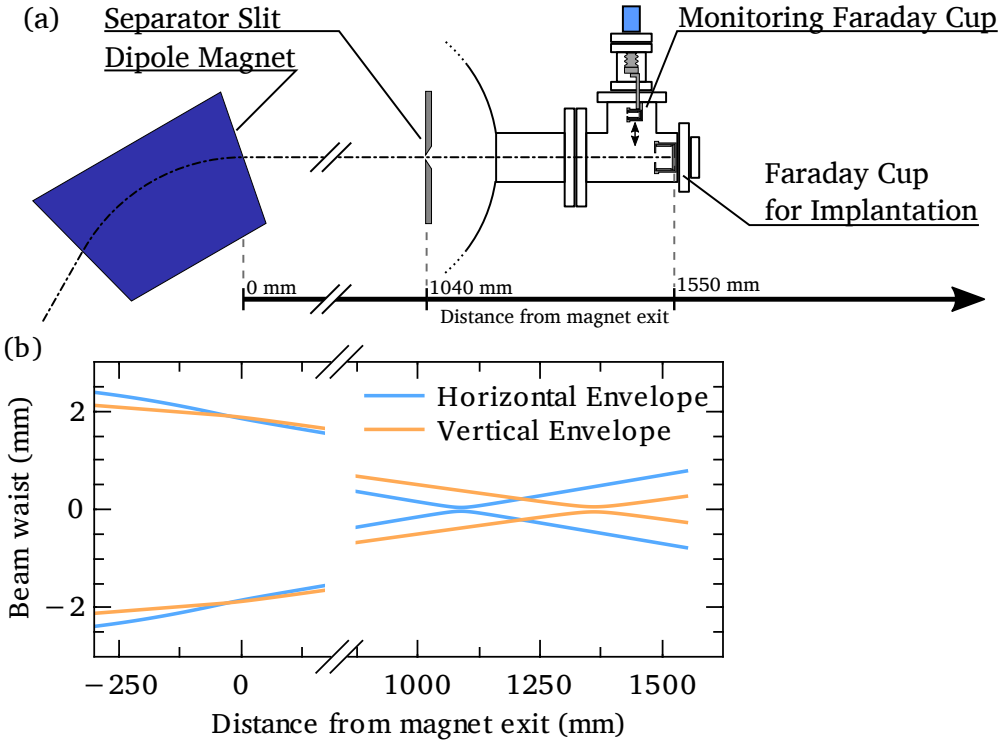

Figure 7.8: Schematic Layout (a) and calculated beam envelopes for a low emittance beam (b) for the RISIKO detection region in the original configuration.

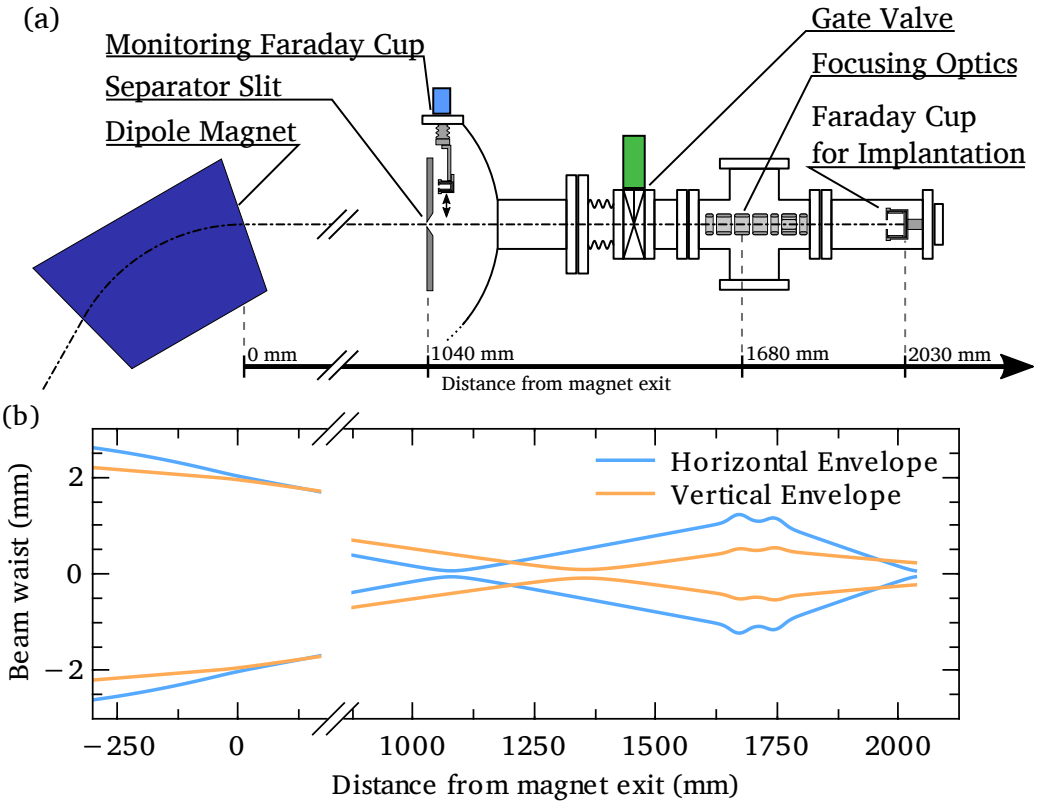

Figure 7.9: Schematic Layout (a) and calculated beam envelopes for a low emittance beam (b) for the upgraded RISIKO detection region including post-focussing optics.

ment, the system is manufactured as a set of ring electrodes and insulators stacked on top of each other and externally fastened by threaded rods as shown in fig. 7.11. The first five electrodes form the two stage einzel lens, with the second and fourth electrodes being connected to a HV power supply. Beam deflection is made possible by splitting the sixth electrode into four 90° sectors allowing the application of transversal electric fields. Mounted in the location shown in fig. 7.9, a focal length of $f = 230\,\mathrm{mm}$ is required to image the focused beam from the slit plane towards the implantation plane. With the given image and object distances, a magnification of 0.55 is expected. Using the matrix formalism for ion optics as described in [104] and [105], the required voltage for the two lens stages would be 15512 V resulting in a magnification of 0.53.

The design was implemented in SIMION to study ion trajectories, in particular to estimate the effect of spherical aberration. Based on the simulation results, paraxial beams originating from a point like focus in the separator slit plane are focused with a voltage of 14480(5) V on the implantation plane. The effect of spherical aberration can be seen in fig. 7.12: Starting from a point-like focus in the slit plane and near parallel beam, ions entering the lens system under a larger opening angle are focused at significantly lower voltages. Therefore, the voltage has to be chosen according to the actual beam opening angle in the experiment. Direct measurements of the beam opening angle have not been performed at RISIKO, but from beam profile measurements at the slit plane (FWHM $1.2 \times 2.0\,\mathrm{mm}^2$) and at the previous location of the implantation plane (FWHM $3.5 \times 1.9\,\mathrm{mm}^2$) an opening half angle of 0.16(4)° can be estimated. The increase in width from spherical aberration can be determined by simulating ion trajectories of ions starting from a point-like focus in the slit plane with a Gaussian distributed starting angle. In this way, the smallest obtainable FWHM beam

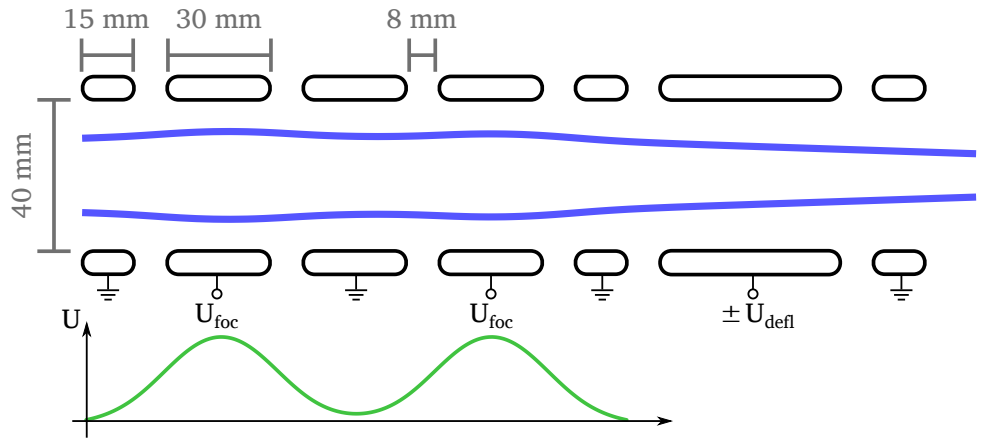

Figure 7.10: Cut view of the refocusing optics, consisting of a two stage einzel lens and a sectioned tube for beam deflection. Shown in blue are the beam envelopes (scaled by ×4 transversally) and in green the electric potential along the symmetry axis.

waist for ions with an origin on the beam axis was 0.012(3) mm at a focusing voltage of 14455(20) V. Ions starting 1 mm off-axis could be focused to 0.020(3) mm. However, when simulating trajectories with ions originating from an extended spot with a FWHM of 1.2 mm, the smallest focus had a waist of 0.50(3) mm with a focusing voltage of 14000(200) V. In conclusion, although the effect of spherical aberration of the refocusing lens system is detectable, it is negligible compared to the realistic beam diameters of RISIKO.

All of these calculations were performed on the basis of a beam focus at the separator slit. In reality, due to the astigmatic focusing of the separator magnet, this is only true for the horizontal direction. Vertically, the beam is focused further downstream in a region 100 mm to 250 mm behind the slit. This was not considered in the design of the lens system, because the regular operation is foreseen in combination with a quadrupole triplet lens in front of the magnet to correct the astigmatic imaging. This quadrupole triplet is already mounted and aligned in RISIKO but not in use because the required power supplies were not yet available. Table 7.2 summarizes the results from

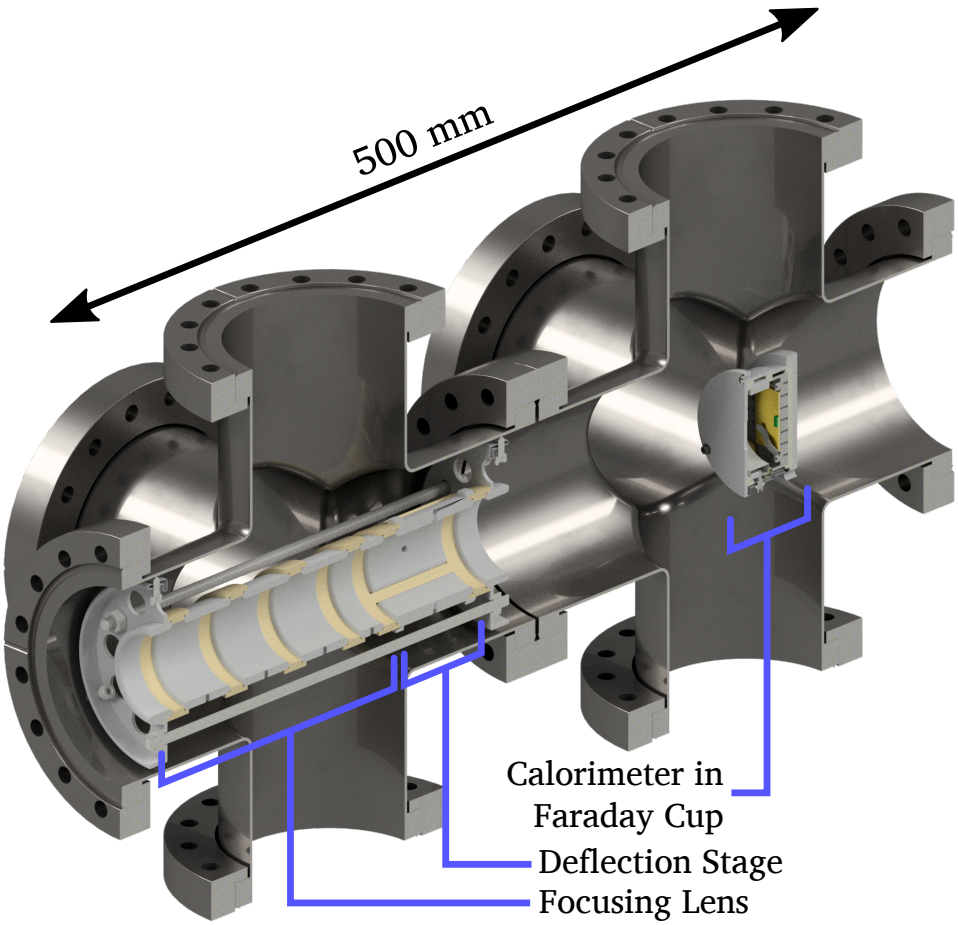

Figure 7.11: 3D model of the new refocusing optics and the implantation Faraday cup within the surrounding vacuum double cross chambers.

Table 7.2: Results from simulated ion trajectories in the new focussing optics using SIMION.

Initial Parameters at Separator Slit		Focusing Voltage	Beam waist at
Beam Waist	Opening half angle	U_{foc}	implantation plane
Point-like focus	0.16°	14455(20) V	0.012(3) mm
1.2 mm FWHM	0.16°	14000(200) V	0.54(2) mm
In case of astigmatic vertical focus 100 mm to 250 mm downstream:			
1.2 mm FWHM	0.16°	14000 V	1.1(1) mm

the simulation, including the effect of an astigmatic beam. Taking the measured beam profiles and including the astigmatic focusing, a beam waist of $0.54(2) \times 1.1(1)\,\mathrm{mm}^2$ is expected. This already is about eleven times smaller than without refocusing in the previous configuration.

The new focusing optics were successfully installed and commissioned in the thesis of S. Kormannshaus [75]. The new vacuum system proved to be leak tight and final pressures of $5 \cdot 10^{-7}$ mbar were reached. Alignment was done by using the axis defined by the opposing view port in the magnet chamber and the exit flange of the separator slit chamber as reference. In addition, the regular beam monitoring Faraday cup was moved as shown in fig. 7.9 and aligned to the same axis as well. As final check, the maximum applicable voltage was tested and up to the output limit of the power supply of 35 kV no sparking occured.

First operation with an ion beam was done with a beam of stable ^{165}Ho. By varying the field strength between the horizontal and vertical deflection plates, the beam was scanned across a 1 mm aperture of the beam monitoring Faraday cup. In this

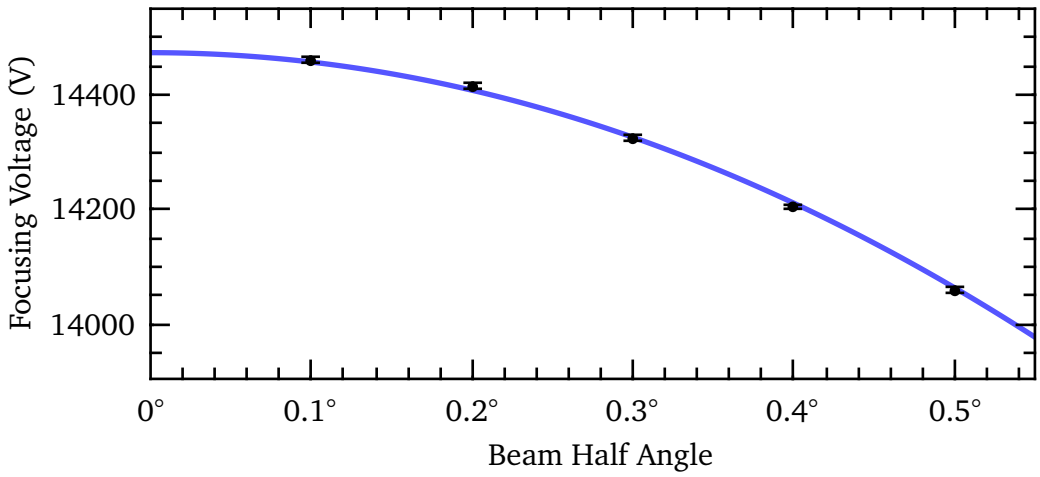

Figure 7.12: Voltages of the einzel lens to focus ions of a given beam opening half angle. The solid line is a parabola fit to the data.

way, a convolution of the beam shape with the rectangular transmission function was obtained. In combination with a calibration value of of 21.5 V/mm for the necessary plate voltages to achieve a certain deflection obtained from SIMION, the beam shapes can be deduced from the measured profiles. In the same manner using the deflection stage in the new focusing optics and a calibration value of 125 V/mm, the beam shapes at the implantation Faraday cups were obtained. When using an extraction voltage of 20 kV and an einzel lens voltage of 10 kV, the horizontal focus was in the slit plane. The beam size was measured to be 1.14(3) mm × 2.00(6) mm in good agreement with a previously determined value by other means. The voltage of the new focusing system was optimized by minimizing the beam waists. 14000 V proved to be the optimum value, producing a beam with 0.62(2) mm × 1.01(6) mm size. This completely confirms the expected values obtained from the SIMION simulations. The new optics therefore were able to increase the calculated overlap of the ion beam with the microcalorimeter absorbers nearly tenfold from 1.5 % to 14.5 % for a 2×2 detector layout with edge lengths of 170 µm.

7.4 Summary

The implemented upgrades to RISIKO drastically improved the efficiency from sample to implanted ions. The efficiency for the ionization could be increased from 32(5) % to 40(6) % with the reduction of atomizer heat dissipation. The implantation efficiency was strongly improved from 1.5 % to 14.5 % with the installation of a new set of ion optics. Overall, a twelve times gain to a total efficiency of 6 % was achieved. Furthermore, beam gating of the ion bunches by pulsed deflection is expected to reduce the ^{166m}Ho contaminations down to the goal of a relative concentration of $< 10^{-9}$. For the first ECHo phase, all requirements are met and the implantations can be performed as soon as the detector design is finalized and manufactured.

Part III

Conclusion

Within this work two important tasks for the starting phase of the ECHo experiment were addressed. In the first part the ^{163}Ho and ^{163}Dy atomic masses as well as the decay energy Q_{EC} were measured for the first time by Penning-trap mass spectrometry. In the second part the processes of ionization and implantation of ^{163}Ho into the ECHo microcalorimeter detectors was developed and characterized.

For the determination of the neutrino mass by analyzing the endpoint region of ^{163}Ho electron capture decay spectrum, the decay energy Q_{EC} is a key factor. However, published values for Q_{EC} from different groups are in strong disagreement. The majority of measurements report values around 2.555(16) keV [35], but more recent measurements point towards a significantly larger value of 2.80(8) keV [27]. All measurements have in common that the determination of Q_{EC} was made indirectly by analyzing the decay spectrum in comparison to atomic theories. In contrast, high-precision Penning-trap mass spectrometry allows a direct measurement of Q_{EC} from the mass difference of ^{163}Ho to ^{163}Dy. Within this work, preparatory work towards such a high-precision measurement was carried out at the TRIGA-TRAP Penning-trap mass spectrometer. ^{163}Ho^{16}O$^+$ or alternatively ^{163}Dy^{16}O$^+$ ions were created in a laser ablation ion source recently upgraded by the addition of a RFQ trapping structure. The ions were transported to the double Penning trap system in which their cyclotron frequency ν_c was measured using the time-of-flight ion cyclotron resonance technique (ToF-ICR). From the ratio of these frequencies to ν_c of $^{12}C_{15}^+$, whose mass is precisely known, the atomic masses of ^{163}Ho and ^{163}Dy were extracted. The obtained values $m(^{163}\text{Ho}) = 162.928\,738\,92(96)$ u and $m(^{163}\text{Dy}) = 162.928\,736\,47(87)$ u are both in agreement with literature data [35], whereas the uncertainties could be decreased by about a factor of two. This marks the two isotopes as the atoms with the most precisely measured masses within the lanthanide group. In a similar way, Q_{EC} was determined by directly comparing the respective ν_c to 2.5(7) keV. Although this value cannot solve the disagreement in the literature data because of the much larger uncertainty, it served as valuable check for systematic errors and as a benchmark of the achievable uncertainties with the ToF-ICR technique. Beyond the values obtained, this measurement campaign could confirm the suitability of the available ^{163}Ho sample as well as the ionization method for Penning-trap mass spectrometry. The improvements of the Mini-RFQ ion source in comparison to the previous simpler laser ablation ion source made it possible to perform the full measurements with only a fraction of the inserted $3 \cdot 10^{16}$ ^{163}Ho atoms. In addition, the recorded frequency ratios showed no detectable upward or downward trend, which could have been expected if the laser ablation process would lead towards an increasing cross-contamination of the two samples.

After verification of the suitability of the ^{163}Ho sample in this work, Q_{EC} was determined at the Penning-trap mass spectrometer SHIPTRAP with higher precision to

be $2.833(30)_{stat}(15)_{sys}$ keV by Eliseev *et al.* [38]. The lower uncertainty was achieved by employing the phase imaging ion cyclotron resonance technique (PI-ICR [37]). Here, the ions transversal position in the trap during ejection is imaged onto a spatially resolving detector. This allows the determination of the phase of the ions circular motion and therefore enables a more precise measurement of ν_c involving similar storage times and necessary number of ions as the time-of-flight ion cyclotron resonance technique applied at TRIGA-TRAP. A first step towards an implementation of PI-ICR at TRIGA-TRAP was taken in the diploma thesis of van de Laar [106], in which such a spatially resolving detector was installed and characterized. Currently the drift path between the measurement trap and the detector is overhauled to support the higher acceleration voltages required by PI-ICR. Furthermore, in parallel development, the detection of the image currents induced by stored ions is implemented. This will allow the measurement of ν_c using a single stored ion by the Fourier-transform ion cyclotron resonance technique (FT-ICR [107]). With the possibility of mass measurements at very high precision using PI-ICR or on single ions using FT-ICR, the on-line coupling of TRIGA-TRAP to the research reactor TRIGA Mainz will be used up to its full potential in the near future.

In the second part of this thesis, the processes ranging from sample preparation, through ionization and mass separation to the implantation of ^{163}Ho into calorimeter absorbers at the mass separator RISIKO was investigated and optimized. For the ECHo experiment it is required to embed an activity of about 1 Bq ($\approx 1.4 \cdot 10^{11}$ atoms ^{163}Ho) into a large number of individual calorimeter pixels. In the first phase of the experiment a total activity of 1 kBq is envisaged to reach a statistical sensitivity for the neutrino mass of < 2 eV. In the subsequent main measurement phase, this is supposed to be increased to 1 MBq. Furthermore, the embedded source should be free of any other radioactive isotopes to provide a clean spectrum. More specifically, the isotope most difficult to separate from ^{163}Ho is ^{166m}Ho. Here, the largest acceptable relative concentration in respect to ^{163}Ho is 10^{-9}. Finally, the process efficiency should be as high as possible. In the first experimental phase, a supply on the order of 10^{18} atoms is estimated, which gives a large margin for losses in the first phase. However, considering the larger scale experiment, an overall process efficiency of $> 5\,\%$ should be reached to alleviate the need to significantly increase the ^{163}Ho production rate.

The complete process was studied using stable ^{165}Ho as substitute for the precious ^{163}Ho. It could be shown that the transfer from Ho in solution to a dried out sample on small Ti substrate could be carried out without losses. Quantification was attained by neutron activation analysis, with which a good reproducibility of the sample sizes was confirmed. The ionization in RISIKO was carried out using a resonant laser ionization. A three step excitation scheme was chosen in which the lower two transitions were completely saturated by the pulsed Ti:sapphire laser light. The measured spectral pro-

files had bandwidths between 24 and 33 GHz, which is more than the typical variation of the laser wavelengths over a day. This allowed a stable operation without the need of an active wavelength stabilization. From several measurements with different sample sizes, an average ionization efficiency of 32(5) % was determined, which could be further increased to 40(6) % by modifications to the ion source geometry and layout. This value matches previous experiments [87, 95] and is amongst the highest efficiencies achieved by resonant laser ionization at all. Neighboring lanthanide elements in the sample were at the same time ionized 30 to 100 times less efficiently, further contributing to the purity of the ion beam. The subsequent mass separation by a sector field magnet suppressed ions of neighboring masses by at least four orders of magnitude. Based on this, the relative level of ^{166m}Ho is expected to be $5 \cdot 10^{-9}$ during implantations of ^{163}Ho. Finally, new focusing ion optics were installed that produced a beam spot of 0.62(2) mm × 1.01(6) mm size at the implantation position. Based on the 2 × 2 layout of the calorimeters used during testing, 14.5 % of the ion beam is implanted into the absorbers. In combination with the ionization efficiency a total efficiency of 6 % can be estimated for the implantation process.

Further developments will target the suppression of ^{166m}Ho ions. By quickly pulsing specific beam gate electrodes the main ion pulse following the laser ionization in the atomizer can be isolated. This will suppress lower energy ions created in front of the atomizer that currently limit the suppression of heavier ions when implanting lighter ions. In addition, a quadrupole triplet lens will be used to counteracted the astigmatic focusing of the separator magnet to further reduce the beam size in the implantation region. A combined microchannel plate and phosphorous screen detection system has been ordered to perform the beam profile measurements in a faster and more precise manner. The implementation of these concepts has already begun and is expected to be complete soon. Once the calorimeter design for the first ECHo measurement is finalized, RISIKO will be prepared to carry out ^{163}Ho implantations for the different stages of the present and future ECHo experiment at full performance.

Part IV

Appendix

Appendix A

Simulation studies of the Mini-RFQ ion source

The Mini-RFQ ion source was designed as an improvement to the previously existing laser ablation ion source [49], with the goal of increasing the relative yield from the ablation samples and decreasing the energy spread of the bunches to enhance the transmission through the low energy beamline and make a better mass separation by the time of flight possible. Furthermore, the use of a radiofrequency quadrupole offers the possibility of a mass selective operation. In case of the installation at TRIGA-TRAP this is less important because of the existing mass separation in the transport beamline, but it might be of interest for future applications at other experiments. To test these matters and the general feasibility, simulations of the ion trajectories in parallel to the design of the mechanical elements are mandatory. After finalizing the design, detailed simulations provide starting points, i.e. voltages for the different electrodes, at which an optimization process of the experiment can start.

The ion trajectories were simulated using the SIMION software [108], which is designed to calculate the electro- and magnetostatic fields in a system by solving the Laplace equation on a three dimensional equidistant grid with given boundary conditions [109]. SIMION uses *electrodes* as input, which are defined by the set of grid points that represent their geometrical dimensions and by their common potential. The geometry is defined beforehand by a set of geometrical functions or by importing parts from CAD software. The electrode potentials are treated in a scalable fashion to support arbitrary time dependent potentials in the simulation during runtime. The trajectory calculation itself is based on the electro- and magnetostatic forces on the partical which are integrated over discrete time steps to obtain a new set of position and velocity coordinates for the particle. The size of the time steps is chosen dynamically on the basis of the acceleration forces and the particle velocity to minimize computation time while maintaining a target accuracy. One of the key features of SIMION is the option to execute additional user scripts in every simulation step to test or modify many aspects of the particle and potential properties which expands the possibilities many fold.

The specific goal of the SIMION simulation of the Mini-RFQ ion source was to find a set of electrode voltages with which an ion bunch can be generated, stored, cooled, ejected and transported with maximum efficiency and minimum emittance. Furthermore the buffer gas cooling was to be tested to establish pressure and storage times necessary for thermalization and the capabilities of operating the Mini-RFQ ion source in a mass selective mode were to be studied.

A.1 SIMION Representation of the Mini-RFQ ion source

The geometry of the Mini-RFQ ion source ion source was modeled using the SIMION built-in functions with a grid resolution of 0.2 mm. To save memory, the planar symmetry in x and y direction was used (with z being the direction of the ion beam). In addition to the Mini-RFQ ion source itself, the first three electrodes used for extraction and collimation of the ion bunch were included in the simulations. Figure A.1 shows a section view of the model in SIMION. The buffer gas collisions are handled by an additional code segment *collisions HS1* included in SIMION and based on [110], which calculates hard sphere collisions between the ions and the gas, under assumption of constant pressure as well as Maxwell-Boltzmann distributed velocity of the buffer gas.

A.1.1 Ion initial conditions

An important aspect are the initial conditions for the created ions. Regarding the Mini-RFQ ion source, these initial conditions should reflect the laser ablation process in respect to the energy and angular distributions of the created ions. Thereby, the results obtained from the simulation should match closely to the experiment. But, in addition, ions with less ideal initial conditions, i.e., wider spread and larger energy, should be taken into account, to test the limits and reliability of the system in case of non expected behavior of the laser ablation.

The momentum and angular distributions for laser ablation, have been studied by several groups, e.g. [56, 111–113]. General consensus is an angular distribution proportional to a cosine power law $\cos^p(\phi)$. Konomi et al. [113] report values of p between 3 and 24 for ablation of various metals under similar conditions as to be expected in the Mini-RFQ ion source. The variation in these values correlates with the sublimation energy of the metals, with a larger sublimation energy corresponding to larger values of p, i.e., a narrower distribution. In a more general formalism, Kools et al. [112] predict values for p in a similar range, with p increasing with smaller laser spot sizes. Regarding the velocity or kinetic energy distribution, much more diverse values are reported, especially in the case of carbon cluster ions C_n^+. Whereas Choi et al. [111] measured velocity distributions matching a shifted Maxwell-Boltzmann

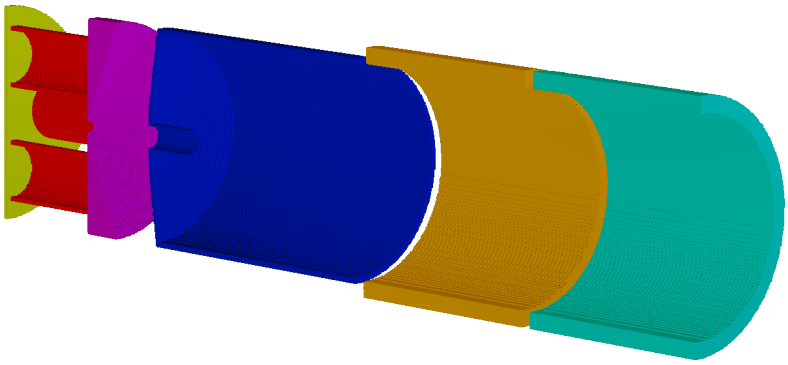

Figure A.1: Model of the Mini-RFQ ion source used for ion trajectory simulations in SIMION.

distribution with a forward energy of 0.005 to 0.5 eV (300 m/s to 3000 m/s) with an internal temperature of 100 to 300 K for C^+, Bae et al. [56] report an average kinetic energy of 15 eV for all clusters ranging from C^+ to C_{24}^+. Both groups assign the non-thermal initial velocity to effects in the laser produced plasma plume. Choi et al. interpret the wide range of temperature and forward velocities as an effect of the adiabatic expansion of the plume, in which thermal energy is converted to kinetic energy. All of these findings [56, 111–113] are reported for moderate laser fluences of 0.5 to 1 J/cm^{-2} in ablation processes. With higher laser fluences, nonlinear effects in the plasma lead to more drastic changes in energy and angular distribution of ions in the plume.

These conditions are implemented into SIMION by creating ions in a Monte-Carlo like fashion with random direction and kinetic energy in given bounds. For the angular distribution, the cosine power law was approximated by a step function $\Theta(\phi_0(p)-\phi)$ with $\phi_0(p)$ as the half-width-half-maximum of $\cos^p(\phi)$: $\phi_0(p) = \arccos((1/2)^{1/p})$. ϕ_0 was chosen as 30°, corresponding to $p = 5$. For the kinetic energy, a uniform distribution between 0.5 eV and 1.5 eV was chosen, independent of the direction. Finally, mass and charge state were chosen to match the isotopes that are planned to be measured and thus to be ionized in the Mini-RFQ ion source. As such, only singly charged ions of either mass $m = 179$ u (equivalent to $^{163}Ho^{16}O^+$) or $m = 264$ u (equivalent to, e.g., $^{248}Cm^{16}O^+$) were studied.

A.1.2 Simulation procedure

After creating ions with the given initial conditions, the trajectroy of each ion is simulated individually. SIMION is able to calculate ion-ion Coulomb rejection, but only with a significant increase in calculation time. As ion-gas collisions are expected to dominate the cooling process, such ion-ion interactions were not taken into account.

Using the *fast_adjust* procedure of SIMION, time dependent potentials are applied

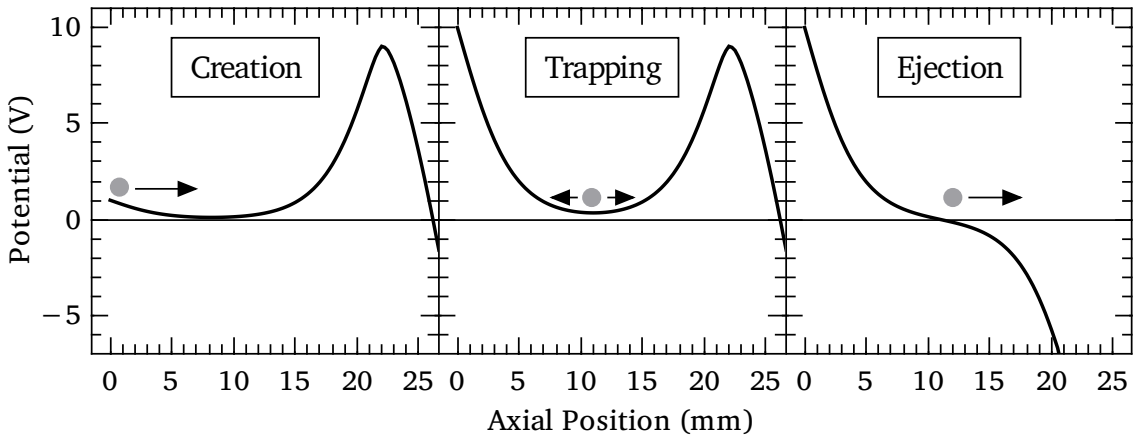

Figure A.2: Axial trapping potentials of the Mini-RFQ ion source during (left) ion creation, (center) while trapping and (right) for ejection of the ion bunch.

to several electrodes, namely the quadrupole rods to implement the RF field and the back and front electrodes of the Mini-RFQ ion source are pulsed for trapping and ejection of ions. With this, the following trapping scheme is implemented: During the laser pulse, the back electrode with the target is kept at a potential just above the mean potential of the RFQ rods. After a short delay, the back electrode is pulsed up to the same potential as the front electrode to have a symmetric trap. For ejection, the potential of the front electrode is pulsed down to the mean level or below that. The trapping potentials on the center axis for a potential difference of 10 V between the endcaps and the RFQ rods are shown in fig. A.2. The potential wall corresponding to the front electrode does not extend to 10 V because the potential on the outside penetrates through the extraction aperture. For the same reason, extracting the ions would be possible with the front electrode on the same potentials as the rods. Pulsing the front electrode to lower potentials changes the longitudinal velocity distribution and thus can be optimized to have the ion bunch focus in time at a certain point in the beam line.

For the data evaluation, the kinetic energy of the trapped ion is recorded every 100 ns, as well as the full kinetic properties (position, velocity, energy and time of flight) are recorded after the ion hits an electrode or is transmitted to the end of the simulated beamline. Because of the random distribution of initial conditions and the buffer gas collisions, the SIMION simulations are non-deterministic, i.e., Monte-Carlo simulations. To obtain meaningful results, the simulation has to be run several times with the same settings to accumulate enough statistics. Thus, 50 to 200 ions were simulated for each parameter set and the observable of interest acquired by the mean value of all ions, and its uncertainty by the standard deviation of these values.

Table A.1: Initial parameter set for the Mini-RFQ ion source simulations.

Parameter	Value
Target offset	1 V
Axial trap depth	10 V
RF Frequency	1 MHz
RF Amplitude	476 V
Buffer gas pressure	10^{-3} mbar
Extraction pulse	100 V
Target pulse delay	10 µs
Trapping duration	2 ms
First electrode	-200 V

A.2 Simulation results

The first goal of the simulations was to find a set of parameters that allows trapping, cooling and extracting of the ions. This set of parameters is given in tab. A.1. Starting from there, targeted variations of parameters allows to optimize the system towards a specific goal.

Buffer gas pressure The first parameter to be studied was the helium buffer gas pressure. In the experiment, the pressure will be one of the parameters most difficult to set, because no direct measurement is possible. It is defined by a given gas flow into the system and the leak rate through the apertures in the Mini-RFQ ion source. Thus, knowledge of the consequences of different pressure ranges is necessary for optimization. In principle, the mean free path is inversely proportional and therefore, the collision rate is proportional to the pressure. Thus, with higher pressures, the time necessary to dissipate the kinetic energy of the ions is lower with higher gas pressures. But, too high pressures may lead to electrical discharges in the Mini-RFQ ion source and in addition raise the pressures in the subsequent beamline all the way to the Penning traps and may prevent usage of those in the desired manner.

The simulations were performed in the range from 10^{-5} mbar to 0.1 mbar. In fig. A.3 the kinetic energy in axial $E_{ax} = {}^1/_2\, m v_z^2$ and radial direction $E_{rad} = {}^1/_2\, m\,(v_x^2 + v_y^2)$ is shown for one of the ions simulated at a buffer gas pressure of 0.01 mbar. The initial axial motion was cooled in 300 µs to the final value of about 0.12 eV. In contrast, the radial motion initially is damped faster, but during the course is several times increased again by up to 1 eV.

From the course of the kinetic energy of 50 particles for each pressure, the mean kinetic energy in the last 200 µs was extracted as a measure of the attainable final

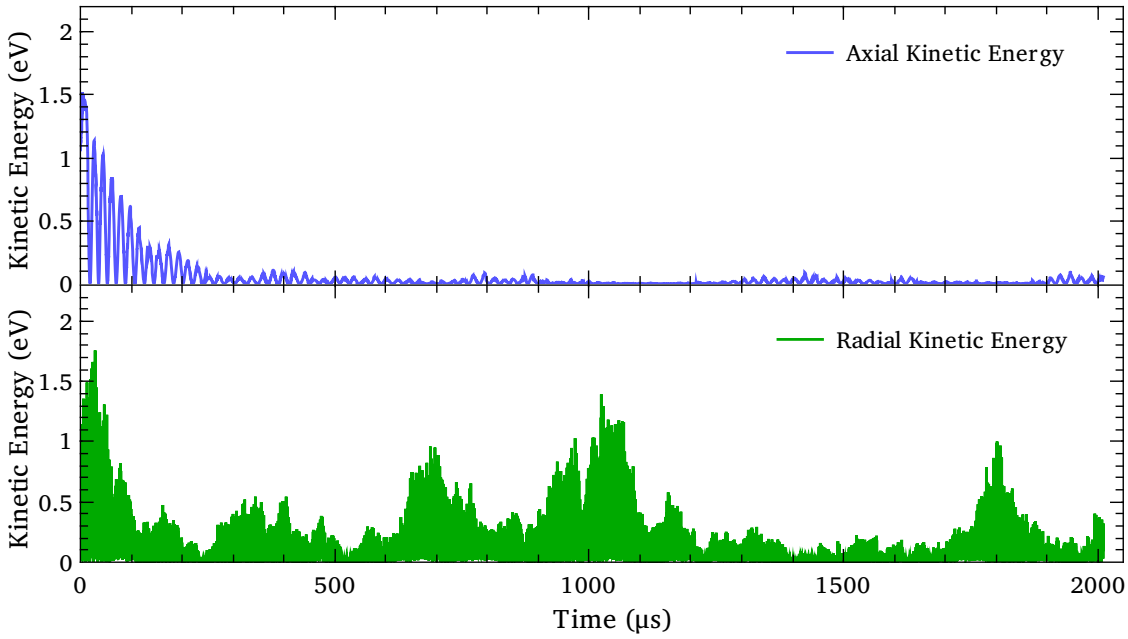

Figure A.3: Course of the kinetic energy in axial and radial direction of a trapped ion in the Mini-RFQ ion source at a buffer gas pressure of 0.01 mbar.

energy. With an exponential fit to the data, the half-life of the collisional damping was evaluated. Because of the possible increases in radial energy, only fits to the axial data provide useful data. Figure A.4a shows the attained final energies at different pressures. The trend shows that a trapping period of 2 µs is barely long enough to cool the ions to the lowest attainable energies at a pressure of 10^{-3} mbar. With lower pressures, only little energy is dissipated, while at higher pressures the final energy levels stay the same. The evaluation of the axial damping half-life shown in fig. A.4b further confirms the expected antiproportional dependence.

Radiofrequency Amplitude As depicted in fig. A.3, the buffer gas collisions can possibly cause large increases in radial kinetic energy. This is caused by the nature of the confining force created by the radiofrequency field. In fig. A.5 the mean kinetic energies after trapping at different radiofrequency amplitudes are depicted. Whereas the energy in axial direction is independent of the amplitude, the energy in radial direction increases strongly with amplitudes above 400 V. With amplitudes outside of the range shown in fig. A.5, no trapping for the full duration was possible. The high amplitude cutoff is in agreement with the results from Mathieu differential equations [].

For an operation without DC offset voltages, i.e., $a = 0$, the region of stability extends to $q \leq 0.908$. This equals to an amplitude of $V = 621\,\mathrm{V}$ for $m = 264\,\mathrm{u}$. At low RF amplitudes, the motion of a particle starting in rest is still stable. But, ions entering with a large deflection angle from the ablation process, perform a drift motion with

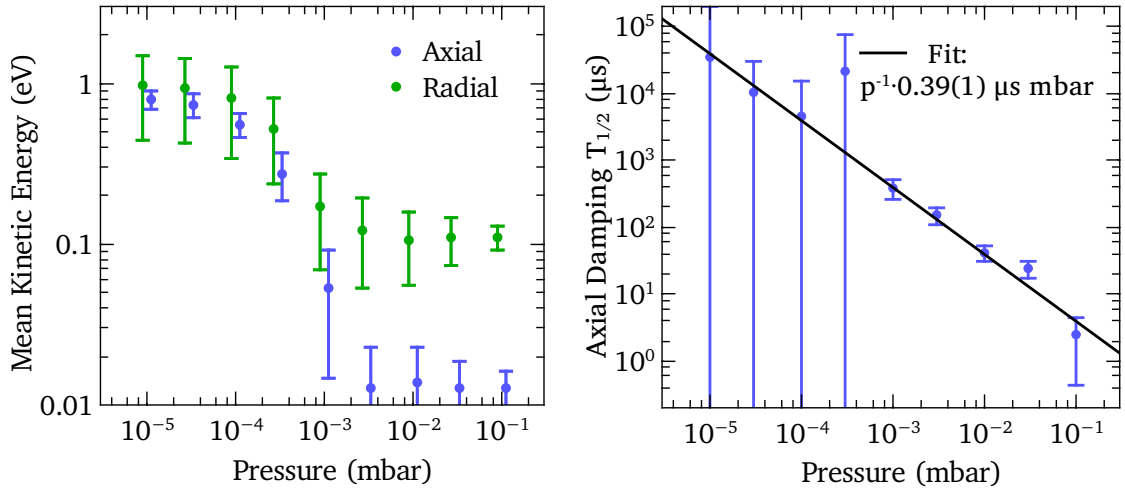

(a) Mean kinetic energy after trapping. (b) Damping constant of the axial motion.

Figure A.4: Results obtained from SIMION simulation of the Mini-RFQ ion source at different helium buffergas pressures and 2 ms trapping time.

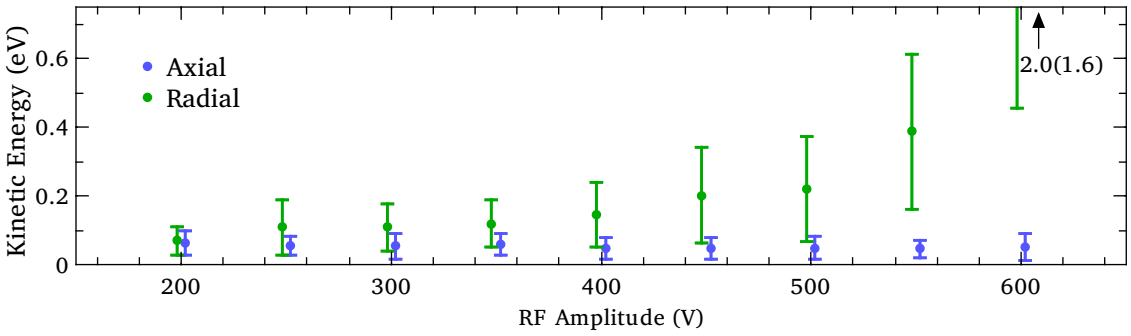

Figure A.5: Mean kinetic energies at different RF amplitudes after trapping for 2 ms at a buffer gas pressure of 0.01 mbar.

only a very low oscillation effect caused by the trapping potential. As such, no ions can be trapped for longer than 100 µs with RF amplitudes below 40 V. And even if the ions are not lost during the trapping, their final radial displacement and energy are too large to efficiently transmit them into the subsequent beamline.

Mass selective operation Another advantage of the Mini-RFQ ion source in comparison to a simple laser ablation ion source is the possibility of applying mass separation directly in the ion source. For this, in addition to the RF field with amplitude V, DC potentials U are applied to the rods. To one pair of opposing rods U is applied, to the other pair of rods $-U$, respectively. Figure A.6 depicts the transmission chance for ions out of the Mini-RFQ ion source into the subsequent beamline for different U und V. The boundaries of the region of stability from the Mathieu differential equations are overlaid in black. In general, the Mini-RFQ ion source behaves similar to an

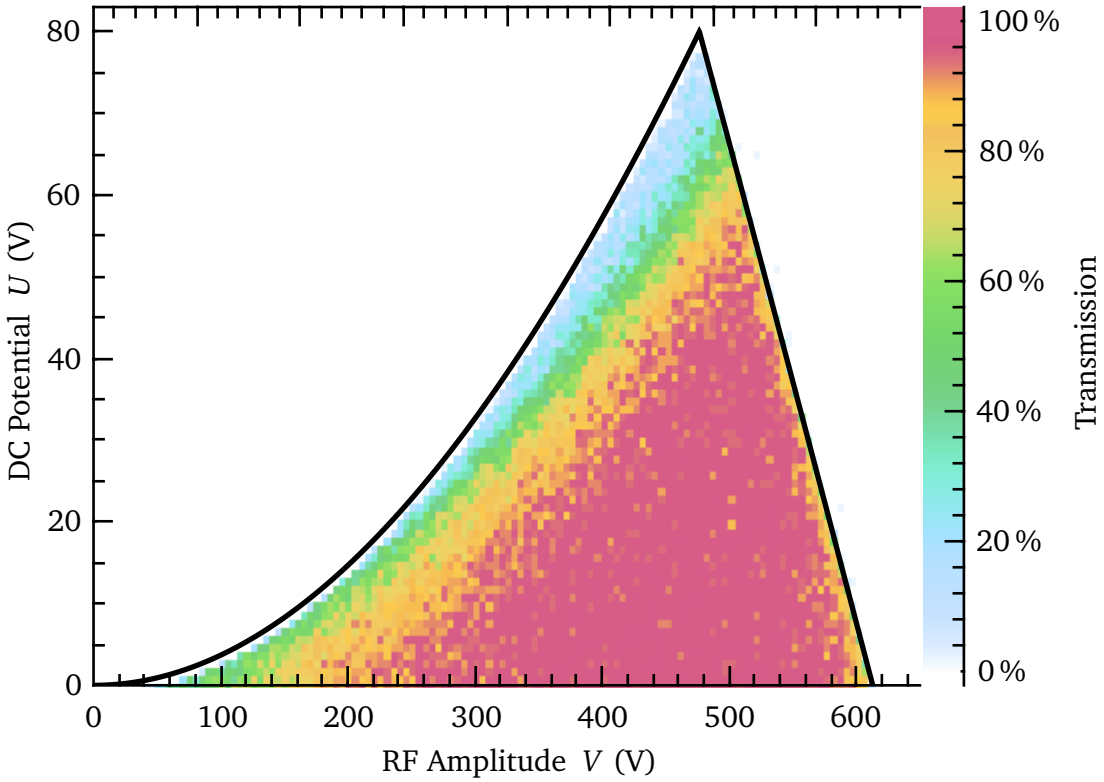

Figure A.6: Transmission from the Mini-RFQ ion source to the subsequent beamline in dependence on the applied DC potential U and RF amplitude V. Overlaid in black are the boundaries of the region of stability defined by the Mathieu differential equations.

ideal trap. Interestingly, close the left border, the transmission decreases gradually. Here ions still have stable trajectories inside the Mini-RFQ ion source, but their radii increases. Thus, they can not be efficiently extracted through exit aperture and the extraction electrode.

Therefore, if mass separation is required, then a compromise has to be taken between the achievable mass resolution and the efficiency of the system. For example, operation at the highest point with full transmission for $m = 264\,\mathrm{u}$, $U = 58\,\mathrm{V}$ and $V = 500\,\mathrm{V}$, contaminant ions with masses below 214 u or above 411 u are completely removed. If a narrower transmission window is desired, e.g., with a width of 30 u, the Mini-RFQ ion source would have to be operated with $U = 74\,\mathrm{V}$ and $V = 476\,\mathrm{V}$ where less than 10 % of the ions are transmitted.

Extraction Pulse The TRIGA-TRAP beamline comprises fast switchable electrodes to select a certain m/q range from the ion bunch by their flight time. To achieve a high separation power, the bunch length should be as short as possible. In the Mini-RFQ ion source the bunch length is controlled by the extraction pulse applied to the front electrode. With increasing magnitude, the electric field along the trap axis increases and

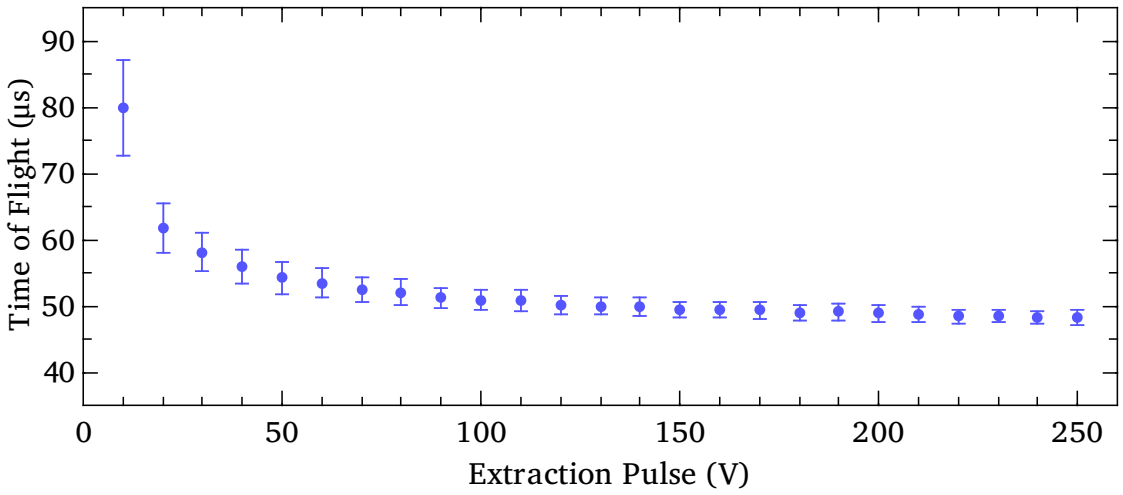

Figure A.7: Flight time and duration of an ejected ion bunch towards a detector positioned 1 m downstream.

the ions are ejected more quickly (see fig. A.2). Figure A.7 shows the simulated flight time and bunch length of the ions recorded at a detector plane 1 m downstream. The ions were accelerated to an energy of 1 keV after being trapped for 2 ms at 10^{-3} mbar. With increasing extraction pulse heights, the flight time as well as the bunch length decrease due to the faster ejection. At extraction pulse heights above 200 V the bunch length is about 2 µs. In comparison, a 2 µs separation corresponds to a mass difference of 20 u to 25 u. Although the geometry of the Mini-RFQ ion source is similar to the two-stage extraction systems used in time-of-flight mass spectrometers [114], the RFQ rods modify the axial potential and thus render a homogeneous electric field for extraction impossible. Therefore, a direct tuning of the time-focusing is not possible beyond what is shown in fig. A.7. Nevertheless, a pulse length of 2 µs is short enough for a coarse mass separation and most importantly, for efficient capturing in the preparation Penning trap.

Appendix B

Mass Measurement Fit Parameters

The figures B.1,B.2 and B.3 list the parameters obtained from curve fitting to the time-of-flight spectra. Although there are some outlying data points, in general the values are all in the desired region. This is especially true for the initial magnetron radius r_{-}, where larger radii than 0.3 mm possibly induce frequency shifts by the residual anharmonicity of the trap potential.

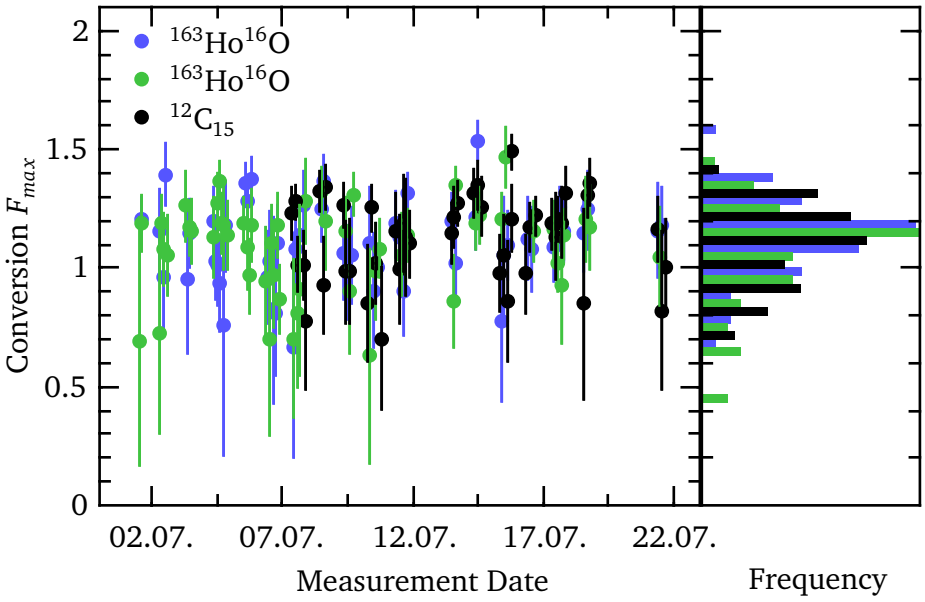

Figure B.1: Values obtained from curve fitting for $F_{\max}$ as indicator of the degree of conversion.

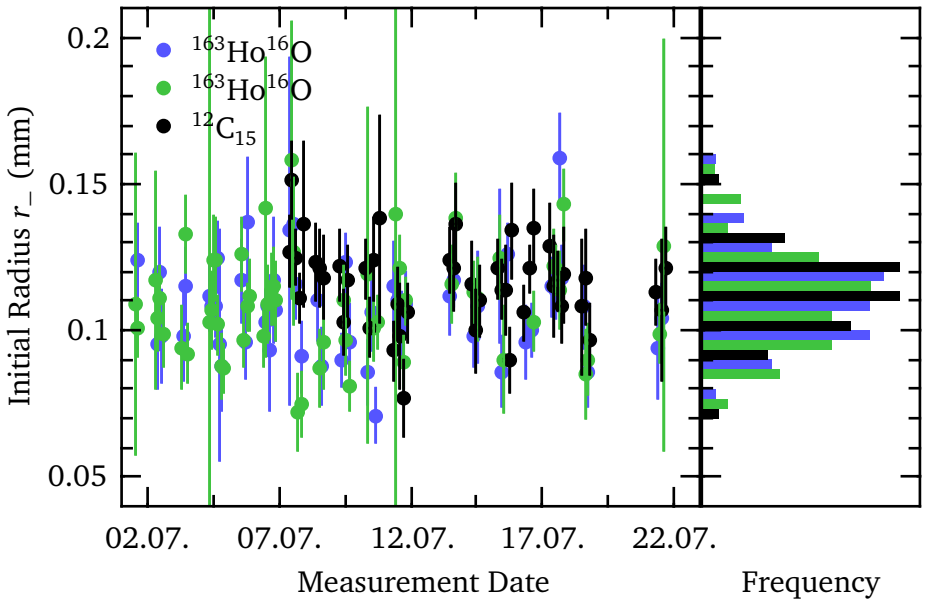

Figure B.2: Values obtained from curve fitting for the initial magnetron radius r_-.

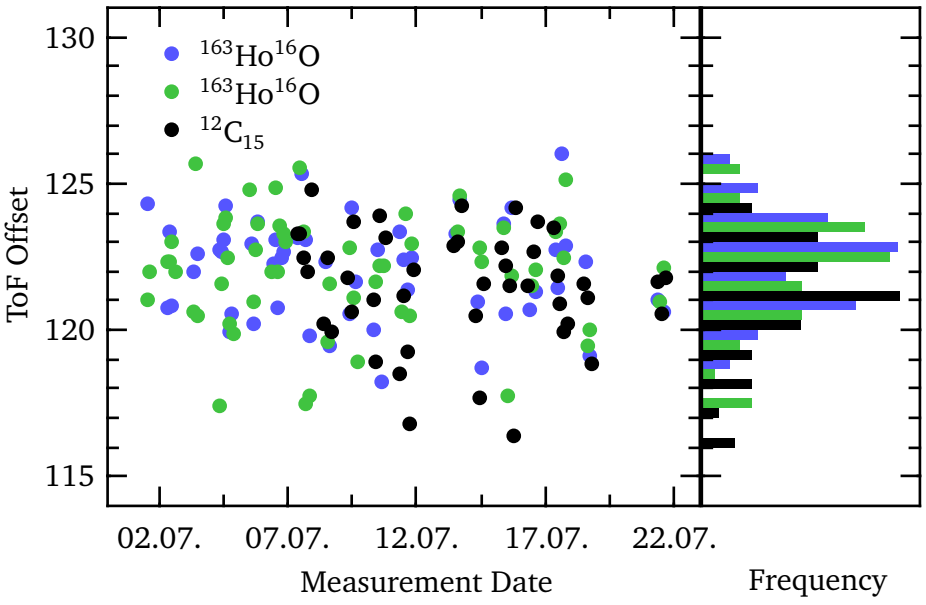

Figure B.3: Values obtained from curve fitting for T_{offset}, the flight time for an ion without any rotational energy.

List of Figures

2.1 Calculated de-excitation spectrum 5
2.2 Metallic magnetic calorimeter 6
2.3 *Q*-values from literature 14

3.1 TRIGA-SPEC setup 16
3.2 3D model of the Mini-RFQ ion source 17
3.3 Ablation target 18
3.4 Laser system for the Mini-RFQ ion source 19
3.5 Schematic representation of the TRIGA-TRAP setup 20

4.1 ToF distribution of ions in front of the Penning traps 25
4.2 Mass-selective resonant buffer-gas cooling spectrum 27
4.3 Time of Flight Ion Cyclotron Resonance spectrum 29
4.4 Reference cyclotron frequency interpolation 31
4.5 Cyclotron frequency ratios for $^{163}Ho^{16}O^{+}$ to $^{163}Dy^{16}O^{+}$ 34
4.6 Relative mass uncertainties for elements from Z=56 to Z=80 35

5.1 Schematic view of the RISIKO mass separator. Taken from [76]. 41
5.2 Computer rendered view of the ion source region. 42

6.1 Excitation scheme for holmium 49
6.2 Resonances and saturation curves of the three transitions 51
6.3 Overview of the measured ionization efficiencies for holmium 52
6.4 Measurement of ionization efficiency 54
6.5 Ion source temperature distributions 55
6.6 Transmission peak of $^{165}Ho^{+}$ 55
6.7 Mass spectra of the ^{163}Ho sample 57
6.8 Depth profile for the implantation of ^{163}Ho ions 58
6.9 Photograph of a microcalorimeter mounted in the Faraday cup 60

7.1 Comparison of atomizer mounting designs 65
7.2 Measured ionization efficiencies for holmium with the improved atomizer mounting 66
7.3 Measurement of ionization efficiency with new atomizer mounting . . 67
7.4 Transmission peak of $^{165}Ho^{+}$ and calculated scattering background . . 68

7.5 Potential and field strength of the acceleration field 70
7.6 Temporal ion bunch shape of resonantly ionized ^{174}Yb 71
7.7 Ion current versus flight time and nominal mass 73
7.8 RISIKO detection region before the upgrade 75
7.9 Upgraded RISIKO detection region 75
7.10 Cut view of the refocusing optics 76
7.11 3D model of the new refocusing optics 77
7.12 Focusing voltages for different beam opening angles 78

A.1 Model of the Mini-RFQ ion source used for ion trajectory simulations in SIMION 91
A.2 Axial trapping potentials of the Mini-RFQ ion source 92
A.3 Simulated kinetic energy of a trapped ion 94
A.4 SIMION simulation results for kinetic energy and axial damping 95
A.5 Mean kinetic energies at different RF amplitudes 95
A.6 Region of transmission from the Mini-RFQ ion source to the subsequent beamline 96
A.7 Flight time and duration of an ejected ion bunch 97

B.1 Values obtained from curve fitting for F_{max} 99
B.2 Values obtained from curve fitting for r_{-} 100
B.3 Values obtained from curve fitting for T_{offset} 100

List of Tables

2.1 ^{163}Ho sample content 9

3.1 Mini-RFQ ion source design parameters 18

4.1 Optimized and simulated Mini-RFQ ion source parameters 24
4.2 Excitation durations and amplitudes in the Penning traps 26
4.3 Carbon cluster frequency ratios 32
4.4 Results of the atomic mass measurements of ^{163}Ho and ^{163}Dy 33

6.1 Analysis results of the prepared samples 48
6.2 Spectroscopic results for the three transitions 51
6.3 Operational parameters of RISIKO 52
6.4 Assumed constitution of the ion beam during ^{163}Ho implantation . . . 58

7.1 Temperatures of the atomizer near the combined mounting point . . . 66
7.2 Results from simulated ion trajectories 78

A.1 Initial parameter set for the Mini-RFQ ion source simulations. 93

Bibliography

[1] E. Fermi, "Versuch einer Theorie der β-Strahlen I", Z. Phys. **88**, 161–177 (1934) 10.1007/BF01351864 (cit. on p. 1).

[2] C. L. Cowan et al., "Detection of the free neutrino: a confirmation", Science **124**, 103–104 (1956) 10.1126/science.124.3212.103 (cit. on p. 1).

[3] R. Davis, D. S. Harmer, and K. C. Hoffman, "Search for neutrinos from the sun", Phys. Rev. Lett. **20**, 1205–1209 (1968) 10.1103/PhysRevLett.20.1205 (cit. on p. 1).

[4] B. Pontecorvo, "Mesonium and antimesonium", Sov. Phys. JETP **6**, 429–431 (1958) (cit. on p. 1).

[5] B. Pontecorvo, "Inverse beta processes and nonconservation of lepton charge", Sov. Phys. JETP **7**, 172–173 (1958) (cit. on p. 1).

[6] G. Danby et al., "Observation of high-energy neutrino reactions and the existence of two kinds of neutrinos", Phys. Rev. Lett. **9**, 36–44 (1962) 10.1103/PhysRevLett.9.36 (cit. on p. 1).

[7] B. Pontecorvo, "Neutrino experiments and the problem of conservation of leptonic charge", Sov. Phys. JETP **26**, 984–988 (1968) (cit. on p. 1).

[8] Q. R. Ahmad et al., "Measurement of the rate of $\nu_e + d \rightarrow p + p + e^-$ interactions produced by ^8B solar neutrinos at the Sudbury Neutrino Observatory", Phys. Rev. Lett. **87**, 071301 (2001) 10.1103/PhysRevLett.87.071301 (cit. on p. 2).

[9] S. Fukuda et al., "Solar ^8B and hep neutrino measurements from 1258 days of Super-Kamiokande data", Phys. Rev. Lett. **86**, 5651–5655 (2001) 10.1103/PhysRevLett.86.5651 (cit. on p. 2).

[10] K. Olive and P. D. Group, "Review of particle physics", Chin. Phys. C **38**, 090001 (2014) (cit. on p. 2).

[11] E. Komatsu et al., "Seven-year Wilkinson Microwave Anisotropy Probe (WMAP) observations: cosmological interpretation", Astrophys. J. Suppl. S. **192**, 18 (2011) (cit. on p. 2).

[12] E. Majorana, "Teoria simmetrica dell'elettrone e del positrone", Nuovo Cimento **14**, 171–184 (1937) 10.1007/BF02961314 (cit. on p. 2).

[13] V. N. Aseev et al., "Upper limit on the electron antineutrino mass from the Troitsk experiment", Phys. Rev. D **84**, 112003 (2011) 10.1103/PhysRevD.84.112003 (cit. on p. 3).

[14] C. Kraus et al., "Final results from phase II of the Mainz neutrino mass search in tritium β decay", Eur. Phys. J. C **40**, 447–468 (2005) 10.1140/epjc/s2005-02139-7 (cit. on p. 3).

[15] KATRIN Collaboration, *KATRIN design report 2004* (2005) (cit. on p. 3).

[16] A. Monfardini et al., "The microcalorimeter arrays for a rhenium experiment (MARE): A next-generation calorimetric neutrino mass experiment", Nucl. Instrum. Meth. A **559**, 346–348 (2006) 10.1016/j.nima.2005.12.006 (cit. on p. 3).

[17] A. D. Rújula and M. Lusignoli, "Calorimetric measurements of 163-holmium decay as tools to determine the electron neutrino mass", Phys. Lett. B **118**, 429–434 (1982) 10.1016/0370-2693(82)90218-0 (cit. on p. 3).

[18] B. Alpert et al., "HOLMES: The electron capture decay of Ho-163 to measure the electron neutrino mass with sub-eV sensitivity", Eur. Phys. J. C **75**, 112 (2015) 10.1140/epjc/s10052-015-3329-5 (cit. on p. 3).

[19] M. P. Croce et al., "Development of holmium-163 electron-capture spectroscopy with transition-edge sensors", J. Low Temp. Phys., 1–11 (2016) 10.1007/s10909-015-1451-2 (cit. on p. 3).

[20] L. Gastaldo et al., "The Electron Capture Ho-163 Experiment ECHo", J. Low Temp. Phys. **176**, 876–884 (2014) 10.1007/s10909-014-1187-4 (cit. on pp. 3, 6).

[21] F. Schneider et al., "Preparatory studies for a high-precision Penning-trap measurement of the ^{163}Ho electron capture Q-value", Eur. Phys. J. A **51**, 89 (2015) 10.1140/epja/i2015-15089-8 (cit. on pp. 5, 13, 17, 18, 20, 25).

[22] J. Andersen et al., "A limit on the mass of the electron neutrino: the case of ^{163}Ho", Phys. Lett. B **113**, 72–76 (1982) 10.1016/0370-2693(82)90112-5 (cit. on pp. 5, 14).

[23] S. Yasumi et al., "The mass of the electron neutrino using electron capture in ^{163}Ho", Phys. Lett. B **181**, 169–172 (1986) 10.1016/0370-2693(86)91277-3 (cit. on pp. 5, 14).

[24] P. T. Springer, C. L. Bennett, and P. A. Baisden, "Measurement of the neutrino mass using the inner bremsstrahlung emitted in the electron-capture decay of ^{163}Ho", Phys. Rev. A **35**, 679–689 (1987) 10.1103/PhysRevA.35.679 (cit. on pp. 5, 6).

[25] F. Hartmann and R. Naumann, "High-temperature gas proportional detector techniques and application to the neutrino mass limit using Ho-163", Nucl. Instrum. Meth. A **313**, 237–260 (1992) 10.1016/0168-9002(92)90102-A (cit. on pp. 5, 14, 35).

[26] M. Galeazzi et al., "The electron capture decay of 163-Ho to measure the electron neutrino mass with sub-ev accuracy (and beyond)", arXiv, 1202.4763 (2012) (cit. on p. 6).

[27] P.-C. O. Ranitzsch et al., "Development of Metallic Magnetic Calorimeters for High Precision Measurements of Calorimetric Re-187 and Ho-163 Spectra", J. Low Temp. Phys. **167**, 1004–1014 (2012) 10.1007/s10909-012-0556-0 (cit. on pp. 6, 7, 14, 35, 39, 83).

[28] L. Gastaldo et al., "Characterization of low temperature metallic magnetic calorimeters having gold absorbers with implanted ^{163}Ho ions", Nucl. Instrum. Meth. A **711**, 150–159 (2013) http://dx.doi.org/10.1016/j.nima.2013.01.027 (cit. on p. 6).

[29] C. Pies et al., "maXs: microcalorimeter arrays for high-resolution X-ray spectroscopy at GSI/FAIR", J. Low Temp. Phys. **167**, 269–279 (2012) 10.1007/s10909-012-0557-z (cit. on p. 6).

[30] S. Kempf et al., "Multiplexed readout of MMC detector arrays using non-hysteretic rf-SQUIDs", J. Low Temp. Phys. **176**, 426–432 (2013) 10.1007/s10909-013-1041-0 (cit. on p. 6).

[31] J. W. Engle et al., "Evaluation of Ho-163 production options for neutrino mass measurements with microcalorimeter detectors", Nucl. Instrum. Meth. B **311**, 131–138 (2013) 10.1016/j.nimb.2013.06.017 (cit. on p. 7).

[32] U. Köster, M. Günther, and D. Habs, "Production of radioisotopes with high specific activity by photonuclear reactions: from a "wild idea" to reality", Radiother. Oncol. **102**, ICTR-PHE 2012 Conference, S102–S103 (2012) 10.1016/S0167-8140(12)70177-9 (cit. on p. 7).

[33] H. Dorrer, "Production, isolation, and characterization of pure ^{163}Ho for the ECHo-project", in preparation (cit. on pp. 8, 56).

[34] S. Eliseev, private communication (cit. on p. 8).

[35] M. Wang et al., "The AME2012 atomic mass evaluation (II). Tables, graphs and references", Chin. Phys. C **36**, 1603–2014 (2012) 10.1088/1674-1137/36/12/003 (cit. on pp. 13, 14, 33, 35, 83).

[36] M. Eibach et al., "Direct high-precision mass measurements on Am-241, Am-243, Pu-244, and Cf-249", Phys. Rev. C **89**, 064318 (2014) 10.1103/PhysRevC.89.064318 (cit. on p. 13).

[37] S. Eliseev et al., "Phase-imaging ion-cyclotron-resonance measurements for short-lived nuclides", Phys. Rev. Lett. **110**, 082501 (2013) 10.1103/PhysRevLett.110.082501 (cit. on pp. 13, 35, 84).

[38] S. Eliseev et al., "Direct Measurement of the Mass Difference of ^{163}Ho and ^{163}Dy Solves the Q-Value Puzzle for the Neutrino Mass Determination", Phys. Rev. Lett. **115**, 062501 (2015) 10.1103/PhysRevLett.115.062501 (cit. on pp. 13, 84).

[39] P. A. Baisden et al., "Measurement of the half-life of ^{163}Ho", Phys. Rev. C **28**, 337–341 (1983) 10.1103/PhysRevC.28.337 (cit. on p. 14).

[40] E. Laegsgaard et al., "The capture ratio N/M in the ec beta decay of Ho-163", in Proceedings of the Seventh International Conference on Atomic Masses and Fundamental Constants (AMCO-7), edited by p. 6. Klepper, O. (1984), pp. 652–658 (cit. on p. 14).

[41] F. X. Hartmann and R. A. Naumann, "Observation of N and M orbital-electron capture in the decay of ^{163}Ho", Phys. Rev. C **31**, 1594–1596 (1985) 10.1103/PhysRevC.31.1594 (cit. on p. 14).

[42] F. Bosch and M. Jung, in *Annual Report* (Gesellschaft für Schwerionenforschung, 1993), p. 65 (cit. on pp. 14, 35).

[43] S. Yasumi et al., "The mass of the electron neutrino from electron capture in ^{163}Ho", Phys. Lett. B **334**, 229–233 (1994) 10.1016/0370-2693(94)90616-5 (cit. on p. 14).

[44] F. Gatti et al., "Calorimetric measurement of the Ho-163 spectrum by means of a cryogenic detector", Phys. Lett. B **398**, 415–419 (1997) 10.1016/S0370-2693(97)00239-6 (cit. on pp. 14, 35).

[45] J. Ketelaer et al., "TRIGA-SPEC: A setup for mass spectrometry and laser spectroscopy at the research reactor TRIGA Mainz", Nucl. Instrum. Meth. A **594**, 162–177 (2008) 10.1016/j.nima.2008.06.023 (cit. on p. 15).

[46] J. Grund et al., "Implementation of an aerodynamic lens for TRIGA-SPEC", Nucl. Instrum. Meth. B **376**, 225–228 (2016) 10.1016/j.nimb.2015.12.017 (cit. on p. 15).

[47] T. Beyer et al., "An RFQ cooler and buncher for the TRIGA-SPEC experiment", Appl. Phys. B **114**, 129–136 (2013) 10.1007/s00340-013-5719-4 (cit. on pp. 15, 17).

[48] C. Gorges et al., "Isotope shift of ^{40,42,44,48}Ca in the $4s^2S_{1/2} \rightarrow 4p^2P_{3/2}$ transition", J. Phys. B **48**, 245008 (2015) 10.1088/0953-4075/48/24/245008 (cit. on p. 15).

[49] C. Smorra et al., "A carbon-cluster laser ion source for TRIGA-TRAP", J. Phys. B **42**, 154028 (2009) 10.1088/0953-4075/42/15/154028 (cit. on pp. 15, 89).

[50] F. Herfurth, "Segmented linear RFQ traps for nuclear physics", Nucl. Instrum. Meth. B **204**, 14th International Conference on Electromagnetic Isotope Separators and Techniques Related to their Applications, 587–591 (2003) 10.1016/S0168-583X(02)02135-3 (cit. on p. 17).

[51] K. Blaum et al., "Carbon clusters for absolute mass measurements at ISOLTRAP", Eur. Phys. J. A **15**, 245–248 (2002) 10.1140/epja/i2001-10262-4 (cit. on p. 19).

[52] J. Ketelaer et al., "Accuracy studies with carbon clusters at the Penning trap mass spectrometer TRIGA-TRAP", Eur. Phys. J. D **58**, 47–52 (2010) 10.1140/epjd/e2010-00092-9 (cit. on p. 19).

[53] R. Jones, "Density functional study of carbon clusters $C_{2n}(2 \leq n \leq 16)$. I: Structure and bonding in the neutral clusters", J. Chem. Phys. **110**, 5189–5200 (1999) 10.1063/1.478414 (cit. on p. 19).

[54] P. R. C. Kent et al., "Carbon clusters near the crossover to fullerene stability", Phys. Rev. B **62**, 15394–15397 (2000) 10.1103/PhysRevB.62.15394 (cit. on p. 19).

[55] G. Savard et al., "A new cooling technique for heavy ions in a Penning trap", Phys. Lett. A **158**, 247–252 (1991) 10.1016/0375-9601(91)91008-2 (cit. on pp. 21, 24).

[56] C. H. Bae and S. M. Park, "A time-of-flight quadrupole mass spectrometric study of C_n^+ (n=1–24) ions produced by laser ablation of a graphite target", J. Chem. Phys. **117**, 5347–5353 (2002) 10.1063/1.1500356 (cit. on pp. 23, 90, 91).

[57] G. Gräff, H. Kalinowsky, and J. Traut, "A direct determination of the proton electron mass ratio", Z. Phys. A **297**, 35–39 (1980) 10.1007/BF01414243 (cit. on p. 25).

[58] G. Bollen et al., "The accuracy of heavy-ion mass measurements using time of flight-ion cyclotron resonance in a Penning trap", J. of Appl. Phys. **68**, 4355–4374 (1990) 10.1063/1.346185 (cit. on p. 25).

[59] M. König et al., "Quadrupole excitation of stored ion motion at the true cyclotron frequency", Int. J. Mass Spectrom. **142**, 95–116 (1995) 10.1016/0168-1176(95)04146-C (cit. on pp. 25, 28).

[60] L. S. Brown and G. Gabrielse, "Precision spectroscopy of a charged particle in an imperfect Penning trap", Phys. Rev. A **25**, 2423–2425 (1982) 10.1103/PhysRevA.25.2423 (cit. on p. 25).

[61] G. Gabrielse, "The true cyclotron frequency for particles and ions in a Penning trap", Int. J. Mass Spectrom. **279**, 107–112 (2009) 10.1016/j.ijms.2008.10.015 (cit. on pp. 25, 32).

[62] S. George et al., "Ramsey method of separated oscillatory fields for high-precision Penning trap mass spectrometry", Phys. Rev. Lett. **98**, 162501 (2007) 10.1103/PhysRevLett.98.162501 (cit. on pp. 26, 30).

[63] C. Roux et al., "Data analysis of *Q*-value measurements for double-electron capture with SHIPTRAP", Eur. Phys. J. D **67**, 146 (2013) 10.1140/epjd/e2013-40110-x (cit. on pp. 28, 30, 32).

[64] G. Bollen et al., "Resolution of nuclear ground and isomeric states by a Penning trap mass spectrometer", Phys. Rev. C **46**, R2140–R2143 (1992) 10.1103/PhysRevC.46.R2140 (cit. on p. 28).

[65] S. George, "Application of the Ramsey method in high-precision Penning trap mass spectrometry", Diploma thesis (Universität Münster, 2005) (cit. on p. 29).

[66] Robert S. Van Dyck Jr. et al., "The UW-PTMS: systematic studies, measurement progress, and future improvements", Int. J. Mass Spectrom. **251**, 231–242 (2006) 10.1016/j.ijms.2006.01.038 (cit. on p. 33).

[67] S. Eliseev et al., "A phase-imaging technique for cyclotron-frequency measurements", Appl. Phys. B **114**, 107–128 (2014) 10.1007/s00340-013-5621-0 (cit. on p. 35).

[68] J. Repp et al., "PENTATRAP: A novel cryogenic multi-Penning-trap experiment for high-precision mass measurements on highly charged ions", Appl. Phys. B **107**, 983–996 (2012) 10.1007/s00340-011-4823-6 (cit. on p. 35).

[69] C. Roux et al., "The trap design of PENTATRAP", Appl. Phys. B **107**, 997–1005 (2012) 10.1007/s00340-011-4825-4 (cit. on p. 35).

[70] K. Chrysalidis, "Probenpräparation für das ECHo-Projekt - Effizienzmessungen an stabilem Holmium 165 am RISIKO-Massenseparator", B.Sc. thesis (Johannes Gutenberg-Universität Mainz, 2014) (cit. on pp. 39, 49, 53).

[71] R. Haas, "Radiochemische Holmium-Probenpräparation für den RISIKO-Massenseparator für das ECHo-Projekt", B.Sc. thesis (Johannes Gutenberg-Universität Mainz, 2014) (cit. on pp. 39, 46, 48).

[72] T. Kieck, "Adaption des RISIKO Massenseparators zur Anreicherung und Implantation von ^{163}Ho für das ECHo Projekt", Staatsexamensarbeit (Johannes Gutenberg-Universität Mainz, 2015) (cit. on pp. 39, 53, 59, 60, 64).

[73] S. Junck, "Nachfokussierung des Ionenstrahls des RISIKO-Massenseparators zur Holmium-Implantation für das ECHo Projekt", B.Sc. thesis (Johannes Gutenberg-Universität Mainz, 2015) (cit. on pp. 39, 74).

[74] S. Schmidt, "Optimierung der Temperaturverteilung in der Ionenquelle des RISIKO-Massenseparators", Staatsexamensarbeit (Johannes Gutenberg-Universität Mainz, 2015) (cit. on pp. 39, 64–66).

[75] S. Kormannshaus, "Nachfokussierung und Optimierung der Implantation von ^{163}Ho im RISIKO-Massenseparator für das ECHo-Projekt", B.Sc. thesis (Johannes Gutenberg-Universität Mainz, 2015) (cit. on pp. 39, 78).

[76] F. Schneider et al., "Resonance ionization of holmium for ion implantation in microcalorimeters", Nucl. Instrum. Meth. B **376**, 388–392 (2016) 10.1016/j.nimb.2015.12.012 (cit. on pp. 39, 41, 49, 51, 52, 54).

[77] K. Zimmer, "Konzeption, Aufbau und Test der Ionenoptik des RISIKO-Massenseparators", Diploma thesis (Johannes Gutenberg-Universität Mainz, 1990) (cit. on p. 41).

[78] K. Zimmer et al., "Determination of ^{90}Sr in environmental samples with resonance ionization spectroscopy in collinear geometry", Appl. Phys. B **59**, 117–121 (1994) 10.1007/BF01081161 (cit. on p. 41).

[79] S. D. Richter, "Implementierung der Laserionenquellenfalle LIST bei ISOLDE und Validierung der Spezifikationen Effizienz und Selektivititat", PhD thesis (Johannes Gutenberg-Universität, 2015) (cit. on pp. 43, 46, 49, 71–73).

[80] H. Wollnik, *Optics of charged particles* (Academic Press, Inc. San Diego, California, 1987) (cit. on pp. 43, 54, 60, 70).

[81] R. Horn, "Aufbau eines Systems gepulster, abstimmbarer Festkörperlaser zum Einsatz in der Resonanzionisations-Massenspektrometrie", PhD thesis (Johannes Gutenberg-Universität Mainz, 2003) (cit. on p. 44).

[82] S. Rothe, "An all-solid state laser system for the laser ion source RILIS and in-source laser spectroscopy of astatine at ISOLDE/CERN", PhD thesis (Johannes Gutenberg-Universität Mainz, 2012) (cit. on p. 44).

[83] P. Naubereit, "Weiterentwicklung eines weitabstimmbaren Titan:Saphir-Lasers und sein Einsatz zur Spektroskopie hochliegender Resonanzen in Holmium", M.Sc. thesis (Johannes Gutenberg-Universität Mainz, 2014) (cit. on p. 44).

[84] C. Mattolat, "Spektroskopische Untersuchungen an Technetium und Silizium - Ein Festkörperlasersystem für die Resonanzionisationsspektroskopie", PhD thesis (Johannes Gutenberg-Universität Mainz, 2010) (cit. on p. 44).

[85] T. Kron, "*IN PREPARATION*", PhD thesis (Johannes Gutenberg-Universität Mainz, projected 2016) (cit. on p. 44).

[86] V. Sonnenschein, "Laser developments and high resolution resonance ionization spectroscopy of actinide elements", PhD thesis (University of Jyväskylä, 2014) (cit. on p. 44).

[87] T. Gottwald, "Studium hochkomplexer atomarer Spektren mittels Methoden der Laserresonanzionisation", PhD thesis (Johannes Gutenberg-Universität Mainz, 2010) (cit. on pp. 46, 49, 50, 85).

[88] B. Balboul, "Physicochemical characterization of the decomposition course of hydrated holmium nitrate. Thermoanalytical studies", Powder Technol. **107**, 168–174 (2000) 10.1016/S0032-5910(99)00183-7 (cit. on p. 46).

[89] W. Wendlandt and J. Bear, "Thermal decomposition of the heavier rare-earth metal nitrate hydrates: thermobalance and differential thermal analysis studies", J. Inorg. Nucl. Chem. **12**, 276–280 (1960) 10.1016/0022-1902(60)80373-9 (cit. on p. 46).

[90] D. R. Lide, *CRC handbook of chemistry and physics (87th ed.)* (CRC Press, Boca Raton, FL, US, 2006) (cit. on p. 46).

[91] J. S. Becker, "Inductively coupled plasma mass spectrometry (ICP-MS) and laser ablation ICP-MS for isotope analysis of long-lived radionuclides", Int. J. Mass Spectrom. **242**, Isotope Ratio Measurements {SI}, 183–195 (2005) 10.1016/j.ijms.2004.11.009 (cit. on p. 46).

[92] K. Eberhardt and N. Trautmann, "Neutron activation analysis at the TRIGA MARK II research reactor of the University of Mainz", IAEA Tech. Rep. Ser. **455**, 537–545 (2007) (cit. on p. 46).

[93] G. Alkhazov et al., "A new highly efficient method of atomic spectroscopy for nuclides far from stability", Nucl. Instrum. Meth. B **69**, 517–520 (1992) 10.1016/0168-583X(92)95309-F (cit. on p. 49).

[94] G. Alkhazov et al., "Application of a high efficiency selective laser ion source at the IRIS facility", Nucl. Instrum. Meth. A **306**, 400–402 (1991) 10.1016/0168-9002(91)90348-T (cit. on p. 49).

[95] Y. Liu, "ORNL developments in laser ion sources for radioactive ion beam production", Hyperf. Int. **227**, 85–99 (2014) 10.1007/s10751-013-0965-8 (cit. on pp. 49, 85).

[96] A. Kramida et al., NIST Atomic Spectra Database (ver. 5.2), [Online]. Available: http://physics.nist.gov/asd [2015, July 20]. National Institute of Standards and Technology, Gaithersburg, MD. 2014 (cit. on p. 51).

[97] J. R. Conrad et al., "Plasma source ion-implantation technique for surface modification of materials", J. Appl. Phys. **62**, 4591–4596 (1987) 10.1063/1.339055 (cit. on p. 57).

[98] J. F. Ziegler, M. D. Ziegler, and J. P. Biersack, "SRIM - The stopping and range of ions in matter", Nucl. Instrum. Meth. B **268**, 19th International Conference on Ion Beam Analysis, Univ Cambridge, Cambridge, ENGLAND, SEP 07-11, 2009, 1818–1823 (2010) 10.1016/j.nimb.2010.02.091 (cit. on p. 58).

[99] H. von Seggern, "Photostimulable X-ray storage phosphors: a review of present understanding", Braz. J. Phys **29**, 254–268 (1999) 10.1590/S0103-97331999000200008 (cit. on p. 59).

[100] M. N. Saha, "Ionization in the solar chromosphere", Philos. Mag. Ser. 6 **40**, 472–488 (1920) 10.1080/14786441008636148 (cit. on p. 63).

[101] R. Kirchner, "On the thermoionization in hot cavities", Nucl. Instrum. Meth. A **292**, 203–208 (1990) 10.1016/0168-9002(90)90377-I (cit. on pp. 63, 64).

[102] M. Menat, "Quantitative study of scattering phenomena in electromagnetic separator", Can. J. Phys. **42**, 164–192 (1964) 10.1139/p64-013 (cit. on pp. 68, 69).

[103] M. Menat and G. Frieder, "Scattering phenomena in double-direction focusing electromagnetic mass separators", Can. J. Phys. **43**, 1525–1542 (1965) 10.1139/p65-142 (cit. on pp. 68, 69).

[104] F. Hinterberger, *Physik der teilchenbeschleuniger und ionenoptik* (Springer-Verlag Berlin Heidelberg, 2008), 10.1007/978-3-540-75282-0 (cit. on p. 76).

[105] U. Timm, "Zur berechnung elektrostatischer linsen", Z. Naturforsch. A **10**, 593–602 (1955) 10.1515/zna-1955-0801 (cit. on p. 76).

[106] J. J. W. van de Laar, "Aufbau eines ortsempfindlichen Detektors für TRIGA-TRAP", Diploma thesis (Johannes Gutenberg-Universität Mainz, 2015) (cit. on p. 84).

[107] J. Ketelaer et al., "Recent developments in ion detection techniques for Penning trap mass spectrometry at TRIGA-TRAP", Eur. Phys. J. A **42**, 311–317 (2009) 10.1140/epja/i2008-10711-6 (cit. on p. 84).

[108] D. Dahl, *SIMION software, version 8.0.5* (Idaho Falls, ID, USA, 2012) (cit. on p. 89).

[109] D. A. Dahl, “Simion for the personal computer in reflection”, Int. J. Mass Spectrom. **200**, Volume 200: The state of the field as we move into a new millenium, 3–25 (2000) 10.1016/S1387-3806(00)00305-5 (cit. on p. 89).

[110] L. He and D. M. Lubman, “Simulation of external ion injection, cooling and extraction processes with SIMION 6.0 for the ion trap/reflectron time-of-flight mass spectrometer”, Rapid Commun. Mass Spectrom. **11**, 1467–1477 (1997) 10.1002/(SICI)1097-0231(19970830)11:13<1467::AID-RCM54>3.0.CO;2-X (cit. on p. 90).

[111] Y.-K. Choi, H.-S. Im, and K.-W. Jung, “Laser ablation of graphite at 355 nm: cluster formation and plume propagation”, Int. J. Mass Spectrom. **189**, 115–123 (1999) 10.1016/S1387-3806(99)00060-3 (cit. on pp. 90, 91).

[112] J. Kools, E. van de Riet, and J. Dieleman, “A simple formalism for the prediction of angular distributions in laser ablation deposition”, Appl. Surf. Sci. **69**, 133–139 (1993) 10.1016/0169-4332(93)90494-V (cit. on pp. 90, 91).

[113] I. Konomi, T. Motohiro, and T. Asaoka, “Angular distribution of atoms ejected by laser ablation of different metals”, J. Appl. Phys. **106**, 013107 (2009) 10.1063/1.3160305 (cit. on pp. 90, 91).

[114] R. Cotter, *Time of flight mass spectrometry: instrumentation and applications in biological research* (ACS,Washington D.C., 1997) (cit. on p. 97).